Department of Physics
Technical University of Munich

Dissertation

Theory of Structural Dynamics in Energy Materials and Implications for Functional Properties

Christian Gehrmann

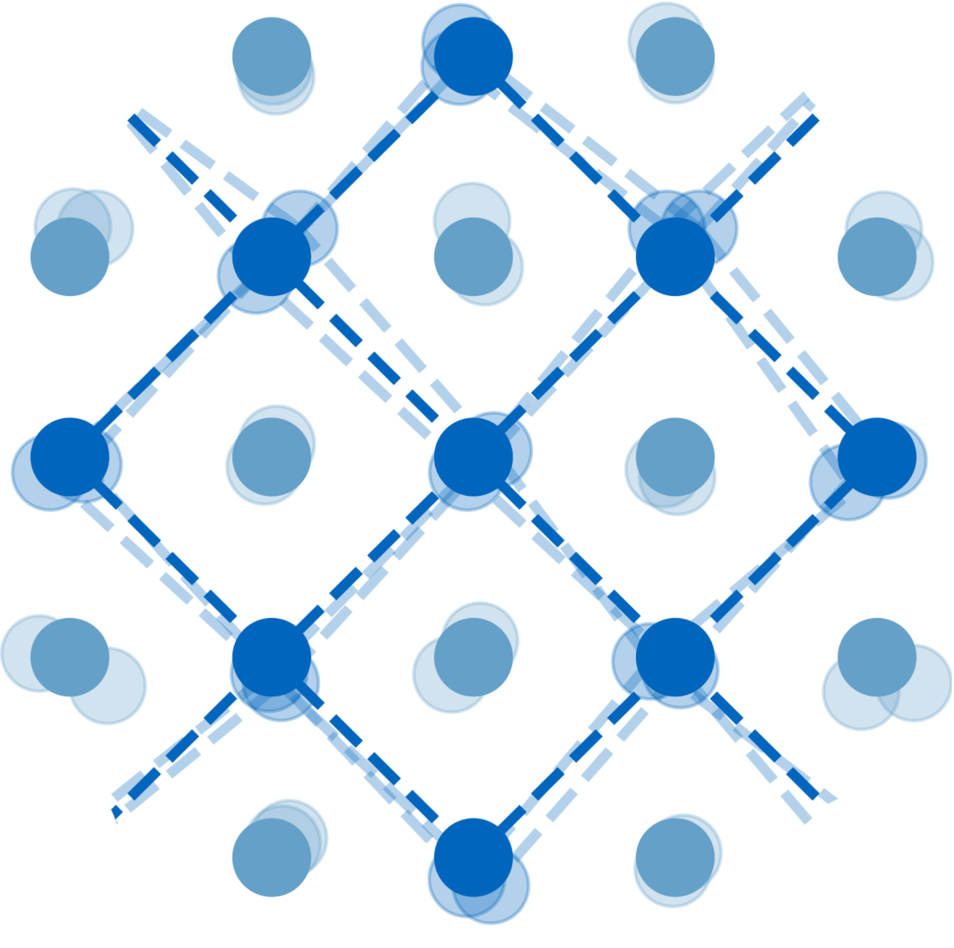

Technische Universität München
Fakultät für Physik

Theory of Structural Dynamics in Energy Materials and Implications for Functional Properties

Christian Gehrmann

Vollständiger Abdruck der von der Fakultät für Physik der Technischen Universität München

zur Erlangung eines

Doktors der Naturwissenschaften (Dr. rer. nat.)

genehmigten Dissertation.

Vorsitz: Prof. Dr. Ian Sharp

Prüfer*innen der Dissertation:

1. Prof. Dr. David Egger
2. Prof. Dr. Martin Zacharias

Die Dissertation wurde am 05.05.2022 bei der Technischen Universität München eingereicht

und durch die Fakultät für Physik am 26.05.2022 angenommen.

Abstract

A profound understanding of structural dynamics is crucial to develop a complete picture of energy materials and their functional properties on the microscopic scale. Traditionally, structural dynamics in crystals are studied within the harmonic approximation. However, in view of the search for and research on new, more efficient energy materials, such as halide perovskites (HaPs) and solid-state ion conductors (SSICs), exploring methods beyond the harmonic approximation becomes scientifically interesting, although it is theoretically challenging.

In this work, state-of-the-art computational methods, in particular first-principles molecular dynamics (MD) simulations, are used to investigate structural dynamics and their implications for functional properties in two types of materials, HaPs and the SSIC α-AgI. Manifestations of vibrational anharmonicity are identified and explored in both materials.

The paradigmatic $CsPbBr_3$ is used as a representative system for the material class HaPs to investigate the impact of anharmonic structural dynamics on band-edge energy distribution, correlations in the disorder potential induced by atomic displacements, and the joint-density of states. To this end, MD simulations are analyzed and contrasted to static calculations. The effect of the different kinds of atomic motion within the material is studied using *gedankenexperiments*. Particular attention is paid to the motion of the halide atoms, whose structural flexibility is a distinctive feature of the perovskite structure. This is shown to be connected to some of the favorable properties of the materials, as a comparison to PbTe confirms.

For α-AgI, anharmonic relaxational motion of the iodine host-lattice is studied using MD simulations and polarization-orientation Raman measurements, which were obtained from our experimental collaborators. A model of local AgI_4 tetrahedral oscillators is introduced to fully explain the experimental spectra. Trajectories of the angle formed by three iodine ions exhibit large deviations from the expectation value, revealing relaxational motion of iodine ions within the tetrahedra. This relaxational motion of the iodine ions is shown to be related to silver diffusion in this ion conductor, which allows to develop a picture of the connection between host-lattice dynamics and ion diffusion.

In summary, manifestations of anharmonicity are found in all energy materials studied and it is shown that structural dynamics facilitate some of their favorable functional properties.

Zusammenfassung

Ein gründliches Verständnis von struktureller Dynamik ist essentiell, um ein umfassendes Bild von Energiematerialien und ihren funktionalen Eigenschaften auf mikroskopischer Ebene zu entwickeln. Üblicherweise wird strukturelle Dynamik in Kristallen mit der harmonischen Näherung beschrieben. Auf der Suche nach neuen, effizienteren Energiematerialien wie Halogenid-Perowskiten und Festkörperionenleitern ist es von großem wissenschaftlichen Interesse über die harmonische Näherung hinauszugehen, auch wenn dies aus theoretischer Sicht noch immer eine Herausforderung darstellt.

In dieser Arbeit werden moderne Computerverfahren verwendet, um die strukturelle Dynamik und ihre Auswirkung auf funktionale Eigenschaften zu untersuchen. Allem voran sind dies Molekulardynamiksimulationen (MD), die auf Dichtefunktionaltheorie basieren. Hierbei werden zwei Arten von Materialien erforscht: Halogenid-Perowskite und der Ionenleiter α-AgI.

Die Perowskite werden am Beispiel $CsPbBr_3$ betrachtet und der Einfluss von Anharmonizität auf die Energieverteilung an den Bandkanten, Korrelationen im Unordnungspotential und die kombinierte Zustandsdichte untersucht. Hierfür werden die MD Simulationen eingehend analysiert und statischen Simulationen gegenübergestellt. Der Einfluss der Bewegung unterschiedlicher Atomsorten im Material wird anhand von Gedankenexperimenten erforscht. Ein besonderer Fokus wird dabei auf die Halogenatome gelegt, deren große Flexibilität ein markantes Merkmal der Perowskitstruktur ist, das mit einigen vorteilhaften Eigenschaften des Materials in Verbindung gebracht werden kann wie ein Vergleich zu PbTe bekräftigt.

In α-AgI wird die anharmonische Bewegung des von den Iodid-Ionen gebildeten Gitters anhand von MD Simulationen und Ramanspektroskopie untersucht. Um das experimentelle Ramanspektrum unserer Kollaboratoren vollständig beschreiben zu können, wird ein Model aus lokalen AgI_4 Tetraedern eingeführt. Der Winkel zwischen drei Iodid-Ionen eines Tetraeders durchläuft große, langanhaltende Abweichungen vom Erwartungswert. Dies offenbart eine relaxierende Bewegung der Iodid-Ionen innerhalb der Tetraeder. Diese Bewegung der Iodid-Ionen kann mit der Diffusion der Silber-Ionen in Verbindung gebracht werden, was es erlaubt ein Bild für den Zusammenhang von Gitterdynamik und Ionendiffusion zu entwickeln.

Zusammenfassend kann gesagt werden, dass anharmonische Atombewegungen in allen untersuchten Materialien auftreten und darüber hinaus kann gezeigt werden, dass diese einige der funktionalen Eigenschaften positiv beeinflussen.

List of publications

The research presented in this work was started at the former research group *Computational Materials Physics* at the University of Regensburg and continued in the research group *Theory of Functional Energy Materials*, Technical University of Munich. Parts of the results have a been published in the following peer-reviewed publications:

[1] Beck, H., Gehrmann, C. & Egger, D. A. Structure and binding in halide perovskites: Analysis of static and dynamic effects from dispersion-corrected density functional theory. *APL Mater.* **7,** 021108. doi:`10.1063/1.5086541` (2019)

[2] Gehrmann, C. & Egger, D. A. Dynamic shortening of disorder potentials in anharmonic halide perovskites. *Nat. Commun.* **10,** 3141. doi:`10.1038/s41467-019-11087-y` (2019)

[3] Brenner, T. M., Gehrmann, C., Korobko, R., Livneh, T., Egger, D. A. & Yaffe, O. Anharmonic host-lattice dynamics enable fast ion conduction in superionic AgI. *Phys. Rev. Mater.* **4,** 115402. doi:`10.1103/PhysRevMaterials.4.115402` (2020)

[4] Seidl, S. A., Kretz, B., Gehrmann, C. & Egger, D. A. Assessing the accuracy of screened range-separated hybrids for bulk properties of semiconductors. *Phys. Rev. Mater.* **5,** 034602. doi:`10.1103/PhysRevMaterials.5.034602` (2021)

[5] Gehrmann, C., Caicedo-Dávila, S., Zhu, X. & Egger, D. A. Transversal Halide Motion Intensifies Band-To-Band Transitions in Halide Perovskites. *Adv. Sci.,* 2200706. doi:`10.1002/advs.202200706` (2022)

[6] Zhu, X., Caicedo-Dávila, S., Gehrmann, C. & Egger, D. A. Probing the Disorder Inside the Cubic Unit Cell of Halide Perovskites from First-Principles. *ACS Appl. Mater. Interfaces,* acsami.1c23099. doi:`10.1021/acsami.1c23099` (2022)

Acknowledgments

The research reported in this thesis was carried out under the guidance and supervision of Prof. David A. Egger, to whom I would like to express my deepest gratitude. This work would have been impossible without his guidance and support. Furthermore, special thanks should be given to Dr. Bernhard Kretz for being my mentor and always giving valuable advise on scientific topics and beyond.

In addition, I would like to thank all members of the TheoFEM group at the TUM – including the former CMS group at the University of Regensburg – for joining me on the journey of this thesis. I have greatly benefited from all our interesting discussions and our social activities inside and outside the office have been a great joy.

But moreover, scientific research is based on bringing together the experience and expertise of various scientist by collaborations and discussions. As a consequence, also this thesis has been enriched by several collaborations which I would like to acknowledge here. To begin with, I want to thank all our experimental collaborators for sharing both their immense knowledge and their data. First of all, I am indebted to Michael Sendner, Sebastian Beck, and Robert Lovrincic, who provided us with experimental data on the infra-red spectra of halide perovskites. Some of their experimental spectra, shown in section 3.2, are still unpublished and I am profoundly grateful for the opportunity to include them in this thesis. Second, I want to express my sincere thanks to Thomas M. Brenner and Omer Yaffe, as well as Roman Korobko and Tsachi Livneh for our successful collaboration on the structural dynamics of α-AgI. Without their Raman spectra, encouragement and patience the project about this solid-state ion conductor would not have been realized. To continue with our theoretical collaborators, I am grateful to Hubert Beck for our fruitful work on finding the parameters most suitable for simulating structural properties of halide perovskites. Hubert's results have been of great value for my research. Furthermore, I want to express my gratitude to Xiangzhou Zhu and Sebastián Caicedo-Dávila for their enormous contributions to our work on understanding the importance of the transversal halide motion in $CsPbBr_3$ and the difference between the halide perovskite and PbTe, as well as our extensive and valuable discussions on disorder and dynamics in halide perovskites. In particular, Sebastián contributed equally to the analysis of the data shown in sections 3.7 and 3.8 and published in reference [5]. Last but not least, I want to thank Stefan Seidl and Bernhard Kretz for our discussions on and their insightful comments about DFT and XC-functionals. Special thanks also to Stefan for always organizing coffee for our offices.

Finally, I gratefully acknowledge the Gauss Centre for Supercomputing e.V. (`www.gauss-centre.eu`) for funding this project by providing computing time through the John von Neumann Institute for Computing (NIC) on the GCS Supercomputer JUWELS at Jülich Supercomputing Centre (JSC).

Contents

1. Introduction

Our modern civilization and lifestyle comes with the cost of an ever increasing power consumption. At the same time we have realized that our dependence on fossil energy sources has to be overcome. Therefore, there is an increasing interest in renewable energy sources and much effort is put into the technologies behind renewable energy. Involved technologies include methods to convert energy, such as photovoltaics, but they also include energy storage systems, e.g., batteries. One approach to improve devices is to learn about the involved materials. We call materials used, e.g., in solar cells or batteries *"energy materials"*. Depending on their application, energy materials have properties that are particularly important – we call them *"functional properties"*. Examples for functional properties are optical absorption in materials used for solar cells, or ionic conductivity in electrolytes used for batteries. Naturally, the material choice allows to optimize functional properties for a specific scenario, resulting in more efficient devices. But also microscopic details strongly impact functional properties. For instance, both crystalline and amorphous silicon are candidates to be used as a light-absorbing material in solar cells. However, the former reaches higher efficiencies [7]. While both examples for solar cells are based on the same chemical element – Si – the spatial arrangement of the Si atoms differs at the microscopic scale. As this example indicates, functional properties can be modified by a variety of microscopic effects.

Our goal is to understand energy materials and their functional properties on the microscopic scale with the aim to eventually provide new insight to optimize materials and devices. Studying a material on the microscopic level can include many aspects, such as electronic properties (e.g., the electronic bandstructure in semiconductors), optical properties and structural properties. In this work we are particularly interested in the structural dynamics in energy materials and their implications for functional properties. Structural dynamics means we are interested in how atoms move at finite temperature.

Usually, atomic motion in crystals is treated in the harmonic approximation, an approach which has been proven to be accurate for many conventional materials. In this approximation, the potential energy surface $V(\mathbf{x})$ of the ions is expanded in a Taylor series, keeping only non-vanishing terms of the lowest order in the atomic displacements, i.e., terms quadratic in the displacements away from the average position $\mathbf{x}_0$:

$$V(\mathbf{x}) \approx \nabla^2 V(\mathbf{x})|_{\mathbf{x}_0} (\mathbf{x} - \mathbf{x}_0)^2 \ . \tag{1.1}$$

In contrast, effects that can only be described with higher-order terms are called anharmonic effects. For crystalline materials, the harmonic approximation can be solved using a plane-wave ansatz and further simplifies due to the translational invariance. This finally results in a description of lattice dynamics in crystalline materials in reciprocal space, i.e., $\mathbf{q}$-point dependent vibrational *dispersion relations* are obtained. The vibrational quasi-particles, obtained in a quantum mechanical description of lattice dynamics, are called *phonons*. By now, phonons have been well-studied, including the development of theories that allow for a profound understanding of their impact on materials properties such as heat transport and electron-phonon coupling.

However, many interesting effects occur when approaching the limits of the harmonic approximation, such as finite phonon lifetimes due to phonon-phonon interactions. Commonly, limitations of the harmonic approximation are equalized with the necessity of including higher order terms in eq. (1.1). Higher order contributions to lattice dynamics, such as cubic or quartic terms, can, e.g., be included perturbatively and manifest for instance in finite phonon lifetimes and frequency shifts. However, the harmonic approximation and subsequent perturbative treatments of anharmonicity are based on another very important assumption, namely the existence of a well-defined equilibrium position $\mathbf{x}_0$. Also this latter approximation can be violated in crystals, for instance, in solid-state ion conductors (SSICs), i.e., crystalline materials which conduct electrical current via diffusing ions. Consequently, the diffusing ions frequently hop among different locations, and as a result there is no unique equilibrium structure.

Exploring methods going beyond the harmonic approximation to study structural dynamics and their implications for functional properties in energy materials is scientifically interesting and theoretically challenging for this reason. Molecular dynamics (MD) simulations are one way to tackle the challenge: in contrast to, e.g., perturbative methods, all orders in the Taylor series for the potential energy surface of the atoms are considered and no well-defined equilibrium positions for the atoms have to be assumed in MD simulations. Instead of approximating the potential energy surface, Newton's equations of motion are solved numerically using instantaneous forces on the atoms as obtained, for instance, from quantum mechanical electronic structure calculations. In this way, trajectories of the atomic positions are obtained which allow to study structural dynamics in energy materials, including the identification and investigation of anharmonicity. Moreover, this approach allows to study implications of structural dynamics for functional properties, both directly from the trajectories and by using the instantaneous atomic configurations.

While many inorganic materials, especially textbook examples like Si and GaAs, can be described accurately by theories based on the harmonic or perturbative treatments of atomic motion, several materials exhibit more complex dynamics. With this, they challenge the conventional view which assumes well-defined reference structures combined with harmonic phonons that show long lifetimes and mean-free paths. These materials include many energy materials like halide perovskites (HaPs), organic semiconductors, SSICs, and thermoelectrics. HaPs are a relatively new class of materials for use as solar absorbers [8–18], as well as LEDs and lasers [19, 20], and sensor applications [20]. Their remarkable functional properties resulted in obtaining solar cells with high efficiency within a comparably short time [7, 16]. At the same time, they show interesting structural dynamics, including phase transitions and rotational motion of the small organic cations in hybrid HaPs [2, 21–27]. Similarly, organic semicondutors can, among other applications, be used for solar cells [28], while anharmonicity has been measured experimentally in these materials [29, 30],manifesting itself, for instance, in a dynamic symmetry breaking of the structure [31]. SSICs, compelling as electrolytes in batteries [32], show a close connection between an important functional property – the conductivity – and structural dynamics, due to the conduction mechanism via diffusing ions, but lack a unique equilibrium structure for the same reason. Last but not least, thermoelectrics, i.e., materials capable of converting thermal energy into electrical energy – and vice versa –, require low thermal conductivity, and thus small phonon mean free paths [33]. As a consequence, materials which behave as “phonon-glass, electron-crystal” are explored as thermoelectrics [34]. Hence, it is proposed to study the effects of structural dynamics and their impact on functional properties for these systems. Specifically, from the broad spectrum of the above mentioned materials, HaPs and α-AgI, a paradigmatic SSIC, are chosen for this work.

To summarize the main scientific goal that will be addressed in this work: using advanced computational methods, such as first-principles MD simulations, to investigate structural dynamics on the microscopic scale, we aim to probe the limits of the conventional harmonic treatment in paradigmatic energy materials and finally unravel the impact of structural dynamics, including anharmonicity, on some of their key functional properties, namely the steepness of optical absorption close to its onset in HaPs and ionic conductivity in SSICs (sketched in fig. 1.1).

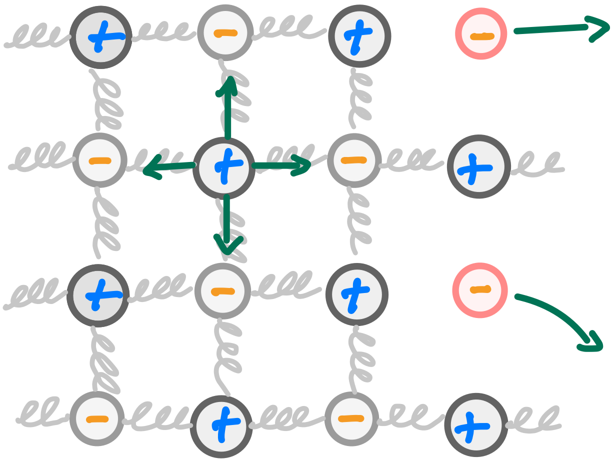

Figure 1.1.: Sketch visualizing that understanding atomic motion (green arrows), e.g., whether it is harmonic (indicated as ”springs”), is required to understand material properties such as charge transport via ion diffusion.

2. Theory

Unless specific references have been cited, the below sections are based on the following textbooks [35–41] and material provided with the online documentation of the tools used (e.g., [42–44]).

The goal of this thesis is to provide a microscopic picture of structural dynamics and functional properties in energy materials. The starting point for any non-relativistic microscopic description is quantum mechanics, with the Schrödinger equation

$$i\hbar\frac{\partial}{\partial t}\Psi(\mathbf{r}_1\ldots\mathbf{r}_N,\mathbf{R}_1\ldots\mathbf{R}_M,t) = \hat{\mathsf{H}}\Psi(\mathbf{r}_1\ldots\mathbf{r}_N,\mathbf{R}_1\ldots\mathbf{R}_M,t) \tag{2.1}$$

as the essential equation. The solution of the Schrödinger equation is the wavefunction $\Psi(\mathbf{r}_1\ldots\mathbf{r}_N,\mathbf{R}_1\ldots\mathbf{R}_M,t)$, with N and M the number of electrons and atoms, respectively. The Hamilton operator

$$\hat{\mathsf{H}} = \hat{\mathsf{T}}_e+\hat{\mathsf{T}}_{\text{nuclei}}+\frac{1}{2}\sum_i\sum_{j\neq i}\frac{e^2}{|\mathbf{r}_i-\mathbf{r}_j|}-\sum_i\sum_I\frac{Z_Ie^2}{|\mathbf{r}_i-\mathbf{R}_I|}+\frac{1}{2}\sum_I\sum_{J\neq I}\frac{Z_IZ_Je^2}{|\mathbf{R}_I-\mathbf{R}_J|}\ , \tag{2.2}$$

is used to describe a solid-state material. The operators

$$\hat{\mathsf{T}}_e = \sum_i\frac{\hat{\mathsf{p}}_i^2}{2m_e} = -\sum_i\frac{\hbar^2}{2m_e}\nabla^2_{\mathbf{r}_i} \quad \text{and} \tag{2.3}$$

$$\hat{\mathsf{T}}_{\text{nuclei}} = \sum_I\frac{\hat{\mathsf{p}}_I^2}{2M_I} = -\sum_I\frac{\hbar^2}{2M_I}\nabla^2_{\mathbf{R}_I} \tag{2.4}$$

are the kinetic energy operators for electrons, with positions $\mathbf{r}_i$ and charge e, and ionic nuclei, at positions $\mathbf{R}_I$ and charges Z_Ie, respectively. This Hamilton operator includes many-particle operators, such as the terms $\frac{1}{2}\sum_i\sum_{j\neq i}\frac{e^2}{|\mathbf{r}_i-\mathbf{r}_j|}$. As a consequence, a many-body Schrödinger equation would have to be solved. This is almost impossible to do for any real system, since for real materials there are about $\mathcal{O}\left(10^{23}\right)$ atoms and electrons. For this reason we have to make use of approximations which simplify this task. One set of approximations is described below, it leads to a theory called *density functional theory (DFT)*, a very popular electronic structure theory.

2.1. Born-Oppenheimer approximation

Following reference [41], as a first approximation, it is assumed that the light electrons *adiabatically* adapt to the instantaneous nuclear positions. This approximation can be made because the mass of electrons m_e is much smaller than the mass of the ionic nuclei M_I

$$\frac{M_I}{m_e} \approx 10^4 \text{ to } 10^6 \ . \tag{2.5}$$

As a consequence of this mass difference, electronic motion is happening on much shorter timescales than ionic motion. Thus we separate the time-dependent wavefunction $\Psi(\mathbf{r}_1 \dots \mathbf{r}_N, \mathbf{R}_1 \dots \mathbf{R}_M, t)$ into time-dependent wavefunctions for the nuclei $\chi_l(\{\mathbf{R}_I\}, t)$ and stationary electronic wavefunctions $\psi_l(\{\mathbf{r}_i\}, \{\mathbf{R}_I\})$ which contain the instantaneous nuclear positions $\{\mathbf{R}_I\}$. And thus they contain an implicit time dependence through the nuclear positions, as parameters

$$\Psi(\{\mathbf{r}_i\}, \{\mathbf{R}_I\}, t) = \sum_l \psi_l(\{\mathbf{r}_i\}, \{\mathbf{R}_I\}) \chi_l(\{\mathbf{R}_I\}, t) \ . \tag{2.6}$$

Moreover, the electronic wavefunctions $\psi_l(\{\mathbf{r}_i\}, \{\mathbf{R}_I\})$ are the solutions of the time-independent electronic Schrödinger equation

$$\hat{\mathsf{H}}_e \psi_l = E_l \psi_l \ , \tag{2.7}$$

with the electronic Hamiltonian

$$\hat{\mathsf{H}}_e = \hat{\mathsf{T}}_e + \frac{1}{2} \sum_i \sum_{j \neq i} \frac{e^2}{|\mathbf{r}_i - \mathbf{r}_j|} - \sum_i \sum_I \frac{Z_I e^2}{|\mathbf{r}_i - \mathbf{R}_I|} + \frac{1}{2} \sum_I \sum_{J \neq I} \frac{Z_I Z_J e^2}{|\mathbf{R}_I - \mathbf{R}_J|} \ . \tag{2.8}$$

Applying the approach from eq. (2.6) to eq. (2.1) reveals

$$\left[\hat{\mathsf{T}}_{\text{nuclei}} + E_l(\{\mathbf{R}_I\}) \right] \chi_l(\{\mathbf{R}_I\}, t) + \sum_k C_{lk} \chi_k(\{\mathbf{R}_I\}, t) = i\hbar \frac{\partial}{\partial t} \chi_l(\{\mathbf{R}_I\}, t) \ , \tag{2.9}$$

with $E_l(\{\mathbf{R}_I\})$ an eigenvalue of eq. (2.7) and

$$C_{kl} = \langle \psi_k | \, \hat{\mathsf{T}}_{\text{nuclei}} \, |\psi_l\rangle = \sum_I \langle \psi_k | \, \frac{\hat{\mathsf{p}}_I^2}{2M_I} \, |\psi_l\rangle = \sum_I \frac{1}{M_I} \langle \psi_k | \, \big(\hat{\mathsf{p}}_I \, |\psi_l\rangle \big) \hat{\mathsf{p}}_I \tag{2.10}$$

being matrix elements of the nuclear kinetic energy operator. In the simplest approximation, no coupling of the nuclear kinetic energy operator on the electronic wavefunctions is assumed ($C_{kl} = 0$), and thus

$$\left[\hat{\mathsf{T}}_{\text{nuclei}} + E_l(\{\mathbf{R}_I\}) \right] \chi_l(\{\mathbf{R}_I\}, t) = i\hbar \frac{\partial}{\partial t} \chi_l(\{\mathbf{R}_I\}, t) \ . \tag{2.11}$$

This approximation is called the *Born-Oppenheimer approximation* whose original derivation involved a perturbative treatment of the problem with an expansion in terms of $\kappa = (m_e/M)^{1/4}$ [38, 41, 45]. The Born-Oppenheimer approximation is a special case of the *adiabatic approximation* which assumes that electrons adiabatically adapt to the instantaneous nuclear positions [41]. The adiabatic approximation, however, allows for the inclusion of diagonal elements C_{kk} in eq. (2.9) [41]. As a very important consequence of the Born-Oppenheimer approximation, which we will apply below, we can solve the stationary Schrödinger equation for the electrons decoupled from the nuclear dynamics. And *vice versa*, we can solve the nuclear dynamics with the electrons only acting as a potential $E_l(\{\mathbf{R}_I\})$.

2.2. Density functional theory (DFT)

2.2.1. Electronic ground-state energy

After separating electronic and nuclear degrees of freedom, there still remains a many-body equation for the electrons. Many-body Hamiltonians are extremely difficult to solve compared to single particle theories. Therefore, the goal is to apply a theory which is approximating the many-body problem by single particle equations: (Kohn-Sham) DFT. The derivation of DFT includes the Hohenberg-Kohn theorems [46]. These theorems allow to replace the equations for the wavefunctions $\psi_i(\mathbf{r}_1, \ldots, \mathbf{r}_N)$, which depend on all spatial coordinates of all electrons, by equations for the density $n(\mathbf{r})$, which depends on only three spatial coordinates. The first Hohenberg-Kohn theorem states that for any system of interacting electrons, their density determines the external potential uniquely (up to a constant). The second Hohenberg-Kohn theorem states that there exists a universal functional $E[n(\mathbf{r})]$ which provides the exact ground state energy and density of any interacting electron system in an external potential. Therefore, the initial problem is simplified by using the (charge) density instead of quantum mechanical wavefunctions. The next step is to map the interacting system to a non-interacting system. This can be done using the Kohn-Sham map [47]. It maps an interacting system to a non-interacting system, such that the groundstate charge density is equal in both systems. According to the Hohenberg-Kohn theorems, the ground state density uniquely determines the external potential for this system, the Kohn-Sham potential

$$V_{\mathrm{KS}} = V_{\mathrm{ext}}(\mathbf{r}) + \mathrm{e}^2 \int d^3r' \frac{n(\mathbf{r'})}{|\mathbf{r} - \mathbf{r'}|} + \frac{\delta E_{\mathrm{xc}}[n(\mathbf{r})]}{\delta n(\mathbf{r})} \ . \tag{2.12}$$

From this, the Kohn-Sham equation can be obtained:

$$\left\{ -\frac{\hbar^2 \nabla^2}{2m} + V_{\mathrm{ext}}(\mathbf{r}) + \mathrm{e}^2 \int d^3r' \frac{n(\mathbf{r'})}{|\mathbf{r} - \mathbf{r'}|} + \frac{\delta E_{\mathrm{xc}}[n(\mathbf{r})]}{\delta n(\mathbf{r})} \right\} \psi_i = E_i \psi_i \ . \tag{2.13}$$

This equation depends on the charge density $n(\mathbf{r})$ which again can be obtained from the Kohn-Sham wavefunctions ψ_i:

$$n(\mathbf{r}) = \sum_{i=1}^{N} |\psi_i|^2 \ . \tag{2.14}$$

The charge density is used as a parameter in eq. (2.13) and depends on its solution ψ_i, see eq. (2.14). Thus, eq. (2.13) has to be solved self-consistently. A procedure to solve eq. (2.13) self-consistently has been sketched in fig. 2.1. In this self-consistent scheme, one starts by providing an initial guess for the charge density or wavefunctions, e.g., from a superposition of atomic orbitals. Using this trial charge density, one can calculate the Kohn-Sham potential, eq. (2.12), for the current iteration. Provided with the potential, one can solve the Kohn-Sham equations, eq. (2.13), to obtain a new set of Kohn-Sham wavefunctions and consequently a new charge density according to eq. (2.14). The quantities calculated from the new solutions of

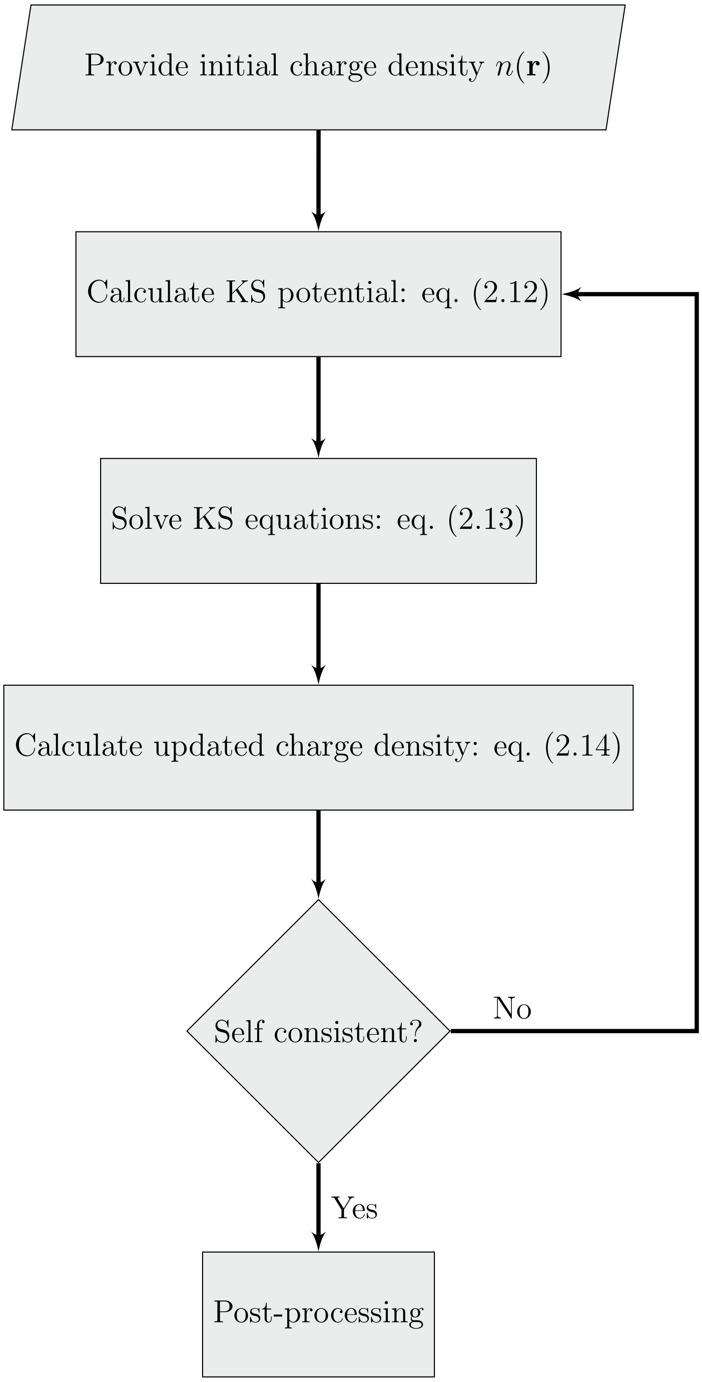

Figure 2.1.: Flowchart of the procedure to solve the Kohn-Sham equations self-consistently.

the Kohn-Sham equations can now be compared with the solutions from the previous iteration, i.e., check the solutions for self-consistency. Once the changes, e.g., in total energy, are below a defined threshold, the calculation is converged and further analysis can be done. However, if the differences between the current and the previous iteration are larger than the threshold, the current charge density is used to further iteratively solve eqs. (2.12) to (2.14).

Exchange-correlation functionals

In principle, Kohn-Sham DFT following the procedure described above is exact, provided we know the exact exchange-correlation (XC) energy E_{xc}. In practice, however, this is not known and one has to rely on approximations. The accuracy of Kohn-Sham DFT calculations thus depends on the approximation for the XC functional. Commonly used approximations include the local density approximation (LDA) and the generalized gradient approximations (GGA).

In the LDA, it is assumed that E_{xc} depends only on the local charge density

$$E_{\mathrm{xc}}^{\mathrm{LDA}}[n(\mathbf{r})] = \int d^3r \; n(\mathbf{r}) \left[\epsilon_{\mathrm{x}}(n(\mathbf{r})) + \epsilon_{\mathrm{c}}(n(\mathbf{r}))\right] \tag{2.15}$$

and that it can locally be approximated by a homogeneous electron gas, i.e.,

$$\epsilon_{\mathrm{x}}(n(\mathbf{r})) = \epsilon_{\mathrm{x}}^{\mathrm{hom}}(n(\mathbf{r})) = -\frac{3e^2 k_F}{4\pi} \quad \text{and} \quad \epsilon_{\mathrm{c}}(n(\mathbf{r})) = \epsilon_{\mathrm{c}}^{\mathrm{hom}}(n(\mathbf{r})) \; , \tag{2.16}$$

with k_F the Fermi wavevector, related to the Fermi energy E_F by $\hbar k_F = \sqrt{2mE_F}$. The exchange energy of a homogeneous electron gas is known exactly, and the correlation energy can be calculated using quantum Monte Carlo methods [48]. The spin-polarized formulation of LDA is often called local spin density approximation (LSD), $E_{\mathrm{xc}}^{\mathrm{LSD}} = E_{\mathrm{xc}}^{\mathrm{LSD}}[n_\uparrow, n_\downarrow]$, and depends on the densities for spin-up $n_\uparrow$ and spin-down $n_\downarrow$, individually.

In the GGA, the gradient of the charge density $\nabla n(\mathbf{r})$ is considered explicitly in the XC energy

$$E_{\mathrm{xc}}^{\mathrm{GGA}}[n(\mathbf{r})] = \int d^3r \; n(\mathbf{r}) \epsilon_{\mathrm{xc}}(n(\mathbf{r}), \nabla n(\mathbf{r})) = \int d^3r \; f(n(\mathbf{r}), \nabla n(\mathbf{r})) \; . \tag{2.17}$$

GGA functionals thus rely on a function f which has to be parameterized.

A famous parametrization is that of Perdew, Burke, and Ernzerhof (PBE) [49]. In this approach all parameters beyond those of the LSD are fundamental constants. First, the exchange-correlation energy,

$$E_{\mathrm{xc}}^{\mathrm{PBE}} = E_{\mathrm{x}}^{\mathrm{PBE}} + E_{\mathrm{c}}^{\mathrm{PBE}} \; , \tag{2.18}$$

is written as a sum of the exchange energy $E_{\mathrm{x}}^{\mathrm{PBE}}$ and the correlation energy $E_{\mathrm{c}}^{\mathrm{PBE}}$. The exchange energy is given as a function of the dimensionless density gradient

$$s = \frac{1}{2k_F} \frac{|\nabla n(\mathbf{r})|}{n(\mathbf{r})} \; , \tag{2.19}$$

by the equation

$$E_{\mathrm{x}}^{\mathrm{PBE}}[n(\mathbf{r})] = \int d^3r\; n(\mathbf{r})\epsilon_{\mathrm{x}}^{\mathrm{hom}}(n(\mathbf{r}))F_{\mathrm{x}}(s)\ , \tag{2.20}$$

with

$$F_{\mathrm{x}}(s) = 1 + \kappa - \frac{\kappa}{1 + \frac{\mu s^2}{\kappa}}\ . \tag{2.21}$$

The remaining parameters are determined to be

$$\kappa = 0.804 \quad \text{and} \quad \mu \simeq \frac{0.066725\pi^2}{3} \simeq 0.21951\ . \tag{2.22}$$

Similarly, the correlation energy E_{c} can be obtained as a function of a dimensionless density gradient

$$t = \frac{1}{2\phi k_s}\frac{|\nabla n(\mathbf{r})|}{n(\mathbf{r}}\ , \tag{2.23}$$

with

$$\phi(\zeta) = \frac{(1+\zeta)^{2/3} + (1-\zeta)^{2/3}}{2}\quad , \quad \zeta = \frac{n_\uparrow - n_\downarrow}{n}\ . \tag{2.24}$$

In particular $\phi = 1$ for the spin-unpolarized case. Further, to parameterize E_{c}, the Bohr radius a_0, Thomas-Fermi screening wave number k_s, and local Seitz radius r_s, defined by

$$a_0 = \frac{\hbar^2}{me^2}\quad , \quad k_s = \sqrt{\frac{4k_F}{\pi a_0}} \quad \text{and} \quad \frac{3}{4\pi r_s^3} = \frac{k_F^3}{3\pi^2}\ , \tag{2.25}$$

respectively, as well as the parameters

$$\gamma = \frac{1 - \ln(2)}{\pi^2} \simeq 0.031091 \quad \text{and} \quad \beta \simeq 0.066725 \tag{2.26}$$

are used. Applying all these definitions, the correlation energy in the PBE parametrization can be written as

$$E_{\mathrm{c}}^{\mathrm{PBE}}[n_\uparrow(\mathbf{r}), n_\downarrow(\mathbf{r})] = \int d^3r\; n(\mathbf{r})\ \left[\epsilon_{\mathrm{c}}^{\mathrm{hom}}(r_s,\zeta) + H(r_s,\zeta,t)\right]\ . \tag{2.27}$$

Consequently, the gradient contribution is given by

$$H(r_s,\zeta,t) = \frac{e^2\gamma\phi^3}{a_0}\ln\left(1 + \frac{\beta}{\gamma}t^2\left[\frac{1+At^2}{1+At^2+A^2t^4}\right]\right)\ , \tag{2.28}$$

with

$$A = \frac{\beta}{\gamma}\frac{1}{\exp\left(-a_0\epsilon_{\mathrm{c}}^{\mathrm{hom}}/\gamma\phi^3e^2\right) - 1}\ . \tag{2.29}$$

It is interesting to note that parameters and functions in the PBE functional are obtained by enforcing the postulated functions to obey certain physical constraints, e.g., to recover the LSD approximation for $s \to 0$. The PBE functional is expected to improve the accuracy of calculations for several physical properties with respect to LDA/LSD [49–51].

Basis sets

Further approximations have to be made when representing the wave functions in eq. (2.13). A basis set has to be chosen in order to expand the wavefunctions. A popular basis set for crystalline materials are plane waves,

$$\phi_{\mathbf{k},s} = \frac{1}{\sqrt{\Omega}} \mathrm{e}^{\mathrm{i}(\mathbf{k}+\mathbf{K}_s)\mathbf{r}} \tag{2.30}$$

as they fulfill Bloch's theorem for lattice periodic systems. Furthermore, they allow for an efficient transform between real and reciprocal space by means of fast Fourier transform (FFT). By using the kinetic energy of the plane waves,

$$E_s(\mathbf{k}) = \frac{\hbar^2}{2m} (\mathbf{k} + \mathbf{K}_s)^2 \ , \tag{2.31}$$

as a parameter, there exists a straightforward way to increase the number of basis functions and to check the convergence with respect to it: only plane waves $\phi_{\mathbf{k},s}$ whose kinetic energy is smaller than a defined cut-off energy,

$$E_s(\mathbf{k}) \leq E_{\mathrm{cutoff}} \ , \tag{2.32}$$

are used in the basis-set expansion. However, plane waves also exhibit a major disadvantage: describing localized orbitals, such as core electrons which are in close proximity to the ionic nuclei, requires a large number of plane waves.

To circumvent the complexity and numerical expenses related to a description of core electrons with plane waves, *pseudo-potentials* and *pseudo-wavefunctions* are used. Based on the perception that core electrons do not participate significantly in chemical bonding, they are not treated explicitly. Instead, all interactions between core and valence electrons, for instance their electrostatic and quantum-mechanical interactions, are replaced by a pseudo-potential. This pseudo-potential is required to coincide with the real potential outside a sphere of radius r_c, but it is much smoother inside this core region (see sketch in fig. 2.2). Moreover, the pseudo-potential is required to provide nodeless pseudo-wavefunctions for the valence electrons which reproduce the real wavefunctions outside the core region. Consequently, if they are constructed carefully, pseudo-potentials allow for an accurate description of the electronic structure while being computationally much more efficient than all-electron calculations. [37, 41]

Van der Waals corrections

In any system, the charge density can temporarily fluctuate, resulting in a temporal dipole moment. This dipole can now induce dipole moments in its environment. The interaction between these temporally induced dipole moments is called *van der Waals interaction* and is of particular importance for systems where covalent interactions are absent, such as dimers of noble gas atoms. On the other hand, it

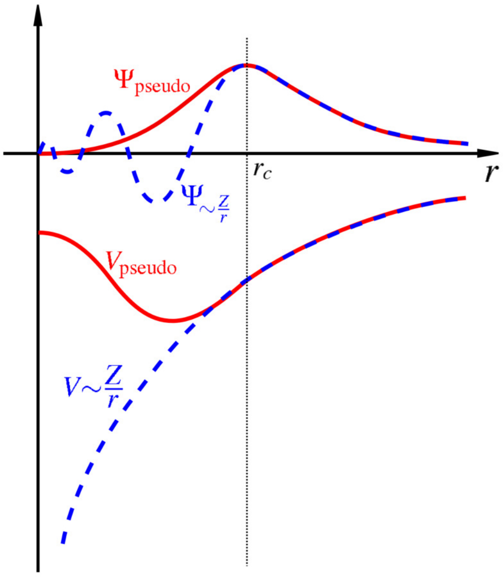

Figure 2.2.: Sketch illustrating the pseudo-wavefunction Ψ_{pseudo} and real wavefunction Ψ_ν, as well as pseudo-potential V_{pseudo} and Coulomb potential Z/r. Pseudo-wavefunction and pseudo-potential coincide with the real wavefuntion and potential for $r > r_c$. *Reprinted with permission from [52], released into the public domain.*

can be shown that van der Waals forces can contribute significantly for systems such as HaPs due to their polarizable atoms such as halides, Cs and organic molecules [1, 53–60]. It further can be shown that van der Waals interactions are non-local and decay with distance as r^{-6} in leading order. In semi-local DFT, however, this non-local interaction is not well described. Therefore, correction schemes have been developed and one popular correction scheme is the pair-wise correction suggested by TKATCHENKO AND SCHEFFLER (TS method) [61], which we will employ. There, the total energy obtained from DFT calculations E_{DFT} is complemented by a correction term E_{TS} to obtain the total energy E:

$$E = E_{\text{DFT}} + E_{\text{TS}} \ . \tag{2.33}$$

The correction term itself is a sum of pair-wise van der Waals interactions,

$$E_{\text{TS}} = -\frac{1}{2}\sum_{A,B}\frac{C_{6AB}}{R_{AB}^6} f(R_{AB}, R_A^0, R_B^0) \ , \tag{2.34}$$

with R_{AB} the distance between atoms A and B. This approximation depends on the C_6 parameters, van der Waals radii R_A^0 and R_B^0, and damping function $f(R_{AB}, R_A^0, R_B^0)$. This procedure of a pair-wise correction has been shown to significantly improve the results for structural properties of materials with significant dispersive contributions [62, 63].

2.2.2. Hellmann-Feynman theorem and forces on ions

Methods to study structural dynamics, like phonon calculations (section 2.3) or MD simulations (section 2.4) rely on knowing the forces acting on the nuclei. These forces can be obtained straightforwardly from the electronic ground-state calculated in DFT (section 2.2.1) with the use of the Hellmann-Feynman theorem. The theorem states how the derivative of the total energy E_λ with respect to a parameter λ can be calculated:

$$\frac{dE_\lambda}{d\lambda} = \langle\psi_\lambda| \frac{d\hat{\mathsf{H}}_\lambda}{d\lambda} |\psi_\lambda\rangle \ . \tag{2.35}$$

Applying this theorem to eq. (2.2) provides the forces acting on nucleus I:

$$F_I(\mathbf{R}_I) = \int d^3r \ n(\mathbf{r}) \ \frac{Z_I e^2(\mathbf{r}-\mathbf{R}_I)}{|\mathbf{r}-\mathbf{R}_I|^3} + \sum_{J\neq I} \frac{Z_I Z_J e^2(\mathbf{R}_I-\mathbf{R}_J)}{|\mathbf{R}_I-\mathbf{R}_J|^3} \ . \tag{2.36}$$

2.3. Lattice dynamics

2.3.1. Harmonic approximation: classical description

As motivated in section 2.1, the ionic nuclei only enter as parameters in the theory discussed in section 2.2. Moreover, up to here, the positions of the ionic nuclei are assumed to stay fixed. However, this assumption is only valid for classical particles in the limit $T \to 0$. At finite temperature (e.g., room temperature) atoms are moving. This is important to understand effects such as (thermal) transport, temperature dependent band gaps or superconductivity.

To describe nuclear motion theoretically, one approach is solving the classical equations of motion for the ionic nuclei in a potential V_nuclei. The potential energy V_nuclei of the nuclei can be rewritten in terms of pair-wise interactions:

$$V_\text{nuclei} = \sum_{I,J} V_{IJ}(\mathbf{R}_I - \mathbf{R}_J) \ . \tag{2.37}$$

In solids at room temperature, nuclear displacements $\mathbf{S}_I$ around their equilibrium positions $\mathbf{R}_I^0$ (cf. fig. 2.3), with

$$\mathbf{R}_I = \mathbf{R}_I^0 + \mathbf{S}_I = \mathbf{R}_n + \mathbf{R}_i + \mathbf{S}_I \ , \tag{2.38}$$

are often small. This motivates a Taylor expansion of the potential energy surface for the nuclei,

$$V_\text{nuclei} = V_\text{nuclei}^0 + \frac{1}{2}\sum_{I,J} \mathbf{S}_I \nabla^2 \, V_{IJ}(\mathbf{R}_I^0 - \mathbf{R}_J^0)\mathbf{S}_J + \mathcal{O}\left(\mathbf{S}_I^3\right) \tag{2.39}$$

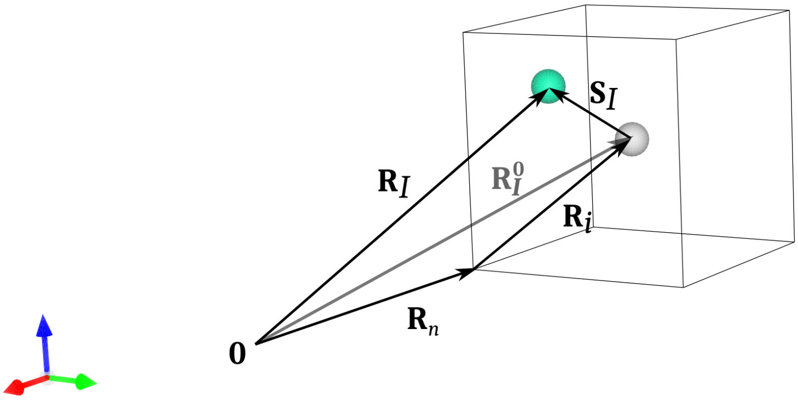

Figure 2.3.: Sketch of the notation used for describing atomic positions within a lattice in the context of the harmonic approximation of lattice dynamics. The (instantaneous) position vector $\mathbf{R}_I$ of atom I (cyan) is given as a sum of the vector $\mathbf{R}_n$ pointing to the unit cell,the vector $\mathbf{R}_i$ pointing to the undisplaced atom (gray) at its equilibrium position within the unit cell, and the displacement vector $\mathbf{S}_I$ defined by the vectors of undisplaced (gray) and displaced atom (cyan), cf. eq. (2.37). Similar, a sum of only the first to vectors provides the vector to the equilibrium position $\mathbf{R}_I^0$ of atom I: $\mathbf{R}_I^0 = \mathbf{R}_n + \mathbf{R}_i$.

and neglect terms of higher order than the quadratic term. The term linear in nuclear displacements vanishes, since at equilibrium there is no net force on the nuclei, i.e., $\sum_{I,J} \nabla V_{IJ}(\mathbf{R}_I^0 - \mathbf{R}_J^0) = 0$. As only the term quadratic in the displacements remains in this approximation, it is called the *harmonic approximation*. We call

$$\Phi_{IJ}^{\alpha\beta} = \left. \frac{\partial^2 V_{IJ}(\mathbf{R}_I - \mathbf{R}_J)}{\partial S_I^\alpha \, \partial S_J^\beta} \right|_{\{\mathbf{R}_I^0\}} \tag{2.40}$$

the *force constants*. The rewritten equations of motion for the nuclear displacements in the harmonic approximation,

$$M_I \frac{\partial^2 S_I^\alpha}{\partial t^2} = -\sum_{J,\beta} \Phi_{IJ}^{\alpha\beta} \, S_J^\beta \ , \tag{2.41}$$

can be solved using the plane wave ansatz

$$\mathbf{S}_I = \frac{1}{\sqrt{M_I}} \mathbf{A}_I(\mathbf{q}) \, \mathrm{e}^{\mathrm{i}(\mathbf{R}_n \cdot \mathbf{q} - \omega t)} \ , \tag{2.42}$$

with wavevector $\mathbf{q}$ and amplitude $\mathbf{A}(\mathbf{q})$. Inserting this ansatz, eq. (2.41) can be written as

$$M_I \frac{\partial^2}{\partial t^2} \left(\frac{1}{\sqrt{M_I}} A_I^\alpha(\mathbf{q}) \, \mathrm{e}^{\mathrm{i}(\mathbf{R}_n \cdot \mathbf{q} - \omega t)} \right) = -\sum_{J,m,\beta} \Phi_{IJ}^{\alpha\beta} \, \frac{1}{\sqrt{M_J}} A_J^\beta(\mathbf{q}) \, \mathrm{e}^{\mathrm{i}(\mathbf{R}_m \cdot \mathbf{q} - \omega t)} \tag{2.43}$$

$$-\omega^2 \sqrt{M_I} A_I^\alpha(\mathbf{q}) \, \mathrm{e}^{\mathrm{i}(\mathbf{R}_n \cdot \mathbf{q} - \omega t)} = -\sum_{J,m,\beta} \Phi_{IJ}^{\alpha\beta} \, \frac{1}{\sqrt{M_J}} A_J^\beta(\mathbf{q}) \, \mathrm{e}^{\mathrm{i}(\mathbf{R}_m \cdot \mathbf{q} - \omega t)} \tag{2.44}$$

$$-\omega^2 A_I^\alpha(\mathbf{q}) = -\frac{1}{\sqrt{M_I M_J}} \sum_{J,m,\beta} \Phi_{IJ}^{\alpha\beta}(\mathbf{q}) \, \mathrm{e}^{\mathrm{i}(\mathbf{R}_m - \mathbf{R}_n) \cdot \mathbf{q}} \, A_J^\beta \ . \tag{2.45}$$

And by introducing the *dynamical matrix*

$$D_{IJ}^{\alpha\beta}(\mathbf{q}) = \frac{1}{\sqrt{M_I M_J}} \sum_m \Phi_{IJ}^{\alpha\beta} \, \mathrm{e}^{\mathrm{i}(\mathbf{R}_m - \mathbf{R}_n)\cdot\mathbf{q}} \; , \tag{2.46}$$

this can be written as

$$-\,\omega^2(\mathbf{q})\mathbf{A}_I(\mathbf{q}) + \sum_{\beta,J} D_{IJ}^{\alpha\beta} A_J^{\beta}(\mathbf{q}) = 0 \; . \tag{2.47}$$

All non-trivial solutions of eq. (2.47) are thus given by the eigenfunctions of the dynamical matrix, with the eigenvalues $\omega_\nu^2(\mathbf{q})$ providing the vibrational frequencies $\omega_\nu(\mathbf{q})$ of the vibrational eigenmodes $\mathbf{e}_\nu(\mathbf{q})$, with

$$D(\mathbf{q})\mathbf{e}_\nu(\mathbf{q}) = \omega_\nu^2(\mathbf{q})\mathbf{e}_\nu(\mathbf{q}) \; . \tag{2.48}$$

The frequencies and eigenmodes are functions of the wavevector $\mathbf{q}$, hence we obtain *dispersion relations.* For a system consisting of 3N atoms, we find 3N branches of the dispersion relations. This is shown in fig. 2.4 for the example of Si. Figure 2.4 shows the phonon dispersion relation, i.e., the phonon frequencies along a path connecting the high-symmetry $\mathbf{q}$-points $\Gamma - K - X - \Gamma - L - X - W - L$ in the first Brillouin zone of Si as obtained from DFT calculations using three different XC-functionals (shown by black, blue, and yellow lines), as well as experimental data indicated by open circles. As the phonon dispersion was calculated for Si in the diamond-cubic structure, the unit cell contains two atoms and a total of six phonon branches can be seen. These six phonon branches consist of three acoustic phonon branches, identified by their linear behavior close to the Γ-point at which they are identically zero, and three optical branches.

Finally, we can write nuclear displacements, eq. (2.42), and velocities as functions of the eigenmodes $\mathbf{e}_\nu(\mathbf{q})$

$$\mathbf{S}_I(t) = \frac{1}{\sqrt{NM_I}} \sum_{\nu,\mathbf{q}} Q_\nu(\mathbf{q},t)\mathrm{e}^{i\mathbf{q}\mathbf{R}_n}\mathbf{e}_\nu^I(\mathbf{q}) \tag{2.49}$$

$$\dot{\mathbf{S}}_I(t) = \frac{1}{\sqrt{NM_I}} \sum_{\nu,\mathbf{q}} \dot{Q}_\nu(\mathbf{q},t)\mathrm{e}^{i\mathbf{q}\mathbf{R}_n}\mathbf{e}_\nu^I(\mathbf{q}) \; . \tag{2.50}$$

The coefficients $Q_\nu(\mathbf{q})$ are *normal coordinates* [39] and can be expressed as

$$Q_\nu(\mathbf{q},t) = \frac{1}{\sqrt{N}} \sum_{I,\mathbf{R}_0} \sqrt{M_I}\mathrm{e}^{-i\mathbf{q}\mathbf{R}_n}\mathbf{e}_\nu^{I*}(\mathbf{q}) \cdot \mathbf{S}_I(t) \tag{2.51}$$

$$P_\nu(\mathbf{q}) = \dot{Q}_\nu(\mathbf{q},t) = \frac{1}{\sqrt{N}} \sum_{I,\mathbf{R}_0} \sqrt{M_I}\mathrm{e}^{-i\mathbf{q}\mathbf{R}_n}\mathbf{e}_\nu^{I*}(\mathbf{q}) \cdot \dot{\mathbf{S}}_I(t) \; , \tag{2.52}$$

here $\mathbf{e}^*$ denotes the complex conjugate of the eigenvector $\mathbf{e}$. These normal coordinates will be helpful for a quantum mechanical description of lattice dynamics (section 2.3.2).

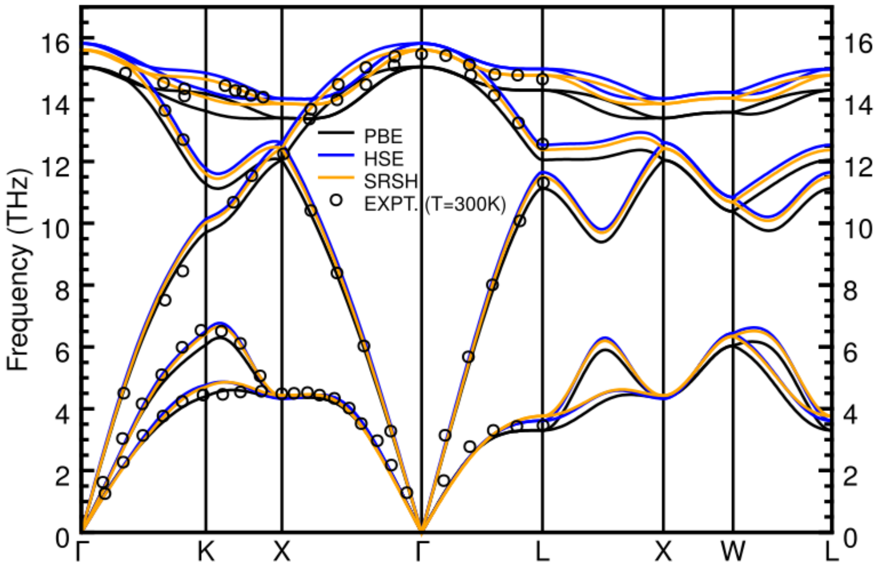

Figure 2.4.: Calculated phonon dispersion relations of diamond-cubic Si. Shown are results calculated using DFT with three different XC-functionals (solid lines), as well as experimental data extracted from [64, 65] (open circles). *Reprinted with permission from [4]. Copyright (2021) by the American Physical Society.*

In practice, elements of the force-constant matrix $\Phi_{IJ}^{\alpha\beta}$ can be computed by using finite differences, i.e., *finite displacements* ΔR_J^β of the atoms:

$$\Phi_{IJ}^{\alpha\beta} = \frac{F_I^\alpha(\mathbf{R}_I, \mathbf{R}_J + \Delta R_J^\beta) - F_I^\alpha(\mathbf{R}_I, \mathbf{R}_J)}{\Delta R_J^\beta} \ . \tag{2.53}$$

Here, $F_I^\alpha(\mathbf{R}_I, \mathbf{R}_J)$ is the α-component of the force $\mathbf{F}_I$ on nucleus I at position $\mathbf{R}_I$, with nucleus J at position $\mathbf{R}_J$. The forces $\mathbf{F}_I$ on the other hand can be calculated with the Hellmann-Feynman theorem (section 2.2.2). An implementation of the finite displacements approach as provided with the phonopy package [66] will later be used to compute harmonic phonon properties, as is described in section 2.6.

2.3.2. Harmonic approximation: quantum mechanical description

Following the classical derivation above, a Hamiltonian for the nuclei can be written within the harmonic approximation [39]

$$\hat{\mathsf{H}}_{\mathrm{harm}} = \sum_I \frac{\hat{\mathsf{p}}_I^2}{2M_I} + \frac{1}{2}\sum_{I,J} \mathbf{S}_I \hat{\Phi}_{IJ} \mathbf{S}_J \ . \tag{2.54}$$

This Hamiltonian can be rewritten using the normal coordinates, eqs. (2.51) and (2.52), as defined for the classical description

$$\hat{\mathsf{H}}_{\text{harm}} = \frac{1}{2}\sum_{\nu,\mathbf{q}} \left(\hat{\mathsf{P}}_{\nu}(\mathbf{q})\hat{\mathsf{P}}_{\nu}^{\dagger}(\mathbf{q}) + \omega_{\nu}^{2}(\mathbf{q})\hat{\mathsf{Q}}_{\nu}(\mathbf{q})\hat{\mathsf{Q}}_{\nu}^{\dagger}(\mathbf{q}) \right) \ , \tag{2.55}$$

Similar to a simple harmonic oscillator, usually discussed in the introductory quantum mechanics lecture, this can be solved by introducing creation and annihilation operators

$$\hat{\mathsf{a}}_{\nu}^{\dagger}(\mathbf{q}) = \frac{1}{\sqrt{2\hbar\omega_{\nu}(\mathbf{q})}} \left(\omega_{\nu}(\mathbf{q})\hat{\mathsf{Q}}_{\nu}^{\dagger}(\mathbf{q}) - i\hat{\mathsf{P}}_{\nu}^{\dagger}(\mathbf{q}) \right) \tag{2.56}$$

$$\hat{\mathsf{a}}_{\nu}(\mathbf{q}) = \frac{1}{\sqrt{2\hbar\omega_{\nu}(\mathbf{q})}} \left(\omega_{\nu}(\mathbf{q})\hat{\mathsf{Q}}_{\nu}(\mathbf{q}) + i\hat{\mathsf{P}}_{\nu}(\mathbf{q}) \right) \ . \tag{2.57}$$

The Hamiltonian can thus be rewritten as

$$\hat{\mathsf{H}}_{\text{harm}} = \sum_{\nu,\mathbf{q}} \hbar\omega_{\nu}(\mathbf{q}) \left(\hat{\mathsf{a}}_{\nu}^{\dagger}(\mathbf{q})\hat{\mathsf{a}}_{\nu}(\mathbf{q}) + \frac{1}{2} \right) = \sum_{\nu,\mathbf{q}} \hbar\omega_{\nu}(\mathbf{q}) \left(\hat{\mathsf{n}}_{\nu}(\mathbf{q}) + \frac{1}{2} \right) \ , \tag{2.58}$$

where the number operator $\hat{\mathsf{n}}_{\nu}(\mathbf{q}) = \hat{\mathsf{a}}_{\nu}^{\dagger}(\mathbf{q})\hat{\mathsf{a}}_{\nu}(\mathbf{q})$ has been introduced. It can be shown that the operator $\hat{\mathsf{a}}_{\nu}^{\dagger}(\mathbf{q})$, applied to an eigenstate $|\psi\rangle$ of the harmonic Hamiltonian,

$$\hat{\mathsf{H}}_{\text{harm}} |\psi\rangle = E |\psi\rangle \ , \tag{2.59}$$

increases the corresponding eigenenergy E by $\hbar\omega_{\nu}(\mathbf{q})$: $E \to E + \hbar\omega_{\nu}(\mathbf{q})$, i.e., it creates an excitation and thus it is called creation operator. Similarly, the operator $\hat{\mathsf{a}}_{\nu}(\mathbf{q})$ can be shown to annihilate an excitation of energy $\hbar\omega_{\nu}(\mathbf{q})$ and thus reduces the energy $E \to E - \hbar\omega_{\nu}(\mathbf{q})$. Therefore, the operator is called annihilation operator. These quantized vibrational excitations are called *phonons* and are considered to be vibrational quasiparticles. Finally, the number operator $\hat{\mathsf{n}}_{\nu}(\mathbf{q})$ counts the number $n_{\nu}(\mathbf{q})$ of excited phonons of energy $\hbar\omega_{\nu}(\mathbf{q})$. The eigenstates and eigenenergies of the Hamiltonian, eq. (2.58), can then be given by the respective number of phonons

$$\hat{\mathsf{H}}_{\text{harm}} |n_{\nu}(\mathbf{q})\rangle = \left(n_{\nu}(\mathbf{q}) + \frac{1}{2} \right) \hbar\omega_{\nu}(\mathbf{q}) |n_{\nu}(\mathbf{q})\rangle \ . \tag{2.60}$$

Before discussing the phonon occupation numbers, it is worth mentioning a peculiarity of the quantum mechanical picture: even in the absence of any phonons, i.e., $n_{\nu}(\mathbf{q}) = 0$ for all $\nu, \mathbf{q}$, the vibrational energy still is nonzero. As we will see below, this corresponds to $T = 0$ and in this case we will find the *zero-point energy*

$$E_0 = \sum_{\nu,\mathbf{q}} \frac{1}{2}\hbar\omega_{\nu}(\mathbf{q}) \ . \tag{2.61}$$

For finite temperatures, when phonons are excited, the phonon occupation number can be related to the amplitudes of nuclear displacements by taking the expectation value of the squared modulus of the normal mode operator $\hat{\mathsf{Q}}_{\nu}(\mathbf{q})$:

$$\langle n_{\nu}(\mathbf{q})| \hat{\mathsf{Q}}_{\nu}(\mathbf{q})\hat{\mathsf{Q}}_{\nu}^{\dagger}(\mathbf{q}) |n_{\nu}(\mathbf{q})\rangle = \frac{\hbar}{\omega_{\nu}(\mathbf{q})} \left(n_{\nu}(\mathbf{q}) + \frac{1}{2} \right) \ . \tag{2.62}$$

The actual number of excited phonons at a specific temperature T are given by the underlying statistics. As phonons are Bosons, they are described by a Bose-Einstein distribution. Specifically, the average number of phonons at temperature T is given by

$$\langle n_\nu(T)\rangle = \frac{1}{\mathrm{e}^{\hbar\omega_\nu/k_BT}-1} \; . \tag{2.63}$$

From this we clearly see that both the number of excited phonons and the amplitude of nuclei displacements increase with decreasing phonon frequencies. Consequently, the impact of phonons can be expected to be particularly important in soft materials with low vibrational frequencies, due to a higher number of excited phonons and larger nuclear displacements.

Vibrational density of states

Last but not least, for calculating phonon contributions to thermodynamic properties such as total energy, entropy, or heat capacity, the number of states per volume element and frequency range, i.e., the phonon density of states (PDOS) or vibrational density of states (VDOS) is of interest [39]. This density of states is useful whenever we have to evaluate a sum $\sum_{\nu,\mathbf{q}}$ over all possible phonon frequencies at all $\mathbf{q}$-points within the first Brillouin zone which, e.g., appears when calculating the phonon contributions to the above mentioned properties. Introducing the VDOS $g(\omega)$, the sum over modes and $\mathbf{q}$-points can be rewritten as an integral over frequencies

$$\sum_{\nu,\mathbf{q}} F[\omega_\nu(\mathbf{q})] = \frac{V}{(2\pi)^3}\sum_\nu \int d^3q\, F[\omega_\nu(\mathbf{q})] = \int d\omega\, g(\omega)\, F(\omega) \; . \tag{2.64}$$

From eq. (2.64), we can immediately identify

$$g(\omega) = \frac{V}{(2\pi)^3}\sum_\nu \int d^3q\, \delta\Big(\omega - \omega_\nu(\mathbf{q})\Big) \; . \tag{2.65}$$

In order to get $g(\omega)$ from the phonon dispersion relations $\omega(\mathbf{q})$ calculated earlier, the approximation

$$\frac{V}{(2\pi)^3}\int_{\mathbf{q}(\omega)}^{\mathbf{q}(\omega+\Delta\omega)} d^3q = \int_{\omega(\mathbf{q})}^{\omega(\mathbf{q})+\Delta\omega(\mathbf{q})} d\omega\, g(\omega) \simeq g(\omega)\Delta\omega \tag{2.66}$$

is used, i.e., an integration over infinitesimal volume fractions in reciprocal space with constant $\omega(\mathbf{q})$. This volume integral can be rewritten as an integral over the surface dS_q with constant ω times the change normal to this surface $dq_\perp$, using that the change perpendicular to the constant ω surface is given by $\Delta\omega = |\nabla_\mathbf{q}\omega(\mathbf{q})|\, dq_\perp$

$$d^3q = dS_q\, dq_\perp = dS_q \frac{\Delta\omega}{|\nabla_\mathbf{q}\omega(\mathbf{q})|} \; . \tag{2.67}$$

Comparing eq. (2.66) with eq. (2.67) allows to finally identify an expression of the VDOS based on the phonon dispersion relations $\omega(\mathbf{q})$ [35, 36]

$$g(\omega) = \frac{V}{(2\pi)^3} \int_{\omega=\text{const.}} \frac{dS_q}{|\nabla_{\mathbf{q}} \omega(\mathbf{q})|} \ . \tag{2.68}$$

It is important to note that although the VDOS has been motivated and derived from the phonon dispersions obtained from the harmonic approximation, the concept of a density of states still holds when the harmonic approximation breaks down and no phonon dispersions can be defined, e.g., in the case of liquids, similar to the case of electrons as discussed in reference [67].

2.3.3. Beyond the harmonic approximation

The harmonic approximation of lattice dynamics is already helpful in describing many phenomena at finite temperature. However, a variety of phenomena cannot be explained relying only on the harmonic approximation. These phenomena include, among others, thermal expansion and phonon-phonon interactions. While the former effect can be taken into account by a formalism called *quasi-harmonic approximation*, i.e., by treating thermal expansion and lattice dynamics as independent effects and explicitly performing calculations within the harmonic approximation at different volumes, the latter effect is more difficult to treat theoretically. Still, phonon-phonon interactions are important, e.g., to determine the lifetime of phonons. Within the harmonic approximation, a phonon that has been excited once will have an infinite lifetime. In order to calculate phonon-phonon interactions, and as a consequence finite vibrational lifetimes and further effects such as frequency shifts caused by anharmonicity, at least third order terms in the Taylor expansion of the potential energy surface for the nuclei, eq. (2.39), have to be taken into account. In terms of the creation and annihilation operators defined in section 2.3.2 third order terms can be written as

$$\frac{\hat{\boldsymbol{\Phi}}^{(3)}_{\nu\nu'\nu''}(\mathbf{q},\mathbf{q}',\mathbf{q}'')}{\sqrt{\omega_\nu(\mathbf{q})\omega_{\nu'}(\mathbf{q}')\omega_{\nu''(\mathbf{q}'')}}} \left(\hat{\mathsf{a}}_\nu(\mathbf{q}) + \hat{\mathsf{a}}^\dagger_\nu(\mathbf{q})\right) \left(\hat{\mathsf{a}}_{\nu'}(\mathbf{q}') + \hat{\mathsf{a}}^\dagger_{\nu'}(\mathbf{q}')\right) \left(\hat{\mathsf{a}}_{\nu''}(\mathbf{q}'') + \hat{\mathsf{a}}^\dagger_{\nu''}(\mathbf{q}'')\right) \ , \tag{2.69}$$

see, e.g., reference [39]. From eq. (2.69) it can be seen that anharmonic contribution can, in the framework of vibrational quasiparticles, be seen as phonon-phonon interactions as it contains, e.g., terms $\hat{\mathsf{a}}_\nu \hat{\mathsf{a}}_{\nu'} \hat{\mathsf{a}}^\dagger_{\nu''}$ where two phonons are annihilated and one is created. Similarly, also terms can be found where one phonon is annihilated and two phonons are created. In general, no exact solution exists for solving the resulting equations. Instead, approximations are used to compute (numerically) such higher order contributions. Higher order terms are for instance treated perturbatively (e.g., references [68, 69]), or using Green's functions (e.g., reference [70]). Another approach to obtain anharmonic material properties is to find an effective harmonic Hamiltonian. This Hamiltonian is quadratic in principle, but it is obtained such that anharmonic properties of a material are mimicked. To obtain this, the effective Hamiltonian is fitted, e.g., to MD simulations. Examples are given in references [71–73]. Besides creating an effective harmonic Hamiltonian, MD offers further ways to investigate anharmonic lattice dynamics, as will be discussed in section 2.4 and in particular section 2.4.3.

2.3.4. Vibrational spectroscopy

In order to study lattice vibrations experimentally, the interaction of phonons with a probe, e.g., photons or neutrons, is measured. Inelastic neutron spectroscopy allows for the accurate measurement of the **q** dependent vibrational frequencies, i.e., the phonon dispersion relation, with the disadvantage of requiring a neutron source. The latter disadvantage can be overcome by using photons as a probe, for instance using one of the two spectroscopy methods introduced below, as light sources are readily accessible.

Infra-red spectroscopy

Optical spectroscopy, i.e., using photons as a probe, allows only to measure phonons at the Γ-point due to the small momentum of photons. In the simplest case, light with a frequency corresponding to the phonon frequencies is used as a probe and absorbed by the sample. The absorbed frequencies provide the phonon frequencies. Due to the typical frequencies being in the infra-red (IR) region of the electromagnetic spectrum, this is usually called *IR-spectroscopy*. For a phonon mode to be measured with IR-spectroscopy, two requirements have to be met: first of all, the frequency of the light has to match the phonon frequency. And second, the phonon mode has to interact with the electromagnetic field of the light, i.e., the associated atomic vibration has to induce a change in the dipole moment of the sample. Because of the second requirement, only optical phonons can be probed by IR-spectroscopy. In theory, the infrared activity of a mode ν with Γ-point frequency ω_ν and (normalized) eigenvector $\hat{\mathbf{e}}_\nu$, can be calculated from the change of the macroscopic polarizability $\mathbf{P}$ with respect to the mode eigenvector [74–78]. Introducing the *Born effective charges* [78, 79]

$$Z^*_{\alpha\beta}(i) = \Omega_0 \frac{\partial P_\alpha}{\partial S_\beta(i)} \, , \tag{2.70}$$

where Ω_0 is the unit cell volume, α, β denote Cartesian coordinates, and i labels atom number i, the infrared activity can be written as [74, 76–78]

$$I(\omega_\nu) = \sum_\alpha \left| \sum_i \sum_\beta Z^*_{\alpha,\beta}(i)\, \hat{\mathbf{e}}^\beta_\nu(i) \right|^2 \, . \tag{2.71}$$

To include effects observed in experiment, such as the finite linewidth of the absorption peaks, effects going beyond the harmonic approximation have to be taken into account. This can, e.g., be done using MD (see section 2.4) by analyzing correlation functions of the dipole moment (cf. section 2.4.2).

Raman spectroscopy

A complementary optical method to probe phonon frequencies at the Γ-point is *Raman spectroscopy.* Raman spectroscopy allows to probe structural dynamics by inelastic scattering of light with the material. Due to the scattering, the frequency of the outgoing light changes with respect to the incident monochromatic light. The Raman shift, i.e., the frequency shift is determined by the phonon energy. For a shift towards lower frequencies (Stokes) a phonon is excited. If the frequency of the scattered light changes towards higher frequencies (Anti-Stokes) a phonon has been annihilated. The ratio of Stokes and Anti-Stokes intensities is determined by the population of the phonon modes, with Stokes intensities usually being higher as it is more likely to create an phonon than to find a populated phonon that can be annihilated. Theoretically, Raman spectra can be calculated from the change of the polarizability tensor $\hat{\alpha}$ with respect to the phonon eigenvector [74, 75, 78] or, in an MD approach, from the velocity autocorrelation function of the polarizability [80, 81]. However, in this work no theoretical Raman spectra have been calculated. Instead, experimentally obtained Raman spectra were compared to the VDOS obtained from MD simulations in the case of AgI (cf. sections 2.4.2 and 4.2).

2.3.5. Relaxational motion

There are two special situations of the theoretical framework introduced above that are of particular interest for the scope of this work. These situations are connected to a particular type of structural dynamics, which we call *relaxational motion.* In this context, relaxational motion describes a motion that – in contrast to vibrational motion – implies long-lasting changes in the nuclear positions.

The first case is the scenario where an eigenvalue of the dynamical matrix, cf. eq. (2.48), is negative, i.e.,

$$\omega_\nu^2(\mathbf{q}) = -\left|\omega_\nu^2(\mathbf{q})\right| \ . \tag{2.72}$$

In this case the vibrational “frequency” gets imaginary

$$\omega_\nu(\mathbf{q}) = \mathrm{i}\left|\omega_\nu(\mathbf{q})\right| \ , \tag{2.73}$$

and the oscillatory nuclear motion in eq. (2.42) becomes exponential

$$\mathbf{S}_I = \frac{1}{\sqrt{M_I}}\mathbf{A}_I(\mathbf{q})\,\mathrm{e}^{\mathrm{i}\mathbf{R}_n\cdot\mathbf{q}}\ \mathrm{e}^{-\mathrm{i}\omega_\nu t} = \frac{1}{\sqrt{M_I}}\mathbf{A}_I(\mathbf{q})\,\mathrm{e}^{\mathrm{i}\mathbf{R}_n\cdot\mathbf{q}}\ \mathrm{e}^{|\omega_\nu|t} \ . \tag{2.74}$$

Consequently, getting an imaginary phonon mode from a (DFT) calculation – excluding numerical issues [82] – implies that displacing nuclei according to the eigenvector of this mode actually results in a structure with lower total energy, i.e., the structure is unstable with respect to this mode. This might imply that the structure used for phonon calculations is not the actual equilibrium structure (in particular, in DFT calculations the geometry might not have been optimized properly) but it might also imply that there is a structural phase transition related to this phonon

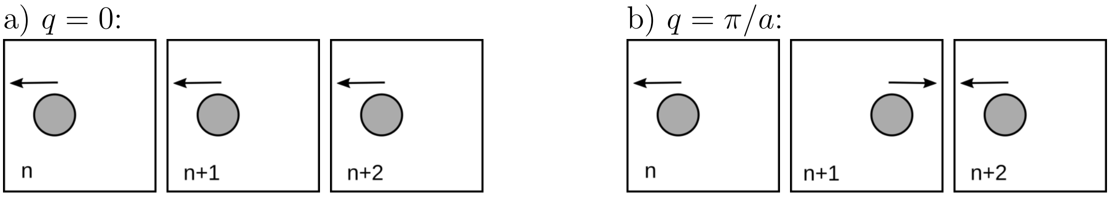

Figure 2.5.: Sketch of atomic motion (of a system with one atom per unit cell and lattice parameter a) in unit cells n, $n+1$, and $n+2$ for vibrations located at different points in reciprocal space. **a)** at the Γ-point ($q = 0$), the atoms of all unit cells move in phase. If the sketched phonon mode would correspond to an imaginary frequency, the lower energy structure could be obtained by optimizing one unit cell. **b)** at $q = \pi/a$, the atoms move with a phase difference of π. If the sketched phonon mode would correspond to an imaginary frequency, the lower energy structure could not be obtained by optimizing only one unit cell as the head-to-head motion (accompanied by a variation of the interatomic distance) could not be mimicked.

mode. For judging whether an imaginary mode obtained from a DFT calculation might be related to an improper geometry optimization, its location in reciprocal space provides helpful information. According to eqs. (2.42) and (2.74) and the translational periodicity of a crystalline material, the motion of nucleus I in unit cells n and m differs by their phase factor $exp\left(\mathrm{i}\mathbf{R}_n \cdot \mathbf{q}\right)$, where $\mathbf{q}$ is the location of the mode in reciprocal space. In particular, at the Γ-point, i.e., $\mathbf{q} = (0,0,0)^T$ this phase factor is 1 for all atoms, i.e., all atoms move in phase. Consequently the motion can be represented within only a single unit cell. This suggests that the unit cell geometry with lowest total energy has not been found during the geometry optimization procedure. In contrast, for any $\mathbf{q} \neq \Gamma$, the motion of nuclei in different unit cells differs by their phase and more than one unit cell might be required to mimic the motion lowering the total energy of the structure. This has been sketched in fig. 2.5. There, two possible nuclear motions are sketched for an example with one atom per unit cell. The motion in fig. 2.5a resembles a Γ-point motion as the atoms in all sketched unit cells $n \ldots n+2$ move in phase. According to the above discussion, if this motion corresponded to an imaginary frequency, the lower energy structure could be obtained by optimizing a single unit cell. In fig. 2.5b, the contrasting case of atoms with a phase difference of π between unit cells has been sketched. This portraits a phonon mode located at Brillouin zone boundary in reciprocal space. As the head-to-head motion cannot be mimicked using only the one atom of one unit cell, the lower energy structure could not be obtained by optimizing atoms in one unit cell, in case this motion was associated with an imaginary frequency. In plots of the phonon dispersion, imaginary frequencies are usually plotted as negative values, i.e., “negative frequencies”.

A second phenomenon that can be understood as relaxational motion are *zero frequency*, i.e., $\omega = 0$ modes, as they, e.g., are measured in Raman spectroscopy. As the frequency of a single harmonic oscillator $\omega = \sqrt{f/m}$ can be directly linked to the force constant f (m is the mass of the oscillator, see eqs. (2.40) to (2.42) and (2.46) to (2.48) for a generalization), zero frequency implies no restoring force. Thus, zero frequency modes imply nuclear motion without restoring force, i.e., relaxational motion.

On the other hand, zero frequency Raman modes can also be be understood as modes with finite frequency that are overdamped, which is helpful to understand, e.g., symmetries still connected with these modes (see also section 2.3.4 and section 4.3). The peak-shape of the intensity I of a Raman active phonon mode with frequency ω_ν, and thus the response of a crystal to a corresponding excitation, can be modeled using a damped Lorentzian oscillator as can be obtained from the fluctuation-dissipation theorem [83]

$$I_\nu(\omega) = c_\nu \; n_{\mathrm{BE}}(\omega) \frac{\gamma_\nu \omega}{\omega^2 \gamma_\nu^2 + (\omega^2 - \omega_\nu^2)^2} \; , \tag{2.75}$$

with c_ν being the intensity coefficient and γ_ν the damping of the oscillator. From this, the well-known Lorentzian peak-shape

$$I_\nu(\omega) = \frac{1}{2} c_\nu \; n_{\mathrm{BE}}(\omega) \frac{\gamma_\nu / 2}{(\gamma_\nu/2)^2 + (\omega^2 - \omega_\nu^2)} \; , \tag{2.76}$$

used to model peaks in spectroscopy, can be obtained as the low γ_ν limit [83]. In this context, however, we are interested in the high-damping limit. In fig. 2.6, the evolution of a peak modeled with a damped-Lorentzian, eq. (2.75), and resonance frequency ω_0 is shown. The plot shows the intensity $I(\omega)$ as a function of the normalized frequency ω/ω_0 for three different damping parameters $\gamma = 0.5\omega_0$ (blue line), $\gamma = \omega_0$ (green line), and $\gamma = 2\omega_0$ (orange line). It can be observed that the peak broadens and at the same time shifts towards lower energies if the damping is increased. In the extremely over-damped case (here: $\gamma = 2\omega_0$), the curve has a peak with resonance frequency $\tilde{\omega}_0 \approx 0$ instead of the underlying finite resonance frequency ω_0. In this sense, a zero-frequency motion can be understood as evolving from an over-damped regular mode: in the extreme case, a full oscillation is not completed and thus the nuclear motion can be considered not to be oscillatory anymore. This is consistent with the above picture of relaxational motion. Yet, it helps to understand the (possible) presence of symmetries associated with the peak as the nuclear motion remains the same as for the regular mode. In the overdamped limit, the peak can be modeled with a Debye relaxor [83]

$$I_0(\omega) = c_0 \; n_{\mathrm{BE}}(\omega) \frac{\gamma_0 \omega}{\gamma_0^2 + \omega^2} \tag{2.77}$$

to obtain the damping factor that is related to the width of the peak and the characteristic timescale of the relaxational motion.

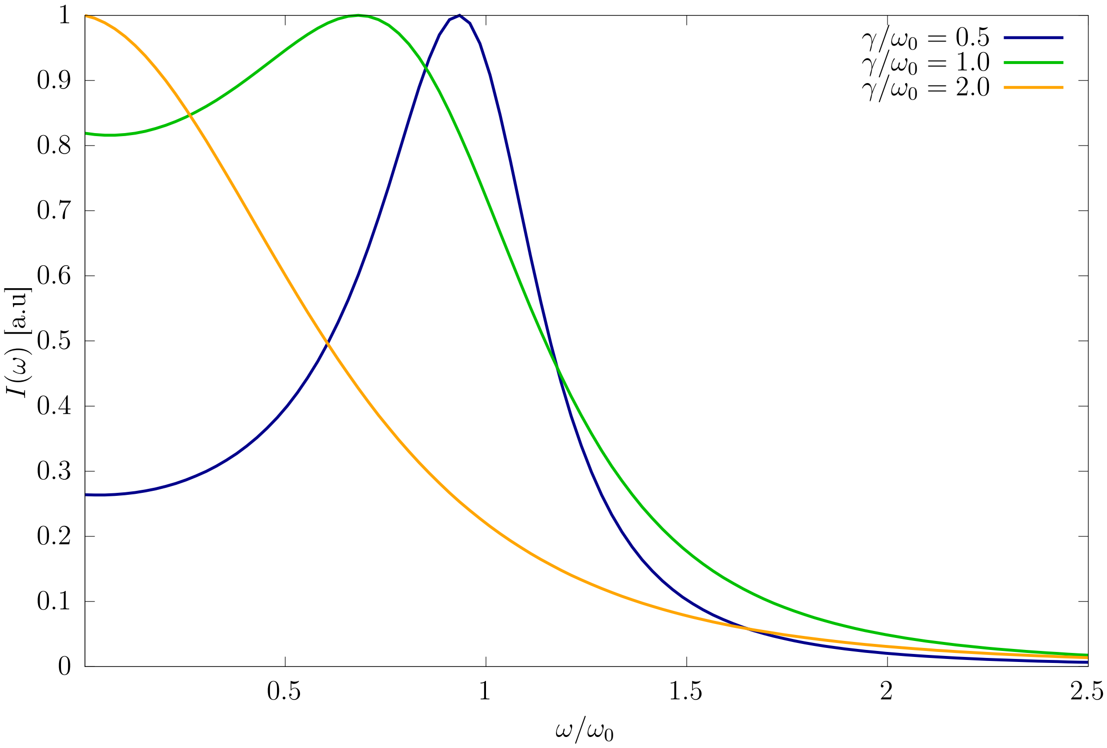

Figure 2.6.: Sketch of the Raman intensity $I(\omega)$ according to the model eq. (2.75) for a mode with frequency ω_0 and for different damping parameters γ. The temperature for the Bose-Einstein factor $n_{\mathrm{BE}}(\omega)$ is set such that to $\hbar\omega_0/k_B T = 0.25$.

2.4. Molecular dynamics (MD)

2.4.1. Fundamentals

In order to study the phenomena discussed in sections 2.3.3 and 2.3.5, a theoretical framework going beyond the approximations introduced in sections 2.3.1 and 2.3.2 is required. Assuming one can treat nuclei as classical particles around room temperature, one approach is to iteratively solve Newton's equations of motion for the nuclei

$$\frac{d^2}{dt^2}\mathbf{R}_I(t) = \frac{\mathbf{F}_I(t)}{M_I} = -\frac{1}{M_I}\nabla_{\mathbf{R}_I} V(\{\mathbf{R}_I\}) \ . \tag{2.78}$$

This approach to simulate finite temperature dynamics is called molecular dynamics (MD). The equations of motion are solved starting from forces which are provided either by a "higher level" theory or from a parametrization. The first case is called *first-principles MD* and the forces can be obtained from the electronic ground-state as calculated, e.g., using DFT as discussed in section 2.2.2, eq. (2.36). The latter case is called *force-field MD* and forces are obtained from a parametrization of the potential energy surface

$$V(\{\mathbf{R}_I\}) \approx V_{FF}(\{\mathbf{R}_I\}) = \sum_I v_1(\mathbf{R}_I) + \sum_{I,J} v_2(\mathbf{R}_I, \mathbf{R}_J) + \sum_{I,J,K} v_3(\mathbf{R}_I, \mathbf{R}_J, \mathbf{R}_K) + \dots \ , \tag{2.79}$$

with v_1, v_2, …, v_n the one-body, two-body, …, n-body contributions to the potential. For instance, the SSIC α-AgI has successfully been described [84] using only two-body potentials of the form

$$V_{FF}(\{\mathbf{R}_I\}) = \sum_{I,J}\left[\frac{A_{IJ}\,(\sigma_I+\sigma_J)^n}{|\mathbf{R}_I-\mathbf{R}_J|^n} + \frac{Z_I Z_J e}{|\mathbf{R}_I-\mathbf{R}_J|} - \frac{(\alpha_I Z_I^2 + \alpha_J Z_J^2)\,e^2}{2\,|\mathbf{R}_I-\mathbf{R}_J|^4} - \frac{W_{IJ}}{|\mathbf{R}_I-\mathbf{R}_J|^6}\right] , \tag{2.80}$$

with repulsive strength A_{IJ}, particle radii σ_I, polarizabilities α_I, and nuclei charges $Z_I e$. The specific parameters for applying eq. (2.80) to α-AgI can be found in reference [84]. Naturally, the force-field includes additional terms if more complex materials, such as hybrid organic-inorganic HaPs are to be described. For instance the force-fields used to describe MAPbBr_3 [85] and MAPbI_3 [86] consist of three parts

$$V_{FF}(\{\mathbf{R}_I\}) = V_{II}(\{\mathbf{R}_I\}) + V_{IO}(\{\mathbf{R}_I\}) + V_{OO}(\{\mathbf{R}_I\}), \tag{2.81}$$

to describe the interactions of the inorganic PbX_3 framework (V_{II}) the organic methylammonium (MA) molecule (V_{OO}) and the interaction between organic molecule and inorganic framework (V_{IO}). The interactions between inorganic atoms as well as between inorganic framework and organic molecule are described by two-body terms, describing electrostatic and dispersive interactions complemented by Pauli repulsion,

$$V_{II}(\{\mathbf{R}_I\}) = \sum_{I,J}\left[\frac{Z_I Z_J e^2}{|\mathbf{R}_I-\mathbf{R}_J|} - \frac{C_{IJ}}{|\mathbf{R}_I-\mathbf{R}_J|^6} + f B_{IJ}\, e^{(A_{IJ}-|\mathbf{R}_I-\mathbf{R}_J|)/B_{IJ}}\right] \tag{2.82}$$

with parameters A_{IJ}, B_{IJ} and C_{IJ}, and

$$\begin{aligned} V_{IO}(\{\mathbf{R}_I\}) = \sum_{I,J} \Bigg\{ & \frac{1}{4\pi\epsilon_0} \frac{Z_I Z_J}{|\mathbf{R}_I - \mathbf{R}_J|} - \frac{\sigma_{IJ}}{|\mathbf{R}_I - \mathbf{R}_J|^6} + A_{IJ}\, e^{-|\mathbf{R}_I - \mathbf{R}_J|/\rho_{IJ}} \\ & + \epsilon_{IJ} \left[\left(\frac{s_{IJ}}{|\mathbf{R}_I - \mathbf{R}_J|} \right)^{12} - \left(\frac{s_{IJ}}{|\mathbf{R}_I - \mathbf{R}_J|} \right)^{6} \right] \Bigg\} \end{aligned} \tag{2.83}$$

with parameters σ_{IJ}, A_{IJ}, ρ_{IJ}, ϵ_{IJ}, and s_{IJ}. The potential to describe the organic MA molecule further includes additional two-body contributions taking into account the atomic bonds b, three-body contributions parameterized as (harmonic) angles θ, and four-body contributions as torsion ϕ [87]

$$\begin{aligned} V_{OO}(\{\mathbf{R}_I\}) = & \sum_{\text{bonds}} k_b (b - b_0)^2 + \sum_{\text{angles}} k_\theta (\theta - \theta_0)^2 + \sum_{\text{torsions}} k_\phi \left(\cos(n\phi + \delta) + 1\right) \\ & + \sum_{\text{nonbond}} \frac{q_I q_J}{|\mathbf{R}_I - \mathbf{R}_J|} + \left(\frac{A_{IJ}}{|\mathbf{R}_I - \mathbf{R}_J|} \right)^{12} - \left(\frac{C_{IJ}}{|\mathbf{R}_I - \mathbf{R}_J|} \right)^{6} , \end{aligned} \tag{2.84}$$

with the force-field parameters k_b, k_θ, and k_ϕ, as well as A_{IJ} and C_{IJ}.

Once the force $\mathbf{F}_I^t = -\nabla_{\mathbf{R}_I} V^t(\{\mathbf{R}_I\})$ on atom I at time t is know from either of the methods described above, Newton's equation of motion, eq. (2.78), can be integrated numerically using, e.g., the Verlet algorithm [88]

$$\mathbf{R}_I^{t+\Delta t} = 2\mathbf{R}_I^t - \mathbf{R}_I^{t-\Delta t} + \frac{\mathbf{F}_I^t}{M_I} \Delta t^2 , \tag{2.85}$$

for which the next position $\mathbf{R}_I^{t+\Delta t}$ can be determined from knowing the current position $\mathbf{R}_I^t$ and the previous position $\mathbf{R}_I^{t-\Delta t}$. Here, Δt is the timestep of the numerical integration that will further be discussed below. Alternatively, if instead of storing the previous position, only the current position and the current velocity $\mathbf{v}_I^t$ are stored, a velocity Verlet algorithm can be used [89]:

$$\mathbf{R}_I^{t+\Delta t} = \mathbf{R}_I^t + \mathbf{v}_I^t \Delta t + \frac{\mathbf{F}_I^t}{2M_I} \Delta t^2 \tag{2.86}$$

$$\mathbf{v}_I^{t+\Delta t} = \mathbf{v}_I^t + \frac{\mathbf{F}_I^t + \mathbf{F}_I^{t+\Delta t}}{2M_I} \Delta t . \tag{2.87}$$

From this, the trajectory of the system, i.e., a time-series of the positions of all atoms during the simulated time-frame can be obtained, and with this all quantities that rely on either the positions or the velocities of the atoms.

As can be seen from eqs. (2.85) to (2.87), and is indicated by writing $\mathbf{R}_I^t$ instead of $\mathbf{R}_I(t)$, our solution of the equations of motion are only obtained for discrete timesteps $n \times \Delta t$. Thus, the timestep Δt has to be chosen very carefully. The specific choice depends on both, the system and the phenomena of interest. On one hand, choosing a large timestep allows to calculate long trajectories and observe slow phenomena with reasonable computational expenses. On the other hand, fast motion has to be described accurately in order to obtain physically and numerically meaningful trajectories. Typically, the timestep has to be a few percent of the vibrational period of the fastest, i.e., highest frequency, motion. For instance, DOVE suggest not to exceed 5% of the shortest vibrational period [39]. Consequently, in most cases the timestep will be chosen as large as possible but as small as necessary.

This scheme simulates a microcanonical (NVE) ensemble, i.e., the number of particles N, the volume V of the system, and the total energy E are conserved. To achieve the latter, algorithms that are designed to conserve the total energy of the system are applied to numerically integrate the equations of motion, for instance the algorithms based on eq. (2.85) or eqs. (2.86) and (2.87).

However, usually one is interested in the finite temperature properties of the system studied. In order to obtain this, the temperature has to be set and controlled. A popular definition for the temperature in MD simulations is based on the average kinetic energy, motivated by the equipartition theorem [90]

$$T = \frac{2}{k_B N_f} \langle E_{\mathrm{kin}} \rangle = \frac{2}{k_B N_f} \left\langle \sum_I \frac{M_I}{2} \mathbf{v}_I^2 \right\rangle , \tag{2.88}$$

with N_f the number of degrees of freedom. As with this definition the temperature is related to the average kinetic energy of the system, the most straightforward way to fix the (instantaneous) temperature T_t is to rescale all velocities,

$$\mathbf{v}_I(t) = \sqrt{\frac{T_t}{T_{\mathrm{set}}}} \mathbf{v}_I(t) . \tag{2.89}$$

In practice, however, one wants to simulate a thermodynamic ensemble, e.g., the canonical ensemble (constant particle number N, constant volume V, and constant temperature T), including its fluctuations. In “MD language” ensembles are named after the fixed variables, e.g., the canonical ensemble is called the NVT ensemble. This canonical ensemble is introduced in statistical mechanics lectures by the coupling of a microcanonical ensemble (NVE ensemble) to a heat bath. This coupling to an external bath can also be mimicked in MD simulations to introduce a thermostat, e.g., the Nosé-Hoover thermostat [91, 92]. In the Nosé-Hoover thermostat the bath is introduced to the Hamiltonian of the system by an additional degree of freedom s, with momentum p_s and “mass” Q. As will be shown below, this additional degree of freedom finally acts like a friction term $-\zeta \mathbf{p}_I$ in the equation of motion for the momentum designed to keep the total kinetic energy constant [91, 92]:

$$\frac{d}{dt} \mathbf{p}_I = -\nabla_{\mathbf{R}_I} V(\{\mathbf{R}_I\}) - \zeta \mathbf{p}_I . \tag{2.90}$$

In order to obtain this equation, Nosé [91] introduced a set of virtual variables $(\mathbf{R}'_I, \mathbf{p}'_I, t')$ using a transformation that can be understood as transformation to a system with scaled time:

$$\mathbf{R}'_I = \mathbf{R}_I \ , \tag{2.91}$$

$$\mathbf{p}'_I = \mathbf{p}_I \, s \ , \tag{2.92}$$

$$p'_s = p_s \, s \ , \tag{2.93}$$

$$dt' = s \, dt \ . \tag{2.94}$$

Further, he postulated the following Hamiltonian for the extended system:

$$H_{\text{Nose}} = \sum_I \frac{1}{2M_I} \frac{{\mathbf{p}'_I}^2}{s^2} + V(\{\mathbf{R'}_I\}) + \frac{{p'_s}^2}{2Q} + Lk_B T \ln(s) \ , \tag{2.95}$$

in which the logarithmic potential for s, $Lk_BT\ln(s)$, ensures reproducing a canonical ensemble for the physical system [91]. Applying the Hamilton formalism

$$\frac{d\mathbf{R}'_I}{dt} = \frac{dH_{\text{Nose}}}{d\mathbf{p}'_I} \ , \quad \frac{d\mathbf{p}'_I}{dt} = -\frac{dH_{\text{Nose}}}{d\mathbf{R}'_I} \tag{2.96}$$

$$\frac{ds}{dt} = \frac{dH_{\text{Nose}}}{d\mathbf{p}'_s} \ , \quad \frac{dp'_s}{dt} = -\frac{dH_{\text{Nose}}}{ds} \ , \tag{2.97}$$

and transforming back to the real variable, modified equations of motion can be derived [91]:

$$\frac{d}{dt}\mathbf{R}_I = \frac{\mathbf{p}_I}{M_I} \ , \tag{2.98}$$

$$\frac{d}{dt}\mathbf{p}_I = -\nabla_{\mathbf{R}_I} V(\{\mathbf{R}_I\}) - \frac{s p_s}{Q} \mathbf{p}'_I \ , \tag{2.99}$$

$$\frac{d}{dt} s = \frac{s^2 p_s}{Q} \ , \tag{2.100}$$

$$\frac{d}{dt} p_s = \frac{1}{s} \left(\sum_I \frac{\mathbf{p}_I^2}{M_I} - Lk_B T \right) - \frac{s {p'_s}^2}{Q} \ . \tag{2.101}$$

As seen in the equations, eq. (2.99) is equivalent to eq. (2.90), with a friction term that couples the additional degree of freedom s to the degrees of freedom of the real system. Therefore energy is transferred between system and bath allowing a canonical ensemble for the real system while conserving the total energy for the extended system. However, as a consequence of the way the system exchanges energy with the bath, it is not always and instantaneously at the correct temperature. Instead, the temperature fluctuates during MD simulations of an NVT ensemble. The energy transfer, and thus also the frequency of the temperature fluctuations, is determined by the coupling between system and bath that has to be tuned via the variable Q. Note that there also exist other thermostats, such as the procedures suggested by Andersen [93], Berendsen et al. [94] and Langevin thermostats, e.g., references [95, 96].

Similarly, it is often useful to simulate an isothermal-isobaric NPT ensemble. And consequently, there exists a number of approaches to control pressure during the MD simulations. Examples for barostats are provided in references [93, 94, 97, 98]. The research that was conducted here, however, focused on NVT simulations applying a Nosé-Hoover thermostat.

An accurate simulation of a system in a chosen ensemble usually includes the below steps [40, 99]. After carefully preparing the starting point of the MD simulation, e.g., by using nuclear coordinates obtained from a minimization of the total energy of the system and assigning random velocities that are Maxwell-Boltzmann distributed, the system has to evolve for some time until a steady state is reached and potential and kinetic energy are partitioned correctly. This part of an MD simulation is called equilibration, and its goal is to have the system evolved to the target energy, temperature, pressure, or volume – depending on the target ensemble – and to discard any influence of the starting configuration. The simulation time necessary to achieve this goal can hardly be predicted beforehand, instead the important variables have to be monitored during the equilibration run. However, once this has been achieved, the production run can be performed, i.e., the part of the MD simulation that describes the target system (e.g., in terms of temperature, volume, etc.) and actually should be analyzed. The production run can then be analyzed, for instance, by using statistical methods as explained below in section 2.6.1. Caution has to be taken that the results of the analysis are converged with respect to the simulation length.

2.4.2. Correlation functions

MD simulations provide a huge amount of output data, since usually the trajectories of large numbers of atoms are computed for a large number of timesteps. In order to analyze this large amount of data, statistical methods are applied. Since in practice *ergodicity* is assumed, statistics can be calculated over the ensemble of atoms and over time. Statistical quantities to be computed include for instance (probability) distributions, such as the velocity distribution which is expected to resemble a Maxwell-Boltzmann distribution even in solids [100]. But moreover, *correlation functions* can be employed to analyze MD trajectories. In particular, autocorrelation functions provide the spatial or temporal relationship between one instance of an observable A and an instance of the same variable shifted in space or time. Three autocorrelation functions particularly helpful to analyze structural dynamics in a material within the context of this work are the *mean-squared displacement (MSD)*, the *velocity autocorrelation function (VACF)*, and the dipole-dipole autocorrelation function.

Mean-squared displacement (MSD)

The MSD, defined as

$$\mathrm{msd}(\Delta t) = \left\langle \left(\mathbf{r}(t+\Delta t) - \mathbf{r}(t)\right)^2 \right\rangle \ , \tag{2.102}$$

provides a measure for the average absolute distance traveled by an atom after a lag time Δt. For usual crystalline materials, in which the nuclei are (harmonically) bound to an equilibrium position, the MSD will fluctuate around a (system and temperature dependent) constant value. In contrast, for fluid materials the MSD is increasing linearly with time, with the slope given by the *diffusion constant* D:

$$\mathrm{msd}(t) = 2nDt \quad (n: \text{ dimensionality}) \; . \tag{2.103}$$

In return, a motion with linear MSD is called *diffusion*. Strikingly, in the case of SSICs, the conducting ion species is also diffusing while the rest of the material is in a crystalline phase. As a consequence, while most atomic species of the material show a more or less constant MSD, one species shows a linearly increasing MSD. Furthermore the diffusion constant determines the magnitude of the ion diffusion and thus the magnitude of the ion conduction. We will thus use the MSD to quantify ionic motion in the SSIC material AgI.

Velocity autocorrelation function (VACF)

The VACF, defined as

$$\mathrm{vacf}(\Delta t) = \langle \mathbf{v}(t) \cdot \mathbf{v}(t + \Delta t) \rangle \; , \tag{2.104}$$

provides information about temporal correlations of the nuclear velocity with itself. In particular, it can be shown [101] that the power-spectrum of the VACF resembles the VDOS

$$\mathrm{vdos}(\omega) = \frac{N}{V} \int_{-\infty}^{\infty} dt \; \mathrm{e}^{i\omega t} \; \frac{\mathrm{vacf}(t)}{\mathrm{vacf}(0)} \; , \tag{2.105}$$

where N is the number of atoms and V the volume of the system. Moreover, we can rewrite eq. (2.102) as

$$\mathrm{msd}(\Delta t) = \left\langle \left(\int_t^{\Delta t} dt' \; \mathbf{v}(t') \right)^2 \right\rangle = \int_t^{\Delta t} dt' \int_t^{\Delta t} dt'' \; \langle \mathbf{v}(t') \cdot \mathbf{v}(t'') \rangle \tag{2.106}$$

$$= 2 \int_t^{\Delta t} dt' \int_t^{t'} dt'' \; \langle \mathbf{v}(t') \cdot \mathbf{v}(t'') \rangle \; , \tag{2.107}$$

i.e., we can rewrite the MSD in terms of the VACF (see also, e.g., [101]) and finally obtain for the diffusion constant

$$D = \frac{1}{3} \int_0^t dt \; \mathrm{vacf}(t) = \frac{1}{6} \int_{-t}^t dt \; \mathrm{vacf}(t) = \frac{1}{6} \mathcal{F}[\mathrm{vacf}(t)](\omega = 0) \; . \tag{2.108}$$

I.e., the diffusion constant can be obtained from the zero-frequency component of the Fourier transform $\mathcal{F}$ of the VACF. Thus the VACF offers two important observables for our analysis of structural dynamics: an alternative way to calculate the diffusion constant on one hand, and on the other hand the VDOS of a system from MD, i.e., the VDOS including anharmonicity up to any order of the Taylor expansion for the potential energy surface of the nuclei.

Dipole-dipole autocorrelation function

Similar to the VACF an autocorrelation function $\langle \mathbf{M}(t) \cdot \mathbf{M}(t+\Delta t) \rangle$ can be defined for the electric dipole moment $\mathbf{M}$. This dipole-dipole autocorrelation function is related to the infra-red (IR) absorption coefficient $\alpha(\omega)$ [80, 102–104]:

$$\alpha(\omega) n(\omega) = \frac{2\pi\omega \left(1 - \mathrm{e}^{-\hbar\omega/k_B T}\right) D(\omega)}{3\hbar c V} \int_{-\infty}^{\infty} dt \ \mathrm{e}^{\mathrm{i}\omega t} \ \langle \mathbf{M}(t) \cdot \mathbf{M}(t+\Delta t) \rangle \ . \tag{2.109}$$

Here, $n(\omega)$ is the frequency dependent refractive index, c is the speed of light and V is the volume. Since classical MD, i.e., solving Newton's equations of motion for the ions (see section 2.4), will be applied to obtain the time dependence of the dipole moment, *quantum corrections* $D(\omega)$ have to be applied [80, 103]. These quantum corrections are responsible for correcting detailed balance and a popular choice is [80]

$$D(\omega) = \frac{\hbar\omega/k_B T}{1 - \mathrm{e}^{-\hbar\omega/k_B T}} \ . \tag{2.110}$$

Furthermore, in force-field MD simulations, $\mathbf{M}$ can be obtained from summing up atomic charges q_I:

$$\mathbf{M} = \sum_I \mathbf{R}_I q_I . \tag{2.111}$$

As a consequence, it is possible to calculate IR-spectra including effects of anharmonicity and finite absorption linewidths from force-field MD using eqs. (2.109) to (2.111).

2.4.3. Phonon quasiparticles from MD

For crystalline materials we would like to extend the harmonic phonon picture (section 2.3) with the information obtained from MD simulations. This can be done using the normal mode decomposition method [105–109]. Using this method, one can determine vibrational quasiparticles with a quasiparticle frequency $\tilde{\omega}_{\mathbf{q}\nu}$ and a quasiparticle lifetime $\tau_{\mathbf{q}\nu}$, from a calculation that includes all orders of the Taylor series in eq. (2.39). The starting point for this is the VACF. As has been discussed in section 2.4.2, the VDOS can be related to the power-spectrum $G(\omega)$ of the VACF [105]

$$G(\omega) = 2 \sum_j \int_{-\infty}^{\infty} d\tau \ \mathrm{e}^{i\omega\tau} \ \langle \mathbf{v}_j(0) \mathbf{v}_j(\tau) \rangle \ . \tag{2.112}$$

On the other hand, since the phonon eigenvectors $\hat{\mathbf{e}}_{\mathbf{q},\nu}$ are orthonormal, they can be used as a basis set to describe all atomic displacements and thus also velocities. We now introduce the velocities in reciprocal space, i.e., the atomic velocities $\mathbf{v}_j^{\mathbf{q}}$ projected on wavevector $\mathbf{q}$:

$$\mathbf{v}_j^{\mathbf{q}}(t) = \sqrt{\frac{m_j}{N}} \sum_l \mathrm{e}^{-iR_{jl}q} \ \mathbf{v}_{jl}(t) \ , \tag{2.113}$$

with power-spectrum

$$G_{\mathbf{q}}(\omega) = 2 \sum_j \int_{-\infty}^{\infty} d\tau \; \mathrm{e}^{i\omega\tau} \left\langle \mathbf{v}_j^{\mathbf{q}*}(0) \mathbf{v}_j^{\mathbf{q}}(\tau) \right\rangle \ . \tag{2.114}$$

And we further introduce the phonon-mode projected velocities

$$\mathbf{v}_{\mathbf{q},\nu}(t) = \sum_j \mathbf{v}_j^{\mathbf{q}}(t) \cdot \hat{\mathbf{e}}_{\mathbf{q},\nu}^j \ , \tag{2.115}$$

with power-spectrum

$$G_{\mathbf{q}\nu}(\omega) = 2 \int_{-\infty}^{\infty} d\tau \; \mathrm{e}^{i\omega\tau} \left\langle \mathbf{v}_{\mathbf{q},\nu}^*(0) \mathbf{v}_{\mathbf{q},\nu}(\tau) \right\rangle \ . \tag{2.116}$$

Since the phonon eigenvectors $\hat{\mathbf{e}}_{\mathbf{q},\nu}$ are orthonormal, as mentioned above, we can write

$$G(\omega) = \sum_{\mathbf{q}} G_{\mathbf{q}}(\omega) = \sum_{\mathbf{q},\nu} G_{\mathbf{q}\nu}(\omega) \ . \tag{2.117}$$

This allows us to interpret $G_{\mathbf{q}\nu}(\omega)$ as the contribution from phonon-mode ν to the phonon density of states at wavevector $\mathbf{q}$. On the other hand, it has been shown that for small temperature-dependent anharmonic phonon self-energies, with little frequency dependence, this contribution follows a Lorentzian lineshape [108]

$$G_{\mathbf{q}\nu}(\omega) \approx \frac{\left\langle |\mathbf{v}_{\mathbf{q},\nu}(t)|^2 \right\rangle}{\frac{1}{2}\gamma_{\mathbf{q}\nu}\pi \left(1 + \left(\frac{\omega - \tilde{\omega}_{\mathbf{q}\nu}}{\frac{1}{2}\gamma_{\mathbf{q}\nu}} \right)^2 \right)} \ . \tag{2.118}$$

This allows us to define "anharmonic phonon quasiparticles" with a quasiparticle frequency $\tilde{\omega}_{\mathbf{q}\nu}$ and a quasiparticle linewidth $\gamma_{\mathbf{q}\nu}$ related to the inverse phonon lifetime $\tau_{\mathbf{q}\nu}^{-1}$.

2.5. Disorder potential and Urbach energy

To investigate the impact of structural dynamics on optical absorption, correlations in the disorder potential can be examined [110–112]. The disorder potential is defined as [112]:

$$V(\mathbf{r}) = V_i(\mathbf{r}) - V_{\text{crystal}}(\mathbf{r}) \ , \tag{2.119}$$

with $V_i(\mathbf{r})$ being the instantaneous electrostatic potential and $V_{\text{crystal}}(\mathbf{r})$ the "perfect crystal potential". The spatial autocorrelation $C(\Delta\mathbf{r})$ of this disorder potential,

$$C(\Delta\mathbf{r}) = \frac{\langle V(\mathbf{r} + \Delta\mathbf{r}) \; V(\mathbf{r}) \rangle}{\langle V(\mathbf{0}) \; V(\mathbf{0}) \rangle} \ , \tag{2.120}$$

has been shown to provide information about optical absorption of a material [110–112]. Small correlations lengths of the correlation in eq. (2.120), on the order of interatomic distances, imply small Urbach energies E_U. The Urbach energy provides how steep the optical absorption coefficient α increases close to the onset of optical absorption [111, 113, 114]. If a material exhibits deviations from the perfect crystalline structure, e.g., because of structural disorder, the absorption coefficient increases exponentially as a function of photon energy E:

$$\alpha(E) \propto \mathrm{e}^{(E-E_1(T))/E_U(T)} , \tag{2.121}$$

with E_1 an energy close to the band gap in semiconductors. Small Urbach energies thus provide a steeper increase of the optical absorption. This implies that a higher fraction of incoming photons will already be absorbed in a thin layer of the semiconductor. Thus having small Urbach energies is one important factor for the fabrication of efficient thin film photovoltaic devices.

With the sketch in fig. 2.7 we want to explain the relation between disorder correlation length and Urbach energy in a more graphical and intuitive way. For a mathematical derivation we would like to refer to references [110–112]. Figure 2.7a sketches the case of long-range correlations, i.e., a displacement of a single atom (indicated by the arrow) can be seen by a large fraction of the material, as indicated by the yellow area. Since a large fraction of the material is influenced, many tail-states are induced in the electronic density of states $D(E)$ (yellow). Having many tail-states within the band gap implies that there are many electronic excitation possible by absorbing (lower energy) photons. But as their occupation is usually small, the absorption coefficient is also small and thus increases only slowly as a function of the photon energy. With this simple argumentation scheme, the Urbach energy is high in case of long range correlated disorder. Figure 2.7b, however, sketches the opposite case. Due to a short range correlation, atomic displacements (arrows) are only seen by small fractions of the material (green areas). As a consequence only a few tail states are induced in the density of states. And arguing in analogy to the long range scenario, we now find a small Urbach energy.

We will substantiate this picture in section 3.6 by explicitly linking correlations in the disorder potential to band edge distributions in HaPs. We will further find that the connection between (anharmonic) structural dynamics, disorder correlations, and band edge distributions is remarkable and particularly important in these materials.

2.6. Numerical details

The plane-wave code VASP [115] was used for DFT calculations and first-principles MD simulations. The projector augmented wave (PAW) method [116] was used as a pseudo-potential to treat core states. The PBE functional [49] was used to describe exchange and correlation. The plane-wave energy cutoff and the number of k-points used for each system, and listed below, were converged such that the change in total energy upon changing the parameter was less than 1-2 meV/atom.

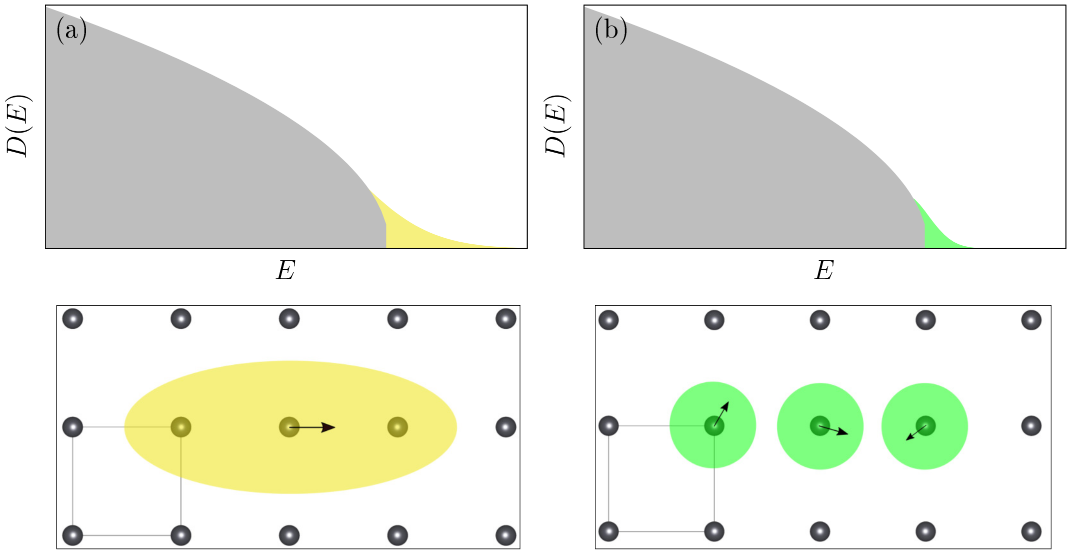

Figure 2.7.: Schematic representation of the amount of tail states in $D(E)$ (top) as expected from the extent of the correlation in the disorder potential (bottom, filled areas) caused by a nuclear displacement (black arrow) for the cases of **(a)** long-range and **(b)** short-range correlated disorder potentials. *Reprinted with permission from [2], published under a CC BY 4.0 license.*

Atomic structures were visualized using the VESTA program [117]. Furthermore, VESTA was also used to visualize the phonon modes adding arrows to the atomic structure.

2.6.1. Halide perovskites

Density functional theory calculations

In order to obtain accurate structural properties DFT calculations have been corrected for dispersive interactions in the Tkatchenko-Scheffler (TS) scheme [1, 61]. Unless stated differently, the following parameter were applied to simulate HaPs: a Γ-centered k-point grid of 6x6x6 and 6x4x6 k-points was used for cubic and orthorhombic structures, respectively. The energy threshold was set to 10^{-8} eV and the plane-wave cutoff energy to 500 eV for $CsPbBr_3$ and $CsPbI_3$ and to 600 eV for $MAPbBr_3$. The studied structures of all materials were optimized until forces on the atoms were below 1 meV/Å. The Gadget code [118] has been used as an alternative to the VASP internal routines for geometry optimization, in particular for the hybrid HaPs. In case Gadget and VASP provided somewhat different results, the structure with the lowest total energy has been used.

Lattice dynamics and Infra-red spectra

Phonon dispersions and VDOS were obtained using the phonopy package [66], implementing the finite displacement method described in section 2.3. Supercells, doubling the unit cell in each dimension, were used with the k-point grid being reduced accordingly. IR spectra were obtained using the phonopy-spectroscopy package [78, 119]. The Born effective charges were calculated using the density functional perturbation theory (DFPT) formalism as implemented in VASP [120, 121].

DFT-based molecular dynamics

First-principles MD simulations of cubic $CsPbBr_3$ and cubic $CsPbI_3$ were performed as implemented in VASP. A 4x4x2 (160 atoms) supercell was simulated in an NVT ensemble for 150 ps after an equilibration of at least 5 ps. The timestep for numerically integrating the equations of motion was set to 8 fs. To improve numerical efficiency, a plane-wave energy cutoff of 250 eV, an energy threshold of 10^{-6} eV , and a single k-point were used. Moreover, the “GW” PAW potentials were used, as they improved the numerical convergence of the electronic self-consistency cycles while retaining the accuracy of the power spectrum of the VACF (cf. fig. A1).

Force-field molecular dynamics

Force-field MD simulations were performed using the LAMMPS code [122] and the force fields for $MAPbI_3$ [86] and $MAPbBr_3$ [85], respectively, applying a timestep of 0.5 fs.

$MAPbBr_3$ Cubic and orthorhombic $MAPbBr_3$ were simulated in an NPT ensemble at 295 K and 130 K, respectively. All simulations started with a cubic 6x6x6 supercell (2592 atoms). For the low temperature simulation, the structure was optimized first resulting in a ratio $c/a \approx 1.067$ between the longest lattice parameter c and the shortest lattice parameter a. This has been proven to be a measure for the orthorhombic structure in this material [85]. A 150 ps NVT equilibration was followed by an 1 ns NPT equilibration at 0 pressure and a 4.5 ns production run. Frequencies obtained from the MD simulations, i.e., while calculating the IR spectra of $MAPbBr_3$ from MD, had to be reduced by 27% to account for a too stiff description of the dynamics [85, 123]. IR spectra from MD have been obtained according to eq. (2.109), employing the quantum correction of eq. (2.110). The total dipole moment of the system has been obtained as a sum of the atomic charges, eq. (2.111), as assigned to the atoms by the force field parametrization.

MAPbI$_3$ A 4x4x2 supercell of cubic MAPbI$_3$ (384 atoms) was simulated in an NVT ensemble for 150 ps, after equilibrating the system for 1 ns.

Phonon-quasiparticle properties

Phonon-quasiparticle properties of cubic CsPbBr$_3$ were calculated using a projection of the MD-based VACF onto harmonic eigenmodes as described in section 2.4.3. For this means, the dynaphopy package [105] has been employed, using standard FFT to transform to frequency domain. This provided quasiparticle frequencies and lifetimes at high symmetry points of the Brillouin zone. The finite-temperature phonon dispersion at arbitrary $\mathbf{q}$ was obtained from an interpolation akin to harmonic lattice dynamics calculations, i.e., an updated dynamical matrix was calculated from renormalized force-constants. Acoustic phonon modes at the Γ-point (zero-frequency modes) were excluded due to their long vibrational period in time domain.

Disorder potential and band-edge histogram calculations

The disorder potential and band-edge distributions were calculated for selected instantaneous configurations of the MD trajectories. A plane-wave energy cutoff of 500 eV and a 1x1x2 k-point grid, corresponding to the real space dimensions of the supercell, were used to increase the accuracy of the calculations. The autocorrelation function $C(\Delta y)$, as shown in figs. 3.20, 3.21, 3.23 and 3.29, was calculated for 30 structures, separated by 5 ps each, according to eq. (2.120). Specifically, the electrostatic potential energy averaged over all considered configurations was subtracted from the instantaneous potential energies to calculate the disorder potential. For fig. 3.29, Br displacements have further been projected on longitudinal and transversal directions, setting either of the contributions to zero. For the autocorrelation function in fig. 3.19 the deviation of an example configuration with one Pb ion displaced by 5 % of the primitive lattice constant was calculated with respect to the ideal configuration. A 5x5x2 supercell was considered in this case to account for the long-range nature of the response. The change in the charge density for longitudinal and transversal displacements of Br, as shown in fig. 3.30, was calculated similarly. Band-edge distributions were calculated from 90 instantaneous configurations, separated by 1.6 ps. In figs. 3.21, 3.23 and 3.35 histograms are shown as a function of dimensionless parameters. transversal and longitudinal

JDOS

The joint-density of states (JDOS) was calculated as a sum over all differences between the eigenstates $\epsilon_i(\mathbf{k})$ in the valence (v) and conduction bands (c) at all $\mathbf{k}$-points [124]:

$$\mathrm{JDOS}(E) = 2 \sum_{v,c,\mathbf{k}} \frac{w_{\mathbf{k}}}{\sigma\sqrt{2\pi}} \mathrm{e}^{-\frac{(\varepsilon_c(\mathbf{k})-\varepsilon_v(\mathbf{k})-E)^2}{2\sigma^2}} \tag{2.122}$$

Here, $\omega_{\mathbf{k}}$ are the weights of the k-points $\mathbf{k}$ and σ is the spectral broadening. In figs. 3.22 and 3.31, $\sigma = 20$ meV has been used. The finite temperature JDOS in fig. 3.22, as well as the JDOS in fig. 3.31, have been obtained for 90 snapshots of the MD simulation and geometries with projected Br displacements as described in section 2.6.1, respectively. In the latter case, structures which resulted in band gaps lower than 80% of the respective average band gap have not been considered. In order to numerically account for the sum over all k-points in the first Brillouin zone, non-selfconsistent calculations on an increased 3x3x6 k-point grid have been performed

Cs_4PbBr_6 and $CsPb_2Br_5$

Cs_4PbBr_6 was simulated using a Γ-centered 4x4x4 k-point grid, an energy threshold of 10^{-6} eV and a plane-wane cutoff energy of 350 eV. $CsPb_2Br_5$ was simulated using a Γ-centered 6x6x3 k-point grid, an energy threshold of 10^{-6} eV and a plane-wane cutoff energy of 450 eV. The structures of both compounds were optimized until the forces on the atoms were below 10^{-4} meV/Å. Again, Gadget [118] has been applied on top of VASP routines and the structure with the lowest total energy has been used for further calculations. Phonons were only calculated at the Γ-point, as implemented in VASP. IR spectra were calculated according to eq. (2.71) with the Born effective charges calculated using the DFPT formalism implemented in VASP.

PbTe

A conventional unit cell of PbTe (8 atoms) was used for PbTe. DFT calculations were performed with a 375 eV plane wave cutoff energy and a 6x6x6 k-point grid. An energy threshold of 10^{-6} eV for all calculations and a force threshold of 10^{-3} eV/Å for geometry optimization were applied. MD simulations were done for a 3x3x2 supercell (144 atoms), with a reduced cutoff of 240 eV, a Γ-only k-point grid and a timestep of 10 fs. PbTe was simulated in a canonical (NVT) ensemble at 425 K, with 5 ps of equilibration and 150 ps of production run. From this, the disorder potential and band-edge distributions were calculated for selected instantaneous configurations of the MD trajectories. A plane-wave energy cutoff of 375 eV and a 2x2x3 k-point grid, corresponding to the real space dimensions of the supercell, were used to increase the accuracy of the calculations. The autocorrelation function $C(\Delta y)$, as shown in fig. 3.35, was calculated for 30 structures, separated by 5 ps each, according to eq. (2.120). Specifically, the electrostatic potential energy averaged over all considered configurations was subtracted from the instantaneous potential energies to calculate the disorder potential. For the autocorrelation function in fig. 3.34 the deviation of an example configuration with one Pb ion displaced by 5 % of the primitive lattice constant was calculated with respect to the ideal configuration. Band-edge distributions were calculated from 90 instantaneous configurations, separated by 1.6 ps. Histograms in fig. 3.35 are shown as a function of dimensionless parameters.

The harmonic VDOS in fig. 3.33 was obtained performing lattice dynamics calculations using the finite displacement method as implemented in the phonopy package [125]. Therefore, a 2x2x2 supercell of the optimized structure was used. The k-point grid was reduced to a 3x3x3 Γ-centered grid according to the larger cell size, while all other numerical parameter were kept as described above. The VDOS from MD was obtained as a Fourier transform of the velocity autocorrelation function

$$\mathrm{vdos}(\omega) = \frac{N}{V} \int_{-\infty}^{\infty} dt\; e^{i\omega t}\, \frac{\langle \mathbf{v}(\tau + t) \cdot \mathbf{v}(\tau) \rangle}{\langle \mathbf{v}(\tau) \cdot \mathbf{v}(\tau) \rangle}\ , \tag{2.123}$$

see also eq. (2.105).

Si MD

The instantaneous total energies shown in fig. 3.14 are obtained from a MD simulation of a 3x3x3 supercell (216 atoms) of the conventional unit cell of Si. The DFT calculations were performed with a 240 eV plane wave cutoff energy and a Γ-only k-point grid, as well as an energy threshold of 10^{-6} eV. An NVT ensemble at 425 K was simulated with a timestep of 2 fs. The data shown in fig. 3.14 were following 2 ps of equilibration.

2.6.2. AgI

DFT-based molecular dynamics

First-principles MD simulations were performed with an energy threshold of 10^{-6} eV, a single k-point, a plane-wave energy cutoff of 280 eV, and a MD timestep of 10 fs. A system of 128 atoms in a cell of ~4736 Å^3 was simulated in an NVT ensemble at 500 K, with an equilibration time of 10 ps and 100 ps production run.

Selective dynamics as implemented in the VASP package were used to fix I or Ag atoms to perform gedankenexperiments. The systems were again equilibrated for 10 ps at 500 K, with the thermostat considering only the available degrees of freedom to obtain the temperature values. 10 instantaneous I configurations of the “full MD” trajectory, separated by 1 ps, were chosen to start simulations with I atoms fixed at “snapshots from full motion”.

Correlation functions

The MSD, eq. (2.102), was calculated as an ensemble average. The diffusion constant D was obtained from a linear fit of the MSD, according to eq. (2.103), with $n = 3$, i.e., $\mathrm{msd}(t) = 6Dt$.

The frequency dependent VDOS, eq. (2.105), was calculated as the FFT of the normalized VACF:

$$\mathrm{vdos}(\omega) = \frac{N}{V}\, FFT \left[\frac{\mathrm{vacf}(t)}{\mathrm{vacf}(0)} \right] \ , \tag{2.124}$$

with N the number of atoms and V the simulation volume. The VACF was calculated according to eq. (2.104) by averaging over atoms and initial time. Finally, the diffusion constant has been obtained from the zero-frequency value of the Fourier transformed VACF, see eq. (2.108).

Angles and Fourier filtering

Angles of a representative AgI_4 tetrahedron were calculated as

$$\Theta_i = \arccos \left(\frac{\mathbf{d}_{ij} \cdot \mathbf{d}_{ik}}{|\mathbf{d}_{ij}||\mathbf{d}_{ik}|} \right) \ , \tag{2.125}$$

where i,j,k are the I atoms of the tetrahedron defining the angle located at atom i. The atomic distances $\mathbf{d}_{ij}(t) = \mathbf{R}_i(t) - \mathbf{R}_j(t)$ were calculated from the atomic trajectories $\mathbf{R}_i(t)$.

The trajectories were further filtered to exclude high-frequency motions using a Fourier filter

$$R_{\mathrm{filtered}}(t) = \mathcal{F}^{-1} \left[\Theta(\omega)\Theta(\omega_{\max} - \omega)\mathcal{F}[R(t)] \right] \ . \tag{2.126}$$

Here, $\mathcal{F}$ and $\mathcal{F}^{-1}$ are the Fourier transform and its inverse, respectively. The upper limit in the Heaviside step function Θ was set to $\omega_{\max} = 4\ \mathrm{cm}^{-1}$.

3. Results and discussion: halide perovskites

3.1. Introduction to halide perovskites

Halide perovskites (HaPs) are a material class with remarkable properties. The materials are named after their crystal structure which resembles that of $CaTiO_3$, a mineral named after LEV PEROVSKI. This typical cubic perovskite structure can be seen in fig. 3.1. It consists of corner sharing BX_6 octahedra, centered around a B-site cation, with the A-site cations positioned at sites in between the octahedra. The stoichiometric composition of perovskite materials is ABX_3. Whether the cubic perovskite structure actually exists for a given set of chemical elements {A,B,X} is determined by the empirical Goldschmidt tolerance factor [126]

$$t = \frac{R_A + R_X}{\sqrt{2}(R_B + R_X)} \,, \tag{3.1}$$

with R_i the atomic radius of element i. In order to find a cubic perovskite structure $t \approx 1$ is required. For $t < 0.8$ and $t > 1$ different crystal structures are found for ABX_3 compounds, as can be seen for the example of $CaCO_3$ for which $t > 1$ and that is found with calcite structure and aragonite structure [126]. In case of *lead halide perovskites*, B is lead (Pb), and X is a halide ion, e.g., Br, I, or Cl. Finally, the A-site is either a large atomic cation such as Cs, or it is a small (organic) molecular cation such as MA or formamidinium (FA).

Electronically, HaPs resemble usual semi-conductors. BRENNER ET AL. (2016) remark that *"the most extraordinary feature of the bandstructure of $MAPbI_3$ is how ordinary it is"* [16]. An example band structure is shown in fig. 3.2. HaPs are semi-conductors with a direct band gap in the optical range and they have effective masses comparable to those of, e.g., GaAs [16]. However, the band gap of cubic HaPs is found at the edge of the Brillouin zone, at the R-point, not at the Brillouin zone center. The nature of the band edges is of PbX origin, i.e., the A-site cation is not contributing to electronic states close to the band gap. In contrast, the electronic states of the A-site cations are found to be far away from the Fermi energy fueling the discussion whether the A-site cation is only a "space filler" stabilizing the structure [57]. Due to the heavy masses of the atoms contributing to the band edges, spin-orbit coupling (SOC) has a strong influence. In addition, HaPs show only a few sub-bandgap states, resulting in small Urbach energies of only about 15 meV at room temperature [127–131], and efficient solar absorption. The combination

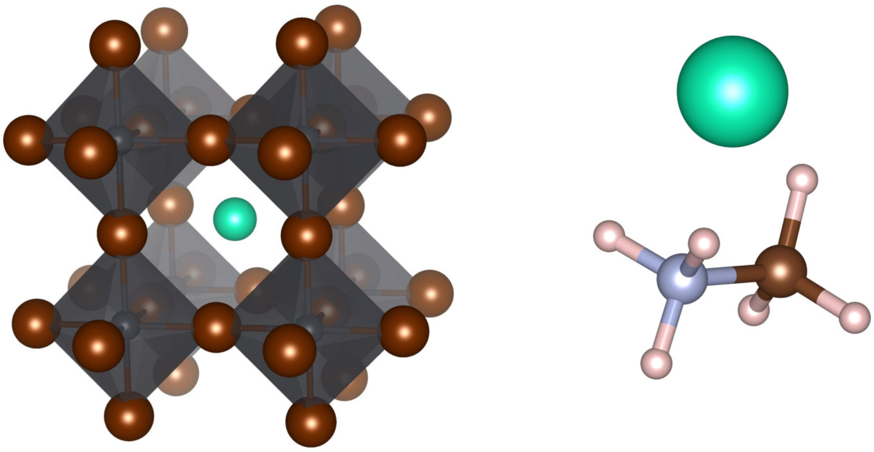

Figure 3.1.: Schematic representation of the crystal structure of cubic $CsPbBr_3$, shown as an example for HaPs. The structure consists of corner sharing BX_6 octahedra (gray), with six X-site anions (here: Br, brown) centered around a B-site cation (here: Pb, gray), and A-site cations (here: Cs, cyan) positioned at sites in between the octahedra. On the right two paradigmatic A-site cations are shown. Top: Cs in cyan. Bottom: Methylammonium (MA) molecule (CH_3NH_3), consisting of C (brown), N (blue), and H (white).

of these features in conjunction with long carrier lifetimes, and thus long diffusion lengths renders HaPs promising materials for photo-voltaic applications [8–18]. Up to now, solar cells with an efficiency of more than 25% have been reported [132] (cf. also reference [7]). This is comparable with Si and GaAs solar cells, where reaching the same efficiency took decades of research (cf. reference [7]). Further applications for HaPs include the usage as photon sources, e.g., for LEDs and lasers [19, 20], and sensor applications [20].

Importantly many findings suggest that charge transport in HaPs is significantly influenced by lattice dynamical phenomena, such as polaronic effects and dynamic disorder [16, 134, 135]. The strong electron-phonon interactions in these materials might be further enhanced by the high phonon occupation numbers at usual device operation temperatures. The high phonon occupation numbers are a consequence of the mechanical softness of HaPs, which is related to their low phonon frequencies [24, 136–139].

Moreover, lattice dynamics in HaPs show effects going beyond the usual harmonic approximation used in solid state physics [2, 21–27, 138, 140–142]. These anharmonic effects can, e.g., be seen in the short phonon lifetimes [2, 22, 26, 27], low thermal conductivity [23], and presence of a central peak in the Raman spectrum [24]. In addition, this includes structural phase transitions related to phonon mode condensation [143], with the phonon modes that are associated with the phase transitions showing up as imaginary modes in harmonic phonon calculations [2, 26, 144–150]. Temperature driven phase transition occur in all HaPs discussed below, due to octahedral tilting [143, 146, 151–154]. I.e., starting from the cubic perovskite

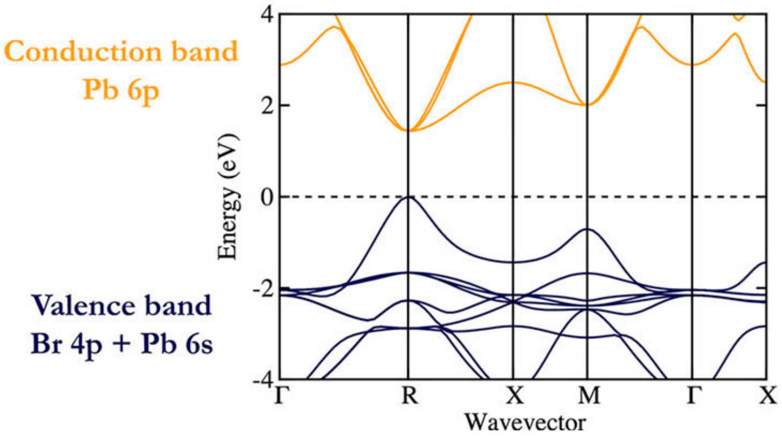

Figure 3.2.: Electronic bandstructure of cubic $CsPbBr_3$ calculated using DFT without SOC. *Reprinted from [133], with the permission of AIP Publishing.*

structure (fig. 3.1) and decreasing temperature, the system will transition from the cubic structure to a tetragonal structure and finally to an orthorhombic structure (fig. 3.3).

The organic cations of hybrid organic-inorganic HaPs add further complexity to the system. These cations are only weakly bound to the PbX octahedra, e.g., by H-bonds and thus molecular rotation is activated at higher temperatures [21, 23, 155]. In this picture, the organic molecule introduces (rotational) disorder and is discussed to have certain impacts on HaPs properties [21, 23, 155]. First of all, the entropic contributions of the disordered molecules have been discussed to stabilize the material [156]. And second, molecular rotation has been discussed to interact with charge carriers in form of screening [155], dynamical changes of the band structure [57] and localization of charge carriers due to dipole reorientation [157]. Moreover, the rotational motion of the organic cation is per se anharmonic and thus not fully included in the phonon picture of structural dynamics. Further, the motion of the organic A-site cations is found to be strongly coupled to the structural dynamics of the PbX octahedra, and thus mediating properties like the band gap and structural dynamics properties (e.g., vibrational lifetimes) of the inorganic framework at least indirectly [22, 57, 156, 158].

On the other hand, little differences have been observed between hybrid organic-inorganic HaPs and all-inorganic (Cs-based) HaPs with respect to vibrational properties [24], polaron binding energies, delocalization lengths, formation times, or bimolecular recombination lifetimes [161]. This might be explained by the notion that longitudinal-optical (LO) modes associated with Pb-X stretching and bending are important for electron-phonon coupling and thus properties like charge carrier scattering and mobility [134, 162, 163].

As a paradigmatic example for the wide class of HaPs, mainly $CsPbBr_3$ will be studied. This choice will be put in contrast with HaPs of different composition several times, when appropriate. Starting from the harmonic approximation in the low temperature orthorhombic phase, we will discuss the theoretical and experimental

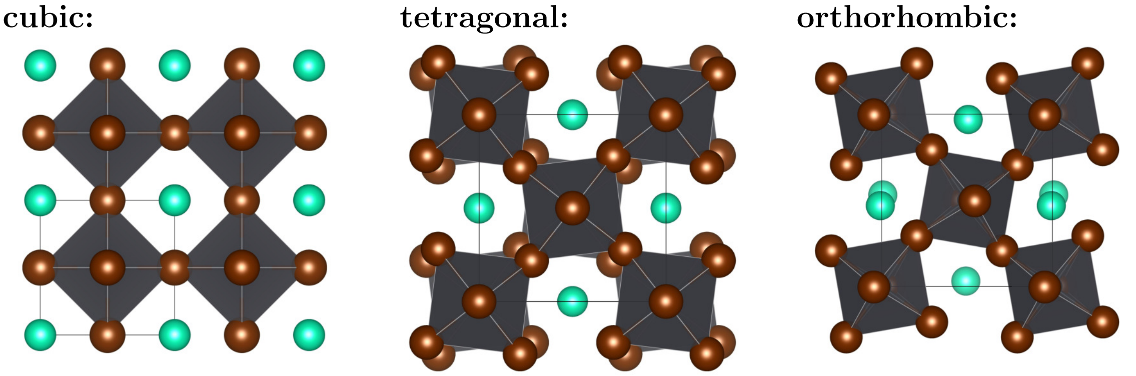

Figure 3.3.: Schematic representation of the structural phases of $CsPbBr_3$ (structures taken from references [151, 159, 160]). Starting from a cubic structure, the material transitions to a tetragonal and orthorhombic structure upon cooling. The color scheme is the same as in fig. 3.1.

IR spectra of $CsPbBr_3$ and $MAPbBr_3$ in section 3.2. This includes a discussion about the influence of the A-site cation and a brief investigation of Pb- and Cs-rich structural phases, which might form during experimental sample preparation. In section 3.3, it will be demonstrated that the high-temperature cubic perovskite structure is located at a local maximum of the potential energy surface. Afterwards, in sections 3.4 to 3.7, anharmonic calculations of cubic $CsPbBr_3$ based on first-principles MD simulations will be analyzed. This will also include a discussion how dynamic disorder is introduced to the system and how the correlation length of the induced disorder potential helps to understand important device properties such as the Urbach energy. In section 3.7, the MD data will be used to study the halide motion in detail. Finally, in section 3.8, HaPs will be contrasted to anharmonic PbTe.

3.2. Influence of the A-site cation on the infra-red spectrum in the orthorhombic phase

The conventional starting point for theoretical studies of lattice dynamics are calculations using the harmonic approximation. The harmonic phonon dispersion and vibrational density of states (VDOS) of the prototypical $CsPbBr_3$ in the low temperature orthorhombic phase is shown in fig. 3.4 . The choice for the orthorhombic phase is supported by the phase diagram of $CsPbBr_3$, for which the phase transition occurs only at approximately 130°C [151]. Thus, the orthorhombic phase is the one which is relevant around room temperature. As we expect for this mechanically soft material [24, 136–139], we observe low phonon energies of less than 6 THz (200 cm^{-1}). These low phonon frequencies are also observed in experimental measurements, e.g., by means of neutron scattering [164], Raman spectroscopy [24], and infrared spectroscopy (see results presented below). For comparison, the optical phonon frequencies of typical inorganic semi-conductors are in the range of

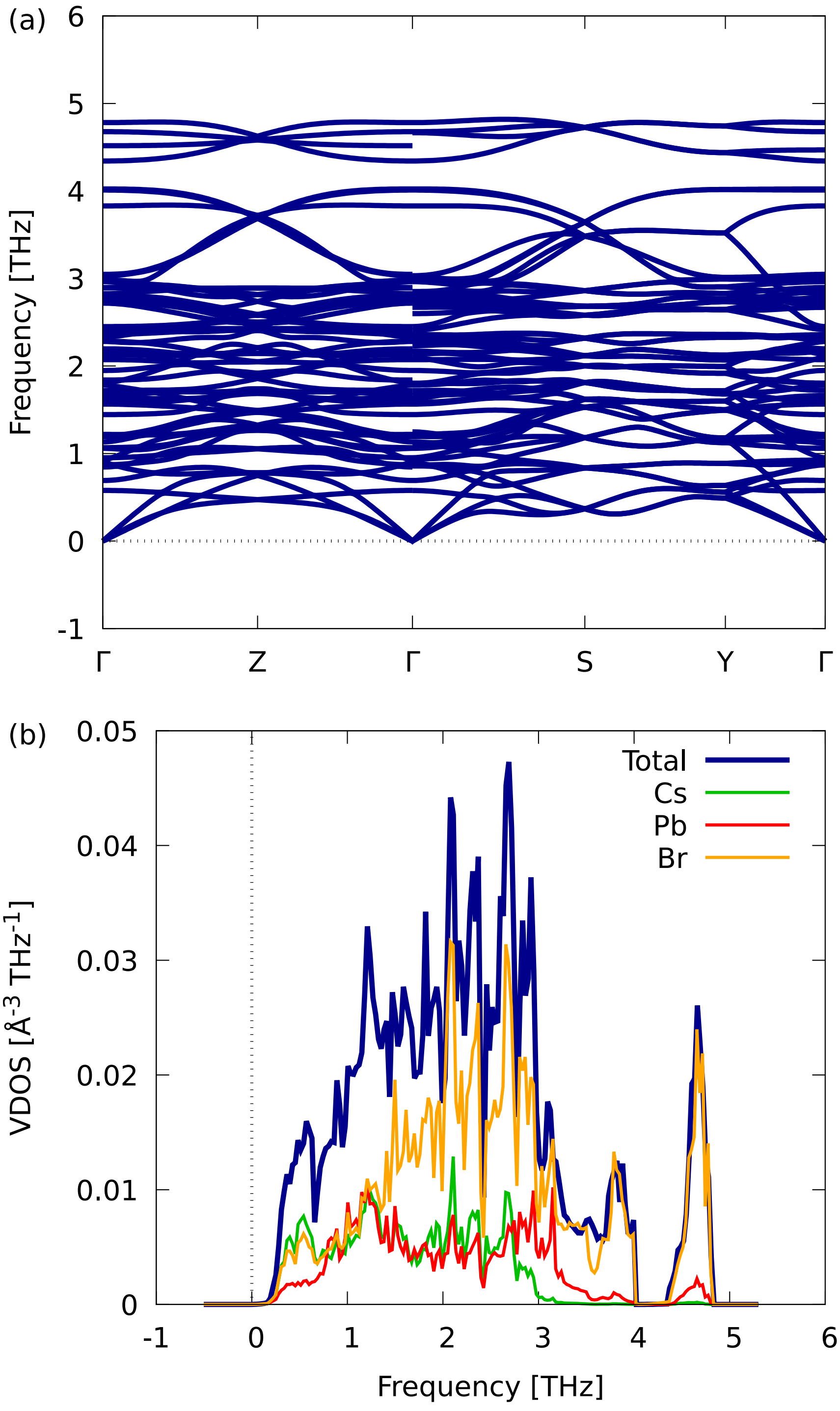

Figure 3.4.: **(a)** Phonon dispersion relation and **(b)** VDOS of orthorhombic $CsPbBr_3$ as obtained from harmonic phonon calculations. The phonon density of states is further projected onto the contributions from Cs, Pb, and Br, respectively.

about 9 THz for GaAs and up to 16 THz for silicon (see, e.g., ref. [4] and references therein). The low phonon frequencies found for $CsPbBr_3$ imply that the phonon occupation numbers are high even at moderate temperatures, suggesting a large influence of structural dynamics on the physical properties of HaPs, as discussed in the introduction, section 3.1.

From calculations of the harmonic phonon frequencies and eigenvectors at the Γ-point, combined with Born effective charges, a theoretical IR spectrum can be obtained (cf. section 2.3.4). It allows to probe optical phonons at the Γ-point and, since an interaction between lattice dynamics and light is required, it allows to determine the (frequency dependent) dielectric constant. The latter, combined with LO phonon frequencies and charge carrier effective masses, allows to determine polaron parameters, such as the polaron mass [165]. Finally, the IR spectrum is a material property that is directly accessible both to theory and experiment.

Motivated by the ongoing debate how important the A-site cation in HaPs actually is for functional properties, we are especially interested in a comparison of the IR spectra of $CsPbBr_3$ and $MAPbBr_3$. On one hand, the electronic structure close to the Fermi energy is dominated purely by the PbBr framework, on the other hand lattice dynamics are found to be important in these materials (see section 3.1 and references there). Pb and Br motion is expected to largely dominate the low frequency region due to their higher masses. At the same time, a correlation of the A-site cation motion and the PbBr framework is discussed in literature [6, 22, 57, 156, 158]. Cs with an atomic mass of approximately 132 u is much heavier than the MA cation (approximately 32 u) and the frequency, at least of an harmonic oscillator, is proportional to $1/\sqrt{m}$. Therefore, Cs is expected to have a higher contribution to the low frequency spectrum than the organic cation composed of light elements, such as H, and exhibiting strong atomic bonds. Consequently, the question how much lattice dynamics in the low frequency spectral region are influenced by the A-site cation can be considered to be non-trivial. Of course, $MAPbBr_3$ also has high-frequency vibrations outside the frequency range considered here, due to intramolecular vibrations of the organic molecule. These high-frequency vibrations will not be discussed here, as the focus is set on vibrational properties occurring at frequencies that are comparable to those of the inorganic PbBr framework of the perovskite crystal, and less on the internal vibrational properties of the organic molecules.

In fig. 3.5 the theoretically calculated IR spectra of $CsPbBr_3$ and $MAPbBr_3$ are shown. The calculated IR activities are shown as vertical bars, comparing the two materials, and broadened by a Lorentzian function. The broadening has been applied to facilitate the visual comparison with experimentally measured spectra. Unlike the experimentally measured broadening, which is related to vibrational lifetimes and instrument properties, the broadening applied in fig. 3.5 is arbitrary and does not convey any physical information. The comparison between $CsPbBr_3$ and $MAPbBr_3$ reveals that both materials show actually quite similar spectra in the region below 4 THz, although the partial VDOS in fig. 3.4 shows obvious contributions of Cs in this frequency range. A significant difference between the different materials can

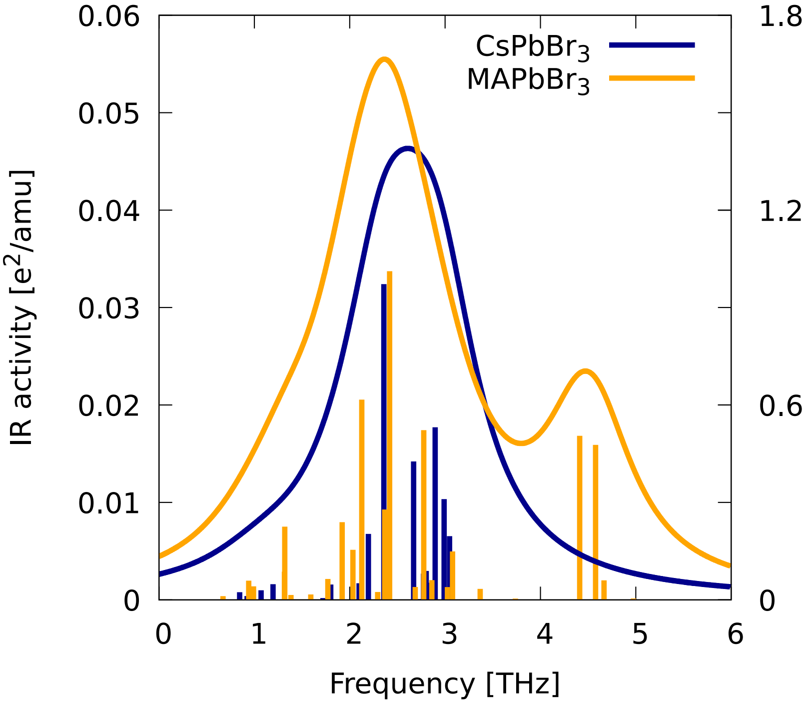

Figure 3.5.: Infrared activity of CsPbBr$_3$ and MAPbBr$_3$ in the orthorhombic phase as obtained from DFT calculations. The IR activity (vertical bars, right y-axis) has further been broadened by a Lorentzian (left y-axis) with width=1 THz as a guide to the eye. The units are the same on both axes.

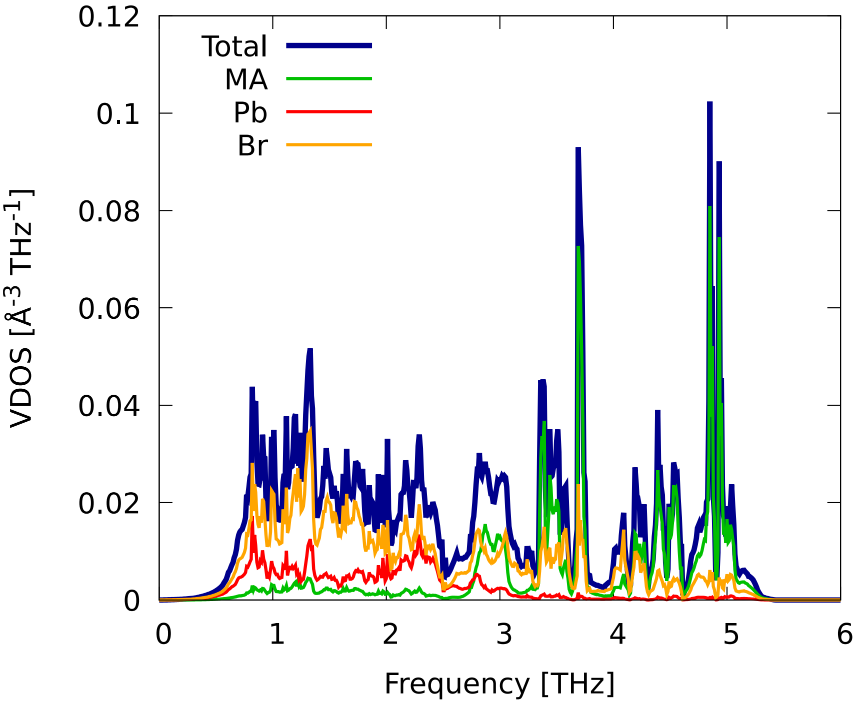

Figure 3.6.: VDOS of orthorhombic $MAPbBr_3$ as obtained from harmonic phonon calculations. The phonon density of states is further projected onto the contributions from Br, Pb, and the MA molecule, respectively.

only be seen in the frequency range above 4.5 THz. To investigate this difference the VDOS projected on the A-site, B-site, and X-site species, respectively, can be used. The projected VDOS of $CsPbBr_3$ has already been shown in fig. 3.4, that of $MAPbBr_3$ is shown in fig. 3.6. Although there are phonon modes related to mainly Br motion above 4.5 THz (cf. figs. 3.4 and 3.6), there also is a large contribution of the MA molecule, see partial VDOS in fig. 3.6. In particular, a visualization of the IR active modes, shown in fig. 3.7, exposes a dominant contribution of the MA molecule. Similarly, a detailed analysis of the MA vibrational eigenvectors in $MAPbI_3$ reveal those modes to be MA libration [166]. In conclusion, the theoretical IR spectra suggest that the main difference between the inorganic $CsPbBr_3$ and the hybrid $MAPbBr_3$ in the investigated frequency range is an additional feature in the IR spectrum of the latter material.

The deduction drawn from the theoretical spectra can further be tested by a comparison to experimentally measured IR spectra of both materials [165, 167]. However, first theoretical IR calculations will be used to examine whether the experimentally measured samples of $CsPbBr_3$ are indeed perovskite crystals. Besides the perovskite $CsPbBr_3$ discussed here, the Cs-rich compound Cs_4PbBr_6 and the Pb-rich compound $CsPb_2Br_5$ (fig. 3.8) can form from the same precursors [168–170]. Moreover, by reacting with CsBr or $PbBr_2$, $CsPbBr_3$ can spontaneously be converted to Cs_4PbBr_6 and $CsPb_2Br_5$ without applying high temperature, high pressure, or catalysts [168, 170]. In addition, water is found to extract CsBr driving a conversion of Cs_4PbBr_6 to $CsPbBr_3$ and $CsPbBr_3$ to $CsPb_2Br_5$ [168]. As a consequence, being able to predict

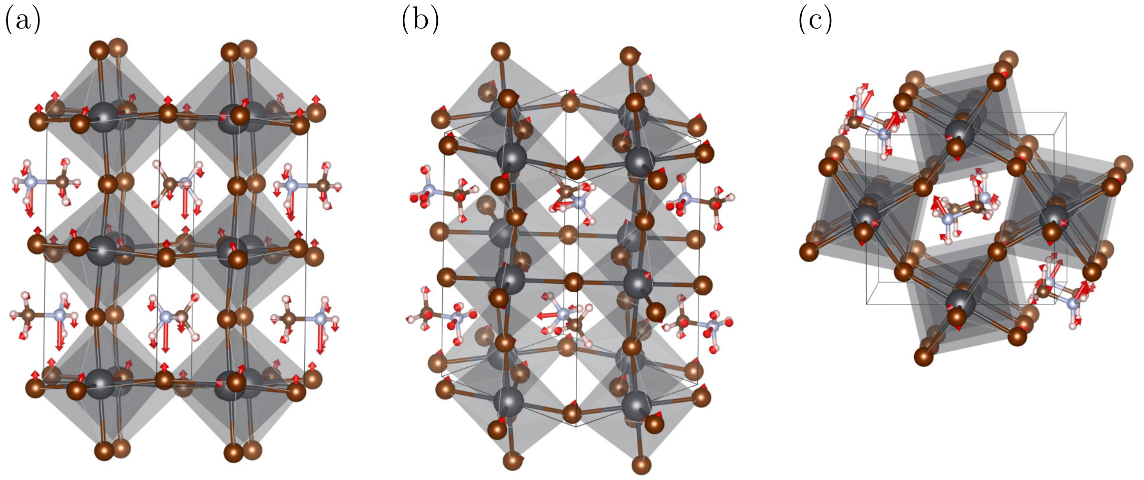

Figure 3.7.: Visualization of the IR active modes close to 4.5 THz / 150 cm^{-1}. **(a)** Phonon mode at 4.41 THz / 147.15 cm^{-1}. **(b)** Phonon mode at 4.58 THz / 152.70 cm^{-1}. **(c)** Same phonon mode as in panel (b) shown from a different perspective.

the IR spectra of Cs_4PbBr_6 and $CsPb_2Br_5$ and comparing them to the spectra measured for the experimental perovskite sample might allow to learn about the actual composition and eventually to draw conclusions on the stability of $CsPbBr_3$.

Figure 3.9 shows the IR spectra of these compounds. Similar to the perovskite spectrum in fig. 3.5, the IR activities of Cs_4PbBr_6 (blue) and $CsPb_2Br_5$ (orange) are shown as vertical bars and broadened by a Lorentzian function. The broadening again is chosen arbitrary for better comparison with the theoretical and experimental spectra of $CsPbBr_3$. From this comparison with the spectra of $CsPbBr_3$ it can be seen that the theoretical spectra of all three $Cs_aPb_bBr_c$ compounds can clearly be distinguished from each other. The Cs-rich compound Cs_4PbBr_6 has only a small frequency range at around 3.15 THz. This is at the higher end of the calculated IR spectrum on $CsPbBr_3$. In addition it is higher than main features in the calculated spectrum of $CsPb_2Br_5$, but lower than the highest frequency features of the latter compound. The Pb-rich compound $CsPb_2Br_5$ on the other hand has its main IR active vibrations in a range between $\sim$ 0.9 THz and $\sim$ 2.55 THz. This is at the lower end of theoretical $CsPbBr_3$ frequencies and clearly lower than Cs_4PbBr_6 frequencies. Besides this, $CsPb_2Br_5$ has also contributions to the IR spectrum at about 4 THz. This is clearly higher than any IR active vibrations of both the perovskite $CsPbBr_3$ and Cs_4PbBr_6.

With this short excursion we have discussed the possible presence of Cs-rich Cs_4PbBr_6 and Pb-rich $CsPb_2Br_5$ compounds within a sample. By discussing and comparing the IR spectra of these compounds with that of $CsPbBr_3$ we have shown that we can distinguish between the spectra of all three compounds.

Herewith, the theoretical spectra can be compared to the experimental spectra in fig. 3.10. There, the relative transmittance of $CsPbBr_3$ and $MAPbBr_3$ samples are shown at room temperature (fig. 3.10a) as well as a comparison of room tempera-

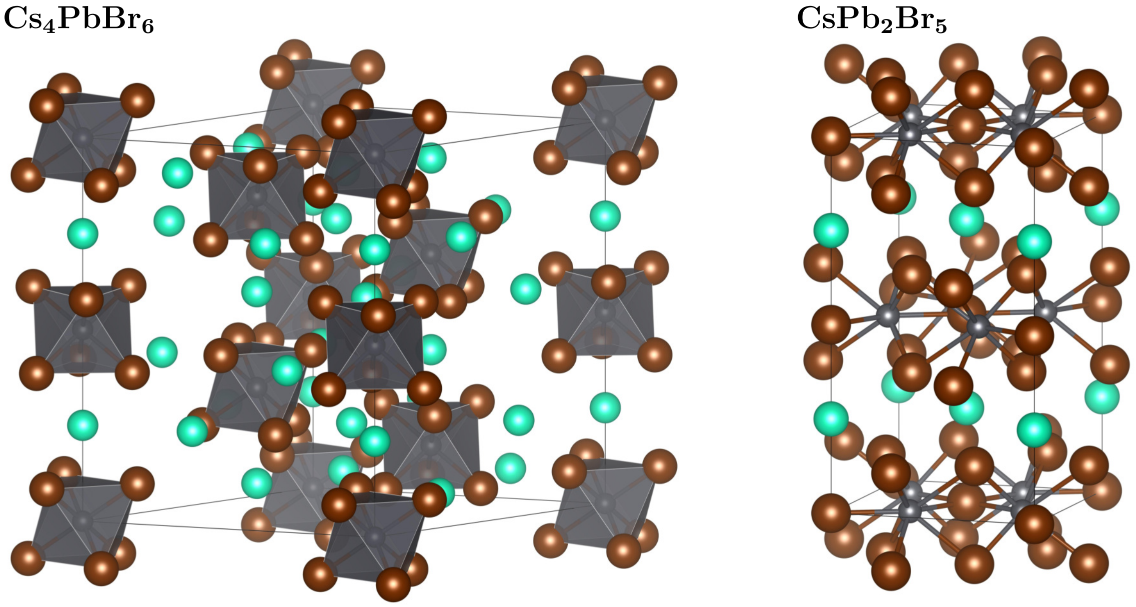

Figure 3.8.: Structural representations of Cs_4PbBr_6 and $CsPb_2Br_5$. The color scheme is the same as in fig. 3.1.

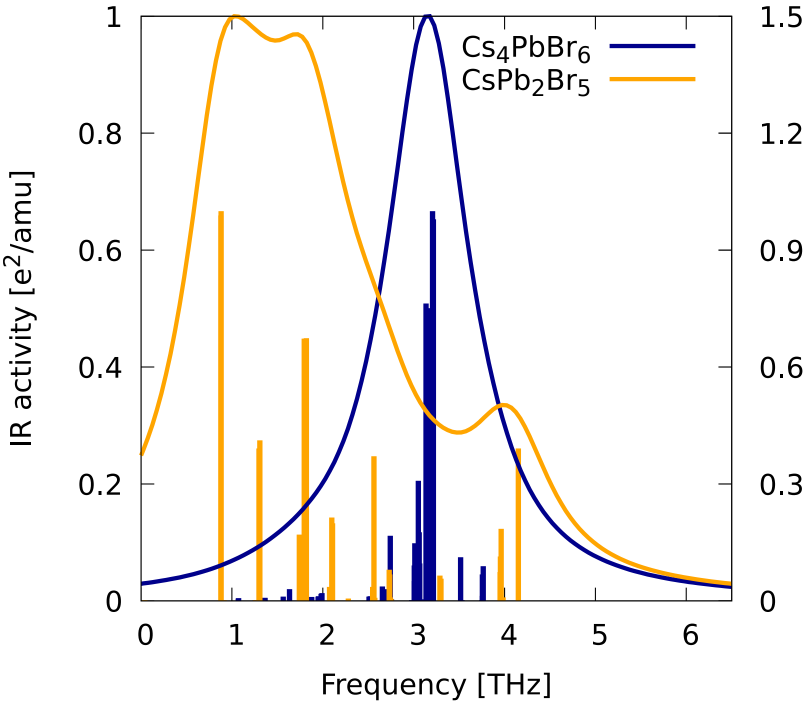

Figure 3.9.: Infrared activity of Cs_4PbBr_6 and $CsPb_2Br_5$ obtained from DFT calculations. The IR activity (vertical bars, right y-axis) has further been broadened by a Lorentzian (left y-axis) with width 0.5 THz as a guide to the eye. The units are the same for both axes.

ture (cubic phase) and low temperature (orthorhombic phase) spectra in the case of $MAPbBr_3$ (fig. 3.10b). The IR activity shown in fig. 3.5 can in first approximation be compared to *1 - relative transmittance*, as the latter approximately provides the absorption. The absorption is highest for frequencies with a high IR activity. In fig. 3.10a, it can be seen that the absolute absorption of $CsPbBr_3$ is much smaller than that of $MAPbBr_3$. However, when both spectra are normalized (inset of fig. 3.10a), they are remarkably similar, like it was found theoretically for most parts of the spectrum in fig. 3.5. There are slight differences, like the higher frequency tail of $MAPbBr_3$ decaying slower, which can potentially be understood, by the possible configurational disorder in $MAPbBr_3$ due to the organic molecule. This is supported by the observation, that the decay is much faster in the low temperature, orthorhombic spectrum, shown in fig. 3.10b. As another difference, for lower frequencies, the peak at approximately 1.35 THz is much more pronounced in $MAPbBr_3$. This peak seems to also exist in $CsPbBr_3$ but is hardly visible within the slope of the main peak. However, for low frequencies, close to 1 THz, limitations of the measurements due to the experimental setup are expected. Thus, overall, and especially around the main peak, we find the two spectra to remarkably well resemble each other. Furthermore, from a comparison with theoretical spectra in figs. 3.5 and 3.9, first of all strong evidence is presented that the experimentally measured $CsPbBr_3$ sample was indeed a perovskite crystal as Cs_4PbBr_6 frequencies are predicted to be higher than any experimentally measured feature whereas $CsPb_2Br_5$ spectra are predicted to have one main feature at the lower end of the experimentally measured spectrum and a second feature that is predicted to occur at frequencies higher than any experimentally measured feature and that is not seen in experiment. What is more, besides a shift of slightly less than 1 THz good overall agreement between theory and experiment can be found for most parts of the spectra. The shift can likely be attributed to numerical parameters such as SOC or XC-functional [171, 172]. However, the most striking difference between theory and experiment is that the IR active modes at around 4.5 THz/150 cm^{-1} in the theoretical spectrum of $MAPbBr_3$ are not only absent in the theoretical IR spectrum of $CsPbBr_3$, surprisingly, they are also absent in the experimental IR spectrum. In particular, in experiment there is no additional mode in $MAPbBr_3$ compared to $CsPbBr_3$, unlike it was predicted theoretically. This naturally rises questions about the origin of the computationally found additional IR active mode.

Experimental measurements of the LO phonons of $MAPbBr_3$ show a feature close to the frequencies of the additional theoretical features [165]. LO phonons are not infra-red active and thus cannot be seen in the transmission spectra, fig. 3.10 [39]. However, these LO phonons are always included in theoretical calculations of the phonon dispersion and VDOS. And in fact, both $MAPbBr_3$ (fig. 3.6) and $CsPbBr_3$ (fig. 3.4) show vibrational modes around 4.5 THz. The VDOS in the relevant frequency range can be attributed to Br motion in both materials, and there are large contributions of MA in $MAPbBr_3$. Experimentally, LO phonons can be measured with the method suggested by Berreman [173]. Instead of illuminating the sample perpendicularly and measuring its absorption, the angle of incidence (AoI) is changed to 60°. The transmittance measured with a non-normal angle of the incoming light also contains information about the LO phonons of the material [39,

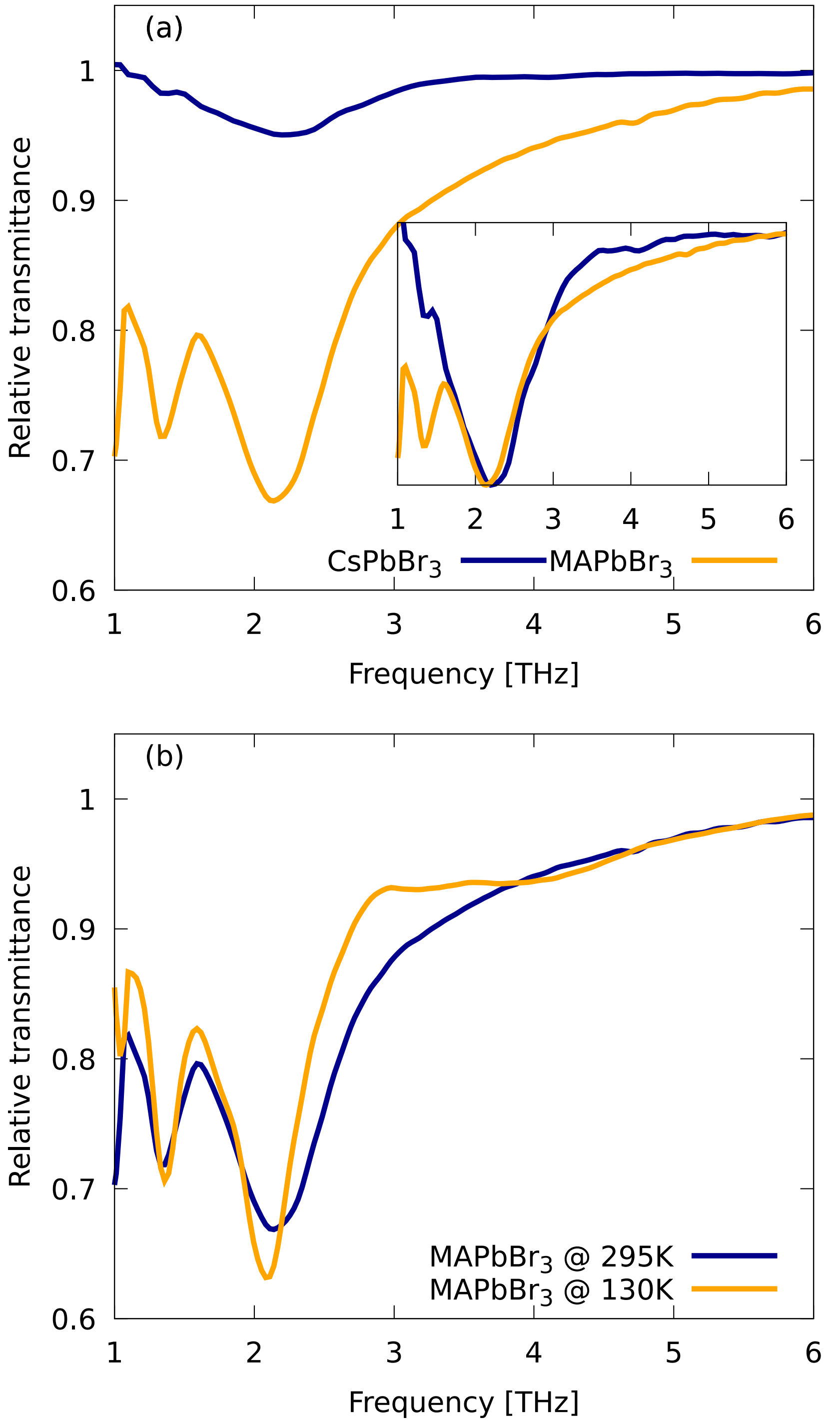

Figure 3.10.: IR spectra of CsPbBr$_3$ and MAPbBr$_3$ as measured from our experimental collaborators [165, 167]. **(a)** Room temperature (295 K) IR spectra of CsPbBr$_3$ and MAPbBr$_3$. Shown is the relative transmittance. The inset shows the transmittance scaled to the same range for CsPbBr$_3$ and MAPbBr$_3$, facilitating a comparison. **(b)** Room temperature (295 K, cubic) and low temperature (130 K, orthorhombic) IR spectra of MAPbBr$_3$. Shown is the relative transmittance.

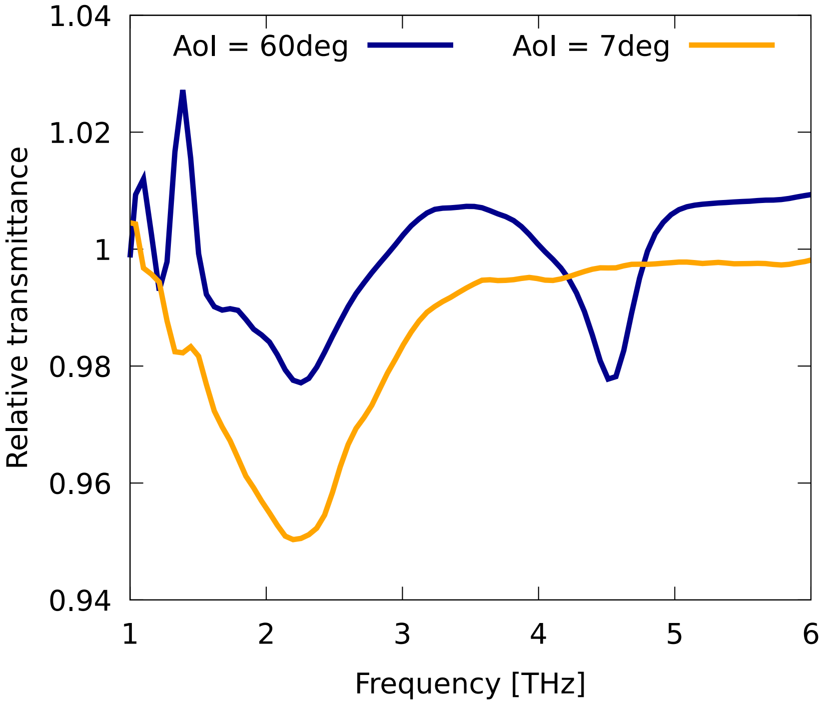

Figure 3.11.: Relative transmittance of $CsPbBr_3$ measured with normal (i.e., 7°) and 60° angle of incidence (AoI) of the incoming light as measured from our experimental collaborators [167].

165, 173]. For $CsPbBr_3$, the spectrum is shown in fig. 3.11 [167] which shows the relative transmittance of $CsPbBr_3$ measured with normal (i.e., 7°) and 60° AoI. The non-normal spectrum shows an additional peak at around 4.5 THz revealing the LO phonon frequency. This frequency is predicted very accurately from theory, as a comparison with fig. 3.4 reveals. Interestingly, the LO phonon frequency of $CsPbBr_3$ is close to the LO phonon frequency of $MAPbBr_3$ reported in literature [165] and the additional feature in our experimental IR spectrum. This suggests that the experimentally measured LO modes in $CsPbBr_3$ and $MAPbBr_3$, relevant for investigating charge transport [165], can be attributed to Br motion and are not related to the additional modes in the theoretical IR spectrum of $MAPbBr_3$ compared to $CsPbBr_3$. As discussed above, the latter modes can be attributed to MA libration, a type of motion that is understood not to be described accurately within the harmonic approximation.

To investigate whether the theoretically found additional IR active mode is a consequence of anharmonic MA motion, the IR spectrum of $MAPbBr_3$ has also been calculated from (force-field) MD simulations using fixed atomic charges and dipole autocorrelation functions, see section 2.4.2. The IR spectra calculated at low temperature (130 K) and at room temperature (295 K) are shown in fig. 3.12. As can be seen in fig. 3.12, calculations based on MD simulations show much better agreement with the higher frequency tail of the main peak, correctly predicting the absence of any additional peak at higher frequencies. In addition, even the shape of the tail, showing a shoulder in the low temperature spectrum, is predicted correctly. On the

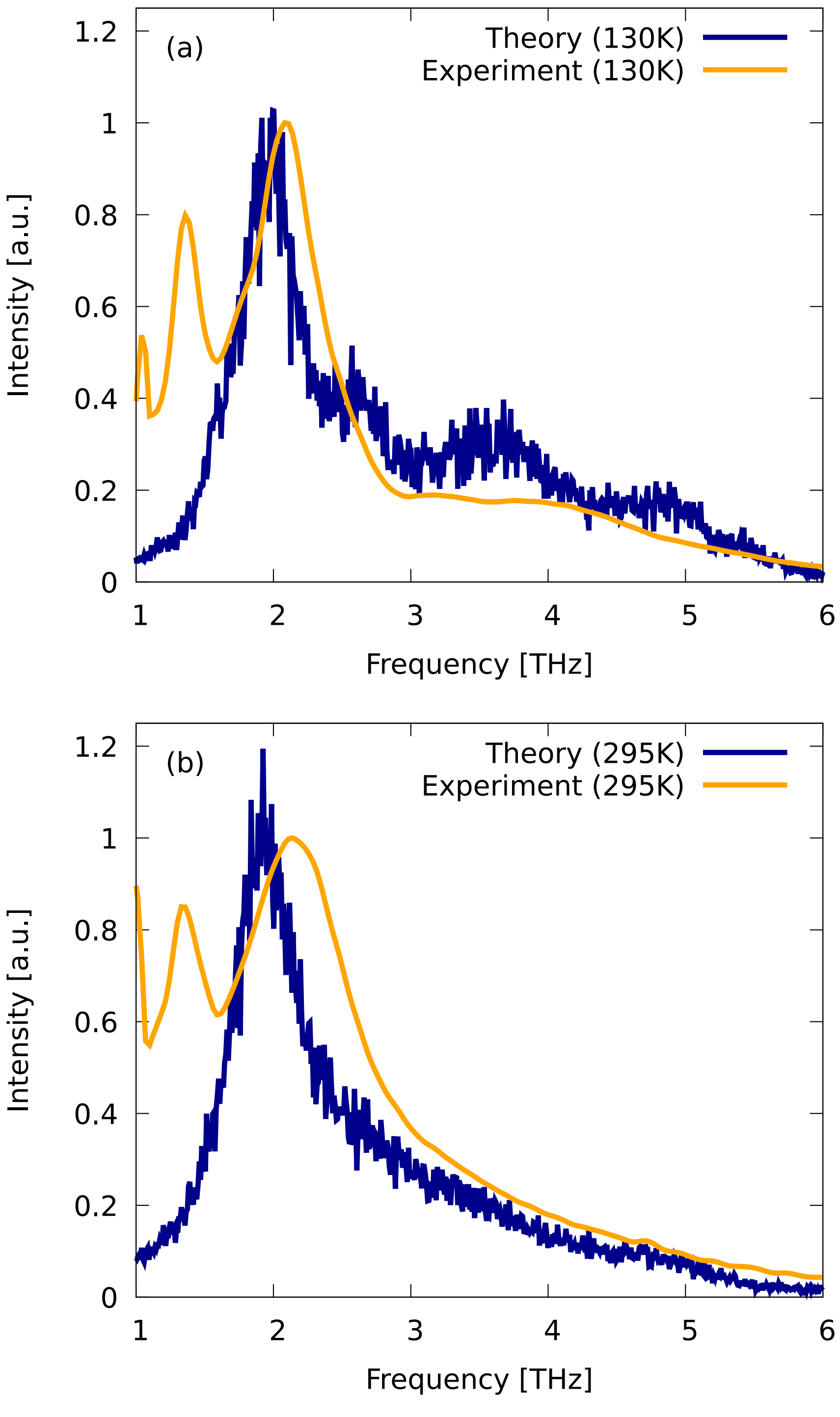

Figure 3.12.: IR intensity of $MAPbBr_3$ calculated from (force-field) MD simulations using fixed atomic charges and the dipole autocorrelation function. The experimental line shown for comparison is 1 − *relative transmittance* (cf. fig. 3.10), normalized for the highest peak.

other hand, the peak at approximately 1.35 THz is not predicted correctly from the MD simulations, demonstrating potential shortcomings of the force-field, which is, for instance, known to provide too high frequencies if not scaled *a posteriori* (see details in section 2.6.1) [85]. The absence of the IR active mode at approximately 4.5 THz in MD simulations can be rationalized recalling our findings on the nature of the underlying nuclear motion. According to the visualization in fig. 3.7, it is most likely related to MA libration. This is especially interesting as IR activity of a vibrational mode is related to the change of the dipole moment (see section 2.3.4) and the organic MA molecule exhibits a dipole moment. In conventional theoretical calculations only one unit cell of the material is used explicitly and repeated by periodic boundary conditions to resemble a bulk material. However, this also implies that only a single configuration of MA orientation is repeated periodically, implying a situation of parallel orientated dipole moments. Accordingly, the additional mode found theoretically might either be a consequence of the limitations of the harmonic approximation or it might be a consequence of not including configurational disorder. The latter is in line with previous MD studies showing a more broadly distributed orientation of the molecular dipole moments at higher temperatures [174, 175].

Summarizing our findings so far, we found good overall agreement between the theoretically computed and experimentally measured IR spectra of $\mathrm{CsPbBr_3}$ and $\mathrm{MAPbBr_3}$, except for an additional mode in $\mathrm{MAPbBr_3}$. Remarkably, this additional mode is only present in harmonic calculations for $\mathrm{MAPbBr_3}$ and absent in both $\mathrm{CsPbBr_3}$ and experimental data. There is convincing evidence from the data shown in figs. 3.6 and 3.7, as well as reference [166], that the mode is related to a tilting motion of the organic MA molecule which has a dipole moment. Performing MD simulations, as a method going beyond the harmonic approximation and periodic boundary conditions applied to a single unit cell, affects the theoretical results and increases agreement with experiment, suggesting a noticeable influence of anharmonic MA motion and configurational disorder. Besides this difference, the spectra of $\mathrm{CsPbBr_3}$ and $\mathrm{MAPbBr_3}$ are similar, implying constraints, as imposed by the harmonic approximation, on the MA molecule to be more important for IR spectra than the chemical composition of the A-site cation. Thus the IR spectrum of $\mathrm{MAPbBr_3}$ constitutes a first example that suggests to exploring methods beyond the harmonic approximation for HaPs.

3.3. Cubic perovskite structure as local maximum in potential energy

In the previous section, it was concluded that anharmonicity has to be included in theoretical methods for an accurate treatment of the dynamics of the organic A-site cation in $\mathrm{MAPbBr_3}$. However, from the above results it is less obvious whether an all inorganic HaP can be treated within the harmonic approximation. In order to investigate this, lattice dynamics of the high-temperature cubic structure of $\mathrm{CsPbBr_3}$ have been investigated. Figure 3.13 shows the harmonic phonon dispersion and

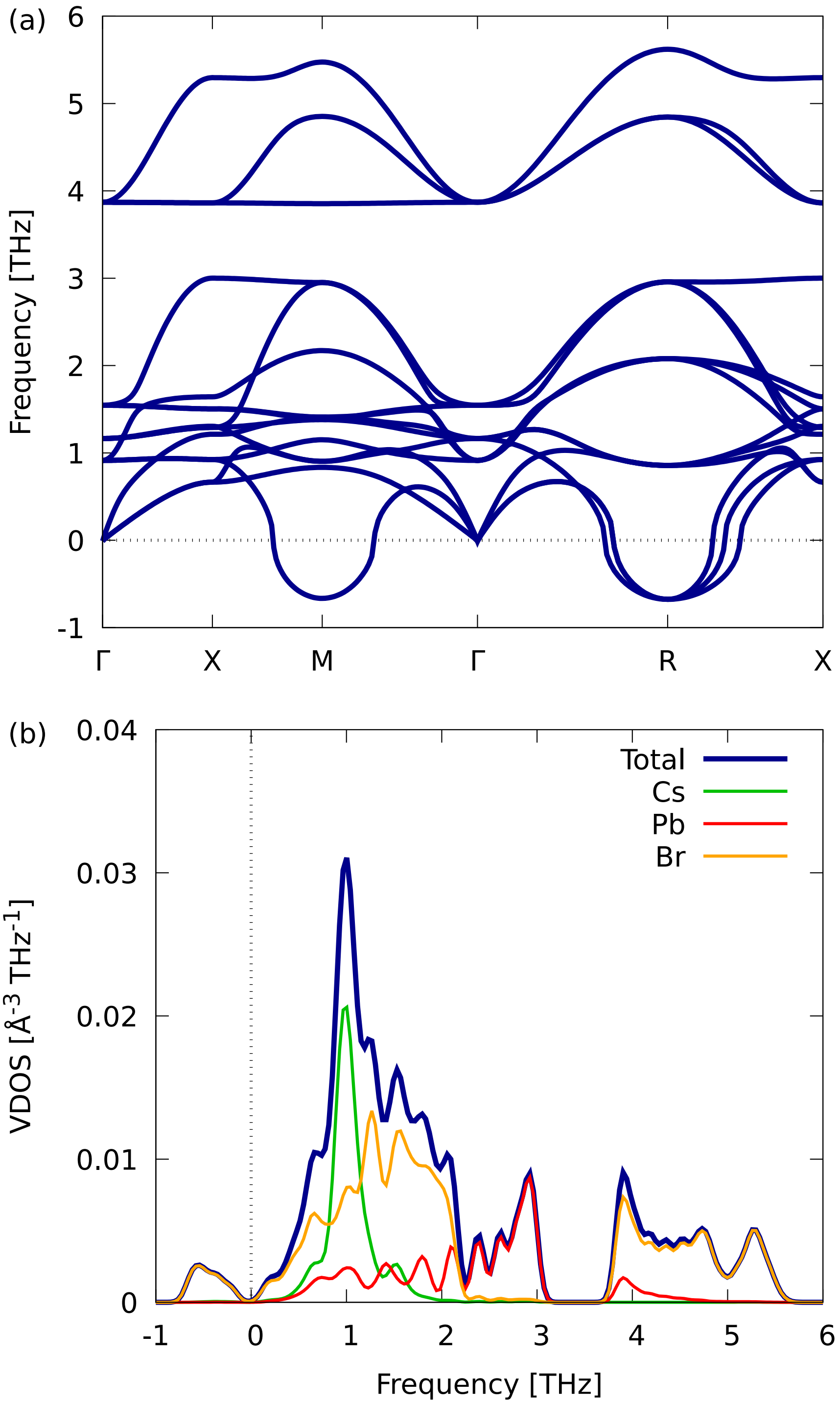

Figure 3.13.: **(a)** Phonon dispersion relation and **(b)** VDOS of cubic $CsPbBr_3$ as obtained from harmonic phonon calculations. The phonon density of states is further projected onto the contributions from Cs, Pb, and Br, respectively. Imaginary phonon modes, occurring at the M and R point of the Brillouin zone, are plotted as negative phonon frequencies.

VDOS of $CsPbBr_3$ in the cubic phase, as obtained from a DFT calculation within the harmonic approximation. A comparison to fig. 3.4 reveals the frequency range of orthorhombic and cubic $CsPbBr_3$ to be very similar. The number of branches shown for the orthorhombic phase, however, is much higher. This is simply a consequence of the number of phonon modes being $3 \times N$ with N the number of atoms in the unit cell. While only one formula unit, i.e., five atoms, is necessary to form the cubic unit cell, four formula units, i.e., 20 atoms, are required for the orthorhombic unit cell. A more striking feature, however, are the imaginary phonons, plotted as negative frequencies in fig. 3.13. To understand the mathematical origin and physical implication, we recap section 2.3. According to the harmonic theory introduced there, we obtain the squares of the phonon frequencies ω^2 as the eigenvalues of dynamical matrix D. If D has negative eigenvalues $\omega^2 = -\tilde{\omega}^2$, we obtain imaginary "frequencies"

$$\omega = \mathrm{i}\tilde{\omega} \ . \tag{3.2}$$

The time-dependent nuclear displacements are given by a plane-wave ansatz, eq. (2.42). If we now apply eq. (3.2) in eq. (2.42), we obtain

$$\mathbf{S}_I = \frac{1}{\sqrt{M_I}} \mathbf{A}_i(\mathbf{q})\, \mathrm{e}^{\mathrm{i}\mathbf{R}_n \cdot \mathbf{q}}\, \mathrm{e}^{-\mathrm{i}^2 \tilde{\omega} t} = \frac{1}{\sqrt{M_I}} \mathbf{A}_i(\mathbf{q})\, \mathrm{e}^{\mathrm{i}\mathbf{R}_n \cdot \mathbf{q}}\, \mathrm{e}^{\tilde{\omega} t} \ . \tag{3.3}$$

In other words, instead of an oscillatory motion, as described by the plane-wave ansatz in eq. (2.42), imaginary phonon modes describe an increasing nuclear displacement with time. Physically, imaginary modes describe a structural instability. Following the eigenvector associated with the imaginary phonon, one ends up in a lower energy structure. In case of HaPs, the imaginary phonon modes found at the Brillouin zone boundary (M and R point of the Brillouin zone) can be linked to octahedral tilting and related to the phase transitions to the low temperature orthorhombic and tetragonal phases [144, 150, 164]. This is further supported by the calculated phonon dispersion and VDOS of $CsPbBr_3$ in the orthorhombic phase, as shown in fig. 3.4, which do not show any imaginary phonon modes. The orthorhombic phase is the low temperature phase of $CsPbBr_3$ and thus expected to be stable at 0 K. Therefore, no imaginary phonon modes are expected and found to arise from effective 0 K DFT calculations.

The imaginary frequency modes in the harmonic phonon dispersion of cubic $CsPbBr_3$ suggest the structure to be at a local maximum of the potential energy surface. In particular, a detailed analysis revealed that the modes corresponding to the Brillouin zone boundary imaginary frequencies can be related to PbX_6 octahedral rotations [144, 150, 164] and the associated potential energy landscape to be of a double-well shape with the average atomic position located at a saddle point [26, 144–146, 149, 150]. Already about 60 years ago it has been suggested that the cubic structure of Cs-based HaPs actually has several potential minima with the Cs and halide atoms randomly distributed among different sites [176]. In this early work it was suggested, based on the analysis of X-ray data, that the halide atoms randomly populate one of four, the Cs one of six individual local potential energy minima each about 0.5 Å away from the average position. Twenty years later, this picture has been rejected and the cubic structure of these compounds has been explained in terms of the $Pm\bar{3}m$ cubic average atomic positions with large anharmonic contributions to the dynamics of Cs and halides present at temperatures relevant for the cubic phase [177]. This refined picture is based on a neutron diffraction study of cubic $CsPbBr_3$ and $CsPbCl_3$. With the renaissance of (hybrid organic-inorganic) HaPs as up-and-coming solar materials the anharmonic nature has been further studied and a picture of double-well potentials has been established [26, 144–146, 149, 150]. The transition time between the minima in the potential energy surface has been discussed to be related to the extremely short phonon lifetimes in these materials [26] and comparable with MA residence time in hybrid HaPs [145]. Evidence for transitions between instantaneous structures has also been observed experimentally, e.g., in Raman spectroscopy [24]. YAFFE ET AL. [24] predict transition times between instantaneous structures of the order of a few hundred fs, based on the width of the Raman central peak. This is remarkable since many experimental and theoretical studies report extremely short phonon lifetimes in the (sub-) ps regime [2, 22, 26]. Along these lines, first-principles MD simulations revealed octahedral tilting in the cubic phase leading to instantaneous tetragonal structures [21].

This motivates the use of MD simulations in the cubic phase of $CsPbBr_3$ to demonstrate that the ideal cubic structure is a local maximum in the total energy surface and that this is different to conventional materials, such as Si. Figure 3.14a shows the difference in total energy between the ideal cubic structure, E_{cubic}, and instantaneous nuclear configurations, E_i, obtained from MD simulations:

$$\Delta E = E_i - E_{\text{cubic}} \ . \tag{3.4}$$

The negative sign of ΔE in fig. 3.14a shows that the total energy of instantaneous configurations is lower than that of the ideal high-symmetry structure [158, 178]. This is substantially different to Si (fig. 3.14b), where the positive sign of ΔE demonstrates the total energy of instantaneous configurations to be higher than that of the ideal structure. Usually, one expects the equilibrium (high symmetry) structure to be the structure with the lowest total energy, and thus atomic displacement, e.g., due to lattice dynamics to increase the total energy, as observed for Si. Therefore, the situation in cubic HaPs contradicts intuitive expectations and the above results are another endorsement of picture to have the ideal structure located at a local maximum.

Consequently, one could ask whether lattice dynamics in cubic HaPs should be understood as low frequency relaxational motions between instantaneous configurations plus (harmonic) phonons around these new equilibrium positions. Already the definition of phonons (quasiparticles) requires a reference structure (see section 2.3) and therefore is difficult to reconcile with the presence of instantaneous configurations and local minima in the potential energy surface. As a consequence, lattice dynamics in cubic $CsPbBr_3$ are difficult to be explained by means of harmonic approximation with a cubic reference structure. Even if perturbatively including higher order corrections of the Taylor series of the lattice potential, eq. (2.39), this approach to lattice dynamics will not capture relevant effects of lattice dynamics, as it starts from the cubic reference structure, and thus may not fully explain, e.g., the

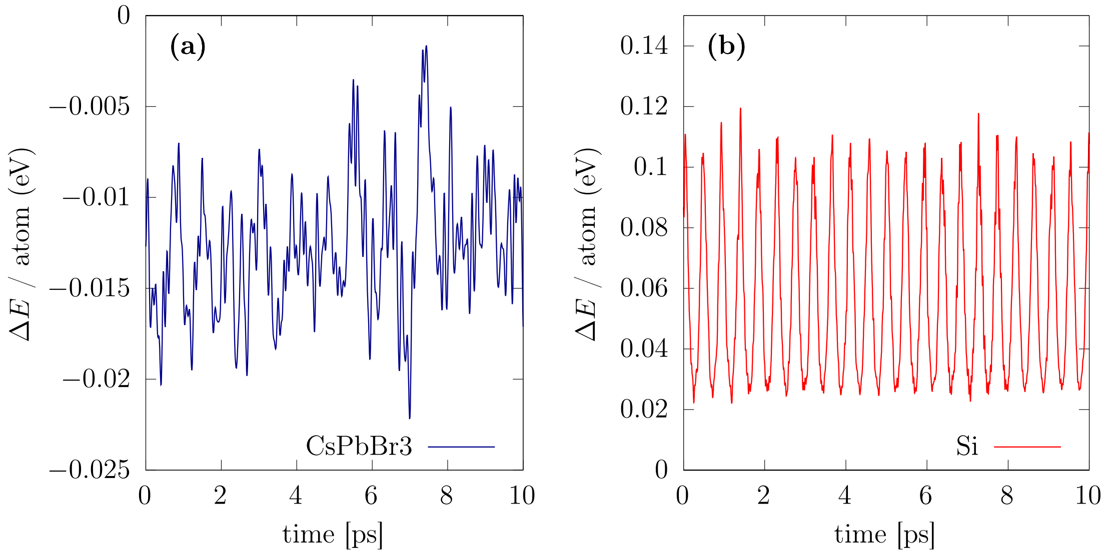

Figure 3.14.: Change of the total energy (excluding kinetic energy of the ions and the energy of the thermostat) per atom as a function of time during an MD simulation. Shown is the difference $\Delta E = E_i - E_{\mathrm{equi}}$ between instantaneous total energies E_i and the total energy of the equilibrium structure E_{equi} for **(a)** $CsPbBr_3$ and **(b)** Si. Instantaneous structures, i.e., atoms displaced from the equilibrium structure lead to lower total energies ($\Delta E < 0$) in $CsPbBr_3$ whereas in Si displaced atoms increase the total energy ($\Delta E > 0$).

low frequency relaxational motion between different instantaneous configurations observed, e.g., in Raman spectroscopy and first-principles MD simulations.

This can be expected to also influence functional properties as the physical observable predicted from the average structure is not necessarily the same as the average of the observable taken over different (instantaneous) structures. As a consequence, the cubic perovskite structure fails to predict many properties of HaPs. A list of such observables has recently been discussed for static properties, using a static approach of “polymorphous networks” [178] to mimic the distribution of atoms in its refined total energy minimum. Interestingly, these ”polymorphous networks”, obtained by theoretically relaxing atom positions of beyond unit cell configurations, looking for the configuration with minimal total energy, are characterized by PbX_6 octahedral rotations and B-site displacements when compared to the monomorphous $Pm\bar{3}m$ cubic structure. Thus this approach is in great agreement with the picture of finding the ideal structure at a local maximum of the potential energy surface. Here, we will recapitulate and extend this list from reference [178]. Difficulties already start with attempting to unravel the exact structure. First, although the average atomic positions and long range order, as measured by X-ray diffraction, can be explained by the $Pm\bar{3}m$ cubic structure, mutual agreement between theory and experiment for more local structural details, as measured by the pair distribution function, can only be achieved if local distortions are allowed for in theory. These local motifs include, but are not limited to, octahedral tilting and B-site displacements. Second, the

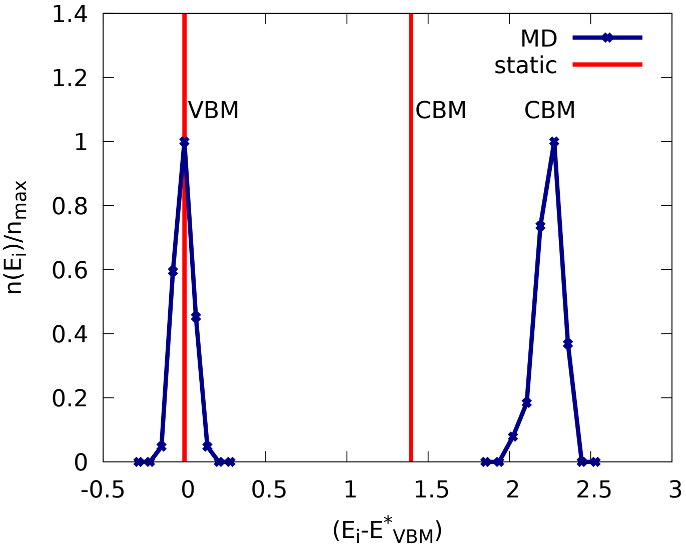

Figure 3.15.: Band-edge energy distributions shown as histograms of the instantaneous VBM and CBM energies E_i obtained from a MD simulation at T=425 K. Vertical lines show VBM and CBM for a static calculation of an ideal system with cubic $Pm\bar{3}m$ symmetry. The histograms are normalized by the highest occurrences $n_{\max} = n(E^*_{\mathrm{VBM/CBM}})$ for VBM and CBM, respectively. The nominal band gap $E^*_{\mathrm{gap}} = E^*_{\mathrm{CBM}} - E^*_{\mathrm{VBM}}$ is given by the difference between the VBM/CBM energies with the highest occurrence, $E^*_{\mathrm{VBM/CBM}}$.

cubic structure fails to predict the band gap, with changes of up to 300% in “polymorphous” vs. “monomorphous” DFT calculations. While calculating the effect of disorder correlation lengths on band-edge energy distributions (see section 3.6), we discovered a significant difference between the band gap of a cubic unit cell and snapshots from MD calculations, see fig. 3.15. This remarkable finding has been discussed and explained by the “polymorphous network” picture [178] independent from our work while our work was still in progress. Even the relative order of band gaps with respect to phase transitions is not maintained with “monomorphous” cubic calculations. Third, mixing enthalpies are corrected by using polymorphous networks. And last but not least, a much larger dielectric constant, with substantial ionic contributions, is obtained. On the other hand, using a polymorphous approach does not contradict properties which usually are related to high symmetry unit cells, such as sharp bands and small Urbach energies [178].

The above paragraphs establish that the cubic structure as such is difficult to rationalize in a static or harmonic picture. This conclusion has been approached from different directions, e.g., rationalizing imaginary phonon modes, “polymorphous networks”, and experimental data such as Raman spectra and X-ray measurements.

3.4. Anharmonic phonon quasi-particles

Note that parts of the results presented in sections 3.4 to 3.8 are published in references [2, 5].

Motivated by the discussion above, the role of anharmonicity in the all-inorganic HaP is investigated, ruling out the anharmonic motion of the organic molecule with its anisotropy and dipole moment. We thus characterize vibrational properties of cubic $CsPbBr_3$ by analyzing first-principles MD simulations using a projection of the VACF on harmonic phonon modes (section 2.4.3). Vibrational quasiparticle properties as obtained from MD are shown in fig. 3.16. First of all, fig. 3.16a shows the phonon dispersion at 425 K, compared to the phonon dispersion obtained from the harmonic approximation. The dispersion relations of these two cases are rather similar, except for two key features we would like to further discuss.

One striking difference is the absence of imaginary modes (plotted as negative frequencies) at 425 K. This is to be expected as the imaginary phonon modes at the boundaries of the first Brillouin zone (M and R point) are related to octahedral tilting and thus to the phase transitions to tetragonal and orthorhombic structural phases at low temperature. This connection has been discussed before in literature for related materials, e.g., references [144, 150], and very recently also again for $CsPbBr_3$ [164]. Displacing atoms according to the eigenvector of an imaginary phonon mode one obtains a lower energy structure. In cubic HaPs these modes ap-

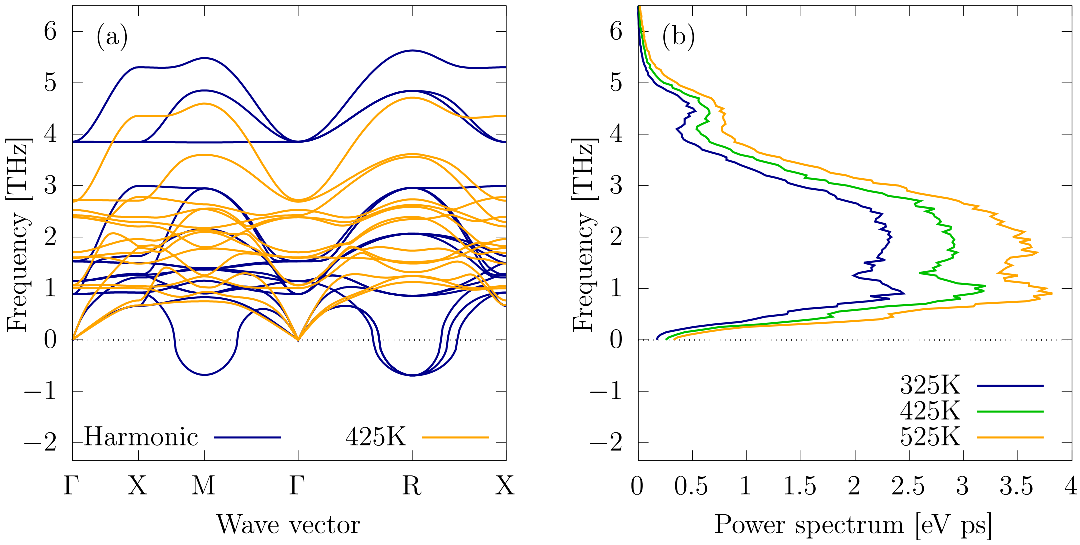

Figure 3.16.: **(a)** Phonon dispersion of $CsPbBr_3$ as obtained from calculations in the harmonic approximation (orange) and from MD simulations at $T = 425$ K (blue). **(b)** Power spectrum of the VACF obtained from MD simulations at $T = 325$ K, $T = 425$ K, and $T = 525$ K. *Reprinted with permission from [2], published under a CC BY 4.0 license.*

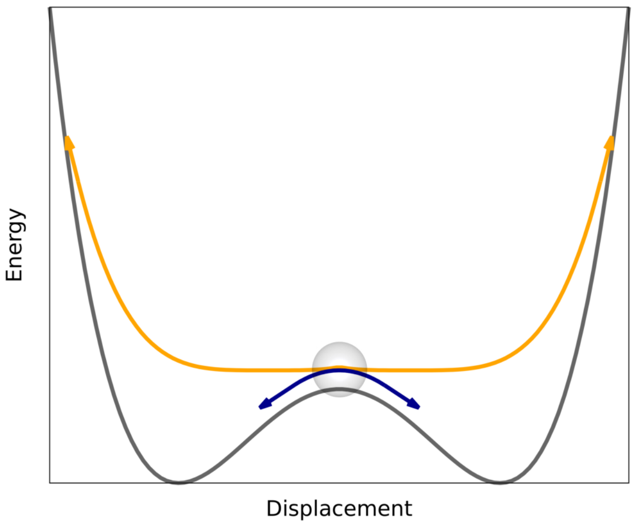

Figure 3.17.: Sketch explaining imaginary (harmonic approximation) and finite frequencies (MD) in a double-well potential (gray): the harmonic frequency is determined by a quadratic approximation of the potential close to the local maximum (indicated in blue). Moreover, at low temperatures, atom are expected get caught in a local minimum. At high enough temperatures, however, a larger part of the potential energy landscape is accessible to the atoms and the atoms can oscillate with finite temperature as indicated in orange.

pear to be associated with a double-well potential [144, 150] whose local maximum is located at the average structure. Atomic displacements according to the harmonic approximation would thus lead to a lower energy structure, thus the presence of imaginary frequencies, and at low temperatures the material would be expected to get trapped in one of the local minima. Eventually, as temperature increases, thermal energy is higher than the energy barrier of the double-well potential, thus it can be overcome and a larger area of the potential energy landscape is accessible (see sketch in fig. 3.17). Consequently, atomic oscillations around the average position are found, resulting in a finite frequency when projecting this atomic motion onto the harmonic phonon eigenvector. The consistency of our findings, no imaginary phonon modes from MD at 425 K, with this picture is further supported by a comparison with the experimentally measured phase transition temperature, approximately 400 K [151], and with the theoretically obtained potential well depth, about 26 meV/atom [164] which is, converted to $k_B T$, equivalent to around $T \approx 302$ K.

The second difference is the shift in the highest frequency optical phonon branches. This shift might be due to a “simple” temperature effect, however the effect on these modes is rather large compared to the effect of temperature on other modes. As an alternative explanation, it might as well be a pressure effect. Since our MD simulations at different temperatures are performed as NVT simulation, all of them with the same volume obtained from a optimization of the unit cell at 0 K, pressure is increasing with increasing temperature. Wang et al. [179] have studied the effect of pressure on phonon properties of $MAPbI_3$ using NPT MD simulations.

Table 3.1.: Range of phonon quasi-particle lifetimes of $CsPbBr_3$ at three different temperatures, specified for acoustic modes and optical modes, respectively. And mean phonon quasi-particle lifetimes as obtained from the histograms in fig. 3.18b. *Reprinted and adapted with permission from [2], published under a CC BY 4.0 license.*

Temperature	Acoustic modes	Optical modes	Mean
325 K	0.5–9.5 ps	0.3–4.6 ps	1.38 ps
425 K	0.4–6.7 ps	0.3–4.4 ps	1.25 ps
525 K	0.5–5.4 ps	0.3–2.8 ps	1.08 ps

Although the inorganic lattice has not been a focus of their work, fig. 3c and d of their publication show very clearly that changing the pressure from 1 bar to 6 bar shifts the higher end of the inorganic (PbI contributions) VDOS from about 5 THz to about 4 THz. Although we are considering a different material, even having a different X-site atom, and no systematic pressure was applied, the effect we observe here for $CsPbBr_3$ is similar to the effect observed in $MAPbI_3$ [179] rendering it possible that this observation is related to a pressure effect.

In fig. 3.16b the power spectrum of the VACF, which is related to the VDOS as discussed in section 2.4.2, is shown. Compared to the VDOS obtained from calculations within the harmonic approximation (cf. fig. 3.13) the features appear strongly broadened. The width in frequency space can be related to vibrational lifetimes as explained in section 2.4.3. In particular by projecting the VACF onto harmonic phonon eigenvectors, quasiparticle lifetimes can be obtained. A plot of lifetimes as a function of frequency can be seen in fig. 3.18a. The (short) phonon lifetimes are attributed to phonon-phonon scattering. This is supported by our observation that the frequencies with the highest intensities of the VDOS (fig. 3.16b) seem to be correlated with the frequencies at which the shortest vibrational lifetimes are found (fig. 3.18a). In other words, phonon-phonon interactions appear to be strongest between 1 and 3 THz due to the presence of a high number of vibrational states, manifesting itself in a high density of states. The vibrational lifetimes span between 0.3 ps and 10 ps (table 3.1) and are thus extremely short. For comparison, the phonon lifetimes calculated here for $CsPbBr_3$ are two orders of magnitude shorter than, e.g., phonon lifetimes in bulk silicon [180].

A different visualization of the vibrational lifetimes, i.e., a histogram of the phonon lifetime is shown in fig. 3.18b. From this representation we can obtain further insight: first of all, the average phonon lifetime (horizontal lines in fig. 3.18b) is decreasing with increasing temperature (cf. also table 3.1). This is consistent with the picture of increasing anharmonicity and phonon-phonon interactions with increasing temperature. And second, we observe that the lower end in the distribution of vibrational lifetimes hardly shifts towards shorter lifetimes, with even the maximum of the distributions of all three temperatures not changing much. Instead , the quasiparticle lifetimes seem to reach a physical limit. A reasonable lower limit is given by the period of the vibrational frequency, i.e., atoms have to undergo at least one full period in order to have a vibrational quasiparticle.. In the case of HaPs this

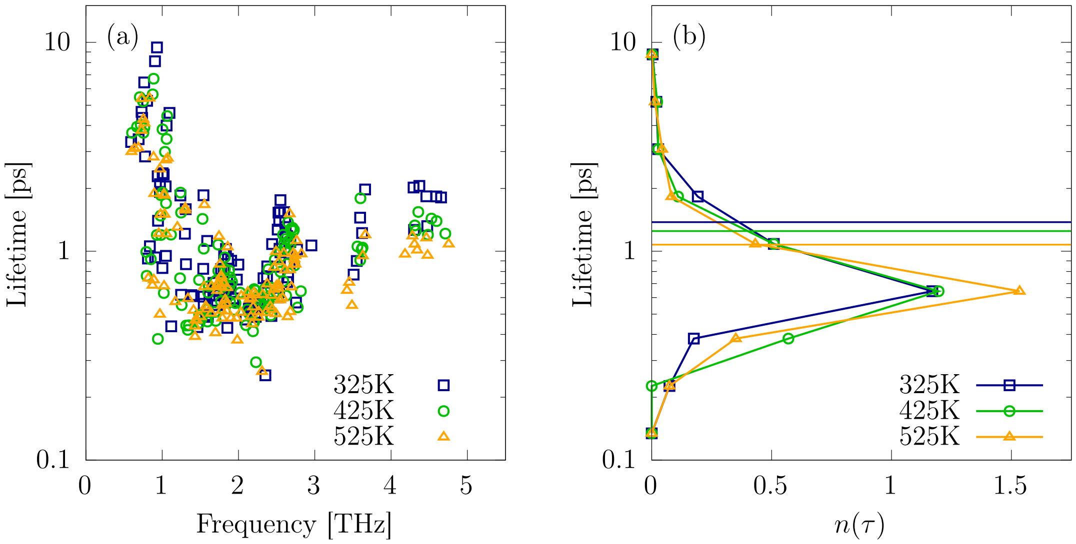

Figure 3.18.: **(a)** Phonon quasi-particle lifetimes as a function of quasi-particle frequency obtained from MD simulations at $T = 325$ K, $T = 425$ K, and $T = 525$ K. **(b)** Histograms of the phonon quasi-particle lifetimes τ at three different temperatures. The histograms are normalized such that the integral over the range is 1. The horizontal lines indicate the mean values, see table 3.1 for details. *Reprinted with permission from [2], published under a CC BY 4.0 license.*

limit seems approached for all temperatures considered here (see also [158]). We can thus conclude that anharmonicity is a strong and important effect in HaPs and that it would be interesting to elucidate its microscopic origin.

3.5. Resonant bonding

A phenomenon that has been related to anharmonicity in HaPs is called *resonant bonding* [158, 181]. This mechanism, also active in other materials [182, 183], originates from orbital degeneracy. Metaphorically speaking, this quantum mechanical effect can be illustrated as a frequent change between configurations that are degenerate. As a consequence, an effective configuration establishes, which is known as a resonant network. In this regard, it can be understood as an extension of the bonding resonance known, e.g., from the benzene ring to crystals [184]. However, at finite temperature the material undergoes atomic motion, which breaks the degeneracy and favors specific configurations over the effective configuration. As the resonant network and thus also the breakdown of the effective configuration go through large parts of the material, resonant bonding can be considered to be a long-range interaction. The long-range nature is illustrated for the example of $CsPbBr_3$. In fig. 3.19a the change in the charge density upon displacing a single Pb atom is shown. The response of the charge density is obviously long-ranged, since

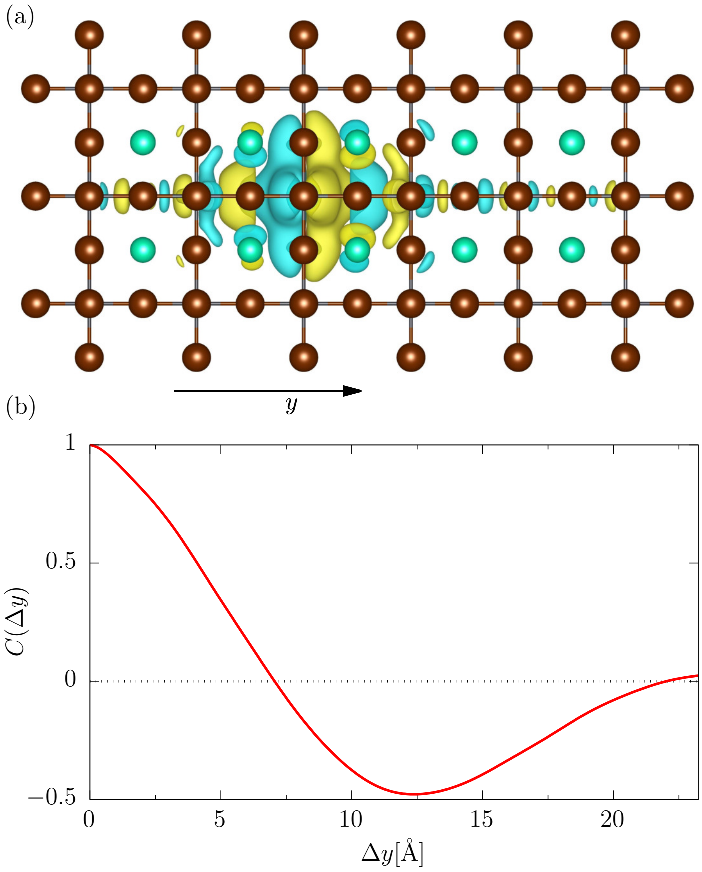

Figure 3.19.: Long-range resonant bonding in $CsPbBr_3$. **(a)** Difference in the charge-density induced by displacing a single Pb atom, visualized as an isosurface plot. **(b)** Autocorrelation of the disorder potential for electronic states, calculated according to eq. (2.120). *Reprinted with permission from [2], published under a CC BY 4.0 license.*

it implies a response significantly larger than one unit cell. Figure 3.19b shows that this long-range response of the charge density can quantitatively be observed in the correlation length for the disorder potential, eq. (2.120). A significant correlation $C(\Delta y)$ can be seen for distances $\Delta y > 12$ Å, which by far exceeds the 5.8 Å lattice parameter of $CsPbBr_3$ by far. Therefore, the above described resonant bonding mechanism is suggested to cause long-range effects in the dynamical matrix and, more importantly, induce anharmonicity [182]. Moreover, as discussed in section 2.5 and the following section, this long-range correlation of the disorder potential would significantly impact the functional properties of HaPs.

It is worth noticing that the observations of fig. 3.19 are not specific for the displacement shown in fig. 3.19, the same behavior would also have been observed when displacing any of the other atoms. This can be understood by considering all the atoms which still are at their undisplaced, ideal positions to form the resonant network inside the material and being responsible for the long-range correlation.

3.6. Disorder correlations and band-edge distributions

As discussed in section 2.5, the correlation length of the disorder potential can be linked to the Urbach energy. A long-range correlation as found in section 3.5 implies a large Urbach energy. This is seemingly in contrast with the small Urbach energies measured experimentally [127–131]. To further study this, we calculated the correlation in the disorder potential for instantaneous snapshots from MD simulations. While fig. 3.20a clearly demonstrates changes in the charge density to be present all over the simulated system for instantaneous nuclear configurations, remarkably, the correlations obtained from MD simulations, shown in fig. 3.20b are short ranged. The correlations decay on the range of half a unit cell, i.e., on the order of interatomic distances. Naturally, the question arises how the correlation is shortened comparing it to the correlation in fig. 3.19.

To examine this question we considered constraint cases, resembling intermediate scenarios between the cases of only a single displaced Pb atom and "full MD". For these intermediate cases certain atoms are displaced according to MD displacements while the other atoms have been kept at their ideal average lattice positions. In detail, we considered the cases where all Pb atoms have been displaced, but Cs and

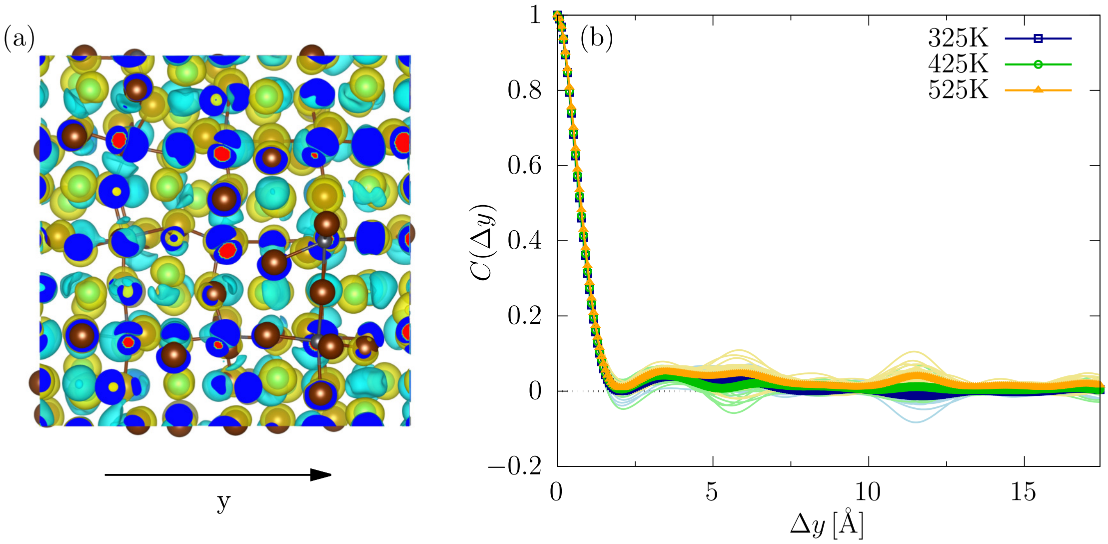

Figure 3.20.: **(a)** Difference in the charge-density between an instantaneous configuration and the mean density taken from a MD trajectory at $T = 425$ K. **(b)** Autocorrelation of the disorder potential for electronic states, calculated according to eq. (2.120). The thin curves show the autocorrelation functions for instantaneous snapshots of MD trajectories at three different temperatures. The thick lines represent the averages of the instantaneous configurations. *Reprinted with permission from [2], published under a CC BY 4.0 license.*

Br atoms were fixed ("Pb MD"), the case were Pb and Cs atoms have been displaced and Br was fixed ("Pb + Cs MD"), and the case were Pb and Br atoms have been displaced and Cs was fixed ("Pb + Br MD"). The results of these *gedanken-experiments* can be seen in fig. 3.21. There, one can observe that the correlation is of somewhat longer range, compared to the ones observed in fig. 3.20, when only Pb atoms are displaced. However, it gets shortened to (almost) the MD correlation length as soon as the A-site cation Cs or, in particular, the halide ion Br are displaced in addition. We can thus conclude that the correlations in the disorder potential get dynamically shortened especially by the large displacements of Cs and Br ions.

According to section 2.5 the changes in the correlation length should be related to the Urbach energy. To test this hypothesis, we studied the band-edge distributions, i.e., the distributions of the VBM and CBM for two paradigmatic cases with different correlation lengths. We choose the case for which we obtained the shortest correlation length, the "full MD" case and the constrained MD simulation with the longest correlation length, which is the "Pb MD" case.

In fig. 3.21 the band-edge distributions for these two cases are shown. In agreement with our expectations, we first of all observe that the distributions of VBM and CBM are broadened for both cases at finite temperature. This is a consequence of different ionic configurations, as obtained from instantaneous MD snapshots, providing slightly different electronic structures. Second, we observe that the "Pb MD" case shows an additional tail for the CBM distribution. This can be understood from the fact that the conduction band in this material is mainly formed from the Pb p-orbitals, which are also predominant in the resonant-bonding mechanism discussed above. And last but not least, we observe that the band-edge distributions for the "full MD" case is narrower than for the "Pb MD" case. This is in perfect agreement with our hypothesis that the correlation length of the disorder potential determines the number of electronic tail states. As predicted by this hypothesis, the case with the shorter correlation length exhibits the narrower band-edge distributions. This is remarkable, however, as this implies that increasing the number of activated degrees of freedom reduces the number of tail states observed. With this, we established the relation between correlation length of the disorder potential and band-edge energy distributions. Allowing to better understand one of the key properties of HaPs, namely their small Urbach energies and efficient optical absorption.

An even more direct approach to investigate optical absorption is provided by the JDOS which counts possible band-to-band transitions [124, 185–187]. Previous work on HaPs already found the JDOS to increase rapidly close to the band edge when compared to other materials [188–190]. However, so far calculations have only been performed for static cells. Figure 3.22 shows the JDOS of $CsPbBr_3$ for the static as well as a dynamic picture. The dynamic JDOS is represented by the JDOS calculated for instantaneous configurations extracted from a MD trajectory at 425 K as well as their average. Indeed, the dynamic JDOS increases much faster than the static JDOS emphasizing once more the importance of dynamics for understanding important physical properties of HaPs in the cubic phase. This is in line with the

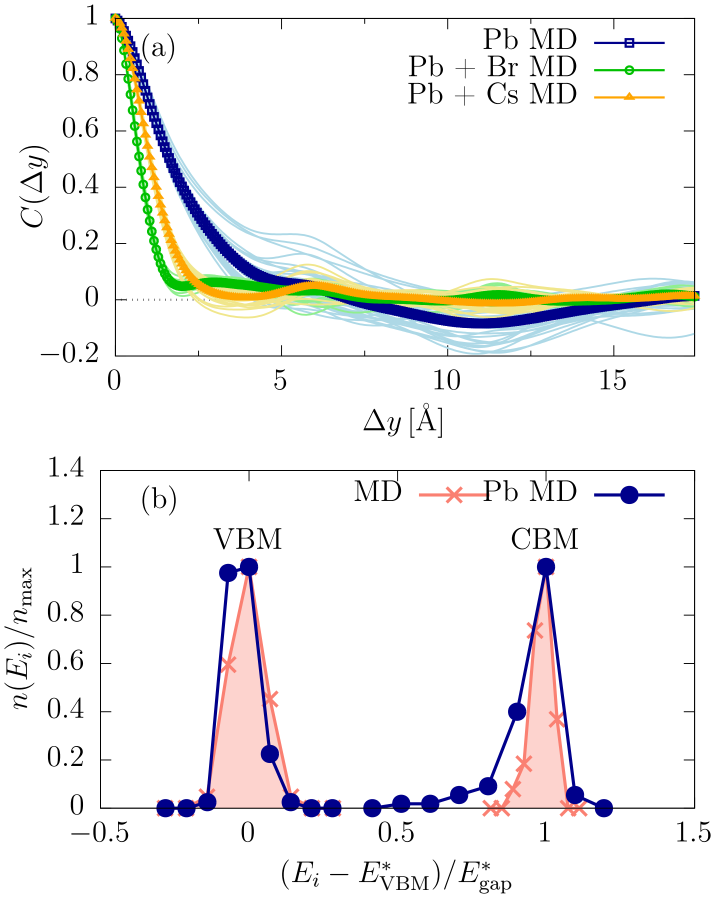

Figure 3.21.: **(a)** Autocorrelation of the disorder potential for electronic states, calculated for three different scenarios. (i) Pb atoms are displaced and Cs and Br atoms are fixed to their ideal lattice positions (blue curves). (ii) Pb and Br atoms are displaced and Cs atoms are fixed (green curves). (iii) Pb and Cs atoms are displaced and Br atoms are fixed (orange curves). All displacements are according to MD simulations at $T = 425$ K. The thin curves show the autocorrelation functions for instantaneous configurations. The thick lines represent the averages of the instantaneous configurations. **(b)** Band-edge energy distributions shown as histograms of the instantaneous energies E_i. Shown are valence band maximum (VBM) and conduction band minimum (CBM) energy distributions for two scenarios: instantaneous configurations are taken along a MD simulation at $T = 425$ K (red curve) and scenario (i) of panel (a) (blue curve). The histograms are normalized by the highest occurrences $n_{\max} = n(E^*_{\mathrm{VBM/CBM}})$ for VBM and CBM, respectively. The nominal band gap $E^*_{\mathrm{gap}} = E^*_{\mathrm{CBM}} - E^*_{\mathrm{VBM}}$ is given by the difference between the VBM/CBM energies with the highest occurrence, $E^*_{\mathrm{VBM/CBM}}$. *Reprinted with permission from [2], published under a CC BY 4.0 license.*

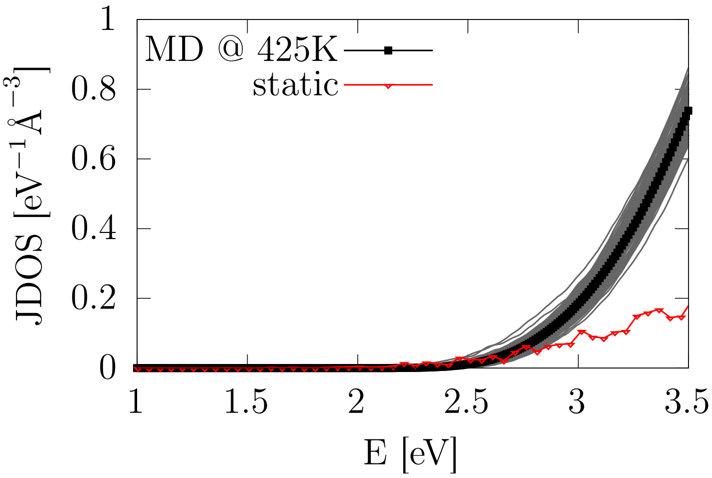

Figure 3.22.: Static and dynamic JDOS of $CsPbBr_3$. The thin gray curves show the JDOS for instantaneous snapshots of a MD trajectory at T=425 K. The thick black line represent the averages of the instantaneous configurations. The red line shows the static JDOS for a cubic perovskite structure. *Reprinted with permission from [5], published under a CC BY 4.0 license.*

findings above which suggest narrower band-edge energy distributions and thus an even steeper increase of band-to-band transitions close to the band gap in the case of a dynamic picture In addition, there is a second difference: the onset of the JDOS differs between the dynamic and static JDOS by about 0.5 eV, respectively. This can be linked to the difference between the band gap of a static perovskite structure and the average band gap of $CsPbBr_3$ as obtained from MD simulations, which has already been shown in fig. 3.15, section 3.3. At this point, there is strong evidence that dynamics in $CsPbBr_3$ significantly influence optical absorption. Below, this will be tested for different HaP compounds and attributed to an intrinsic characteristic of the perovskite structure, namely its dynamic flexibility.

3.6.1. Ionic composition

As discussed in the introduction (section 3.1), the class of HaPs contains a variety of compounds with an ABX_3 stoichiometry. Even when focusing on lead-halide perovskites, i.e., constraining B to Pb and X to be a halide, there is still broad flexibility within the possible compounds. Here, we test our findings of dynamically shortened disorder potential correlations with HaPs of different chemical composition.

We start by changing the halide ion to iodine, thus considering $CsPbI_3$. In fig. 3.23a we show the correlation function as obtained from MD simulations at 425 K. Similar to $CsPbBr_3$, the correlation decays on the range of interatomic distances, revealing a short range correlation. To investigate the mechanisms that shorten the correlation

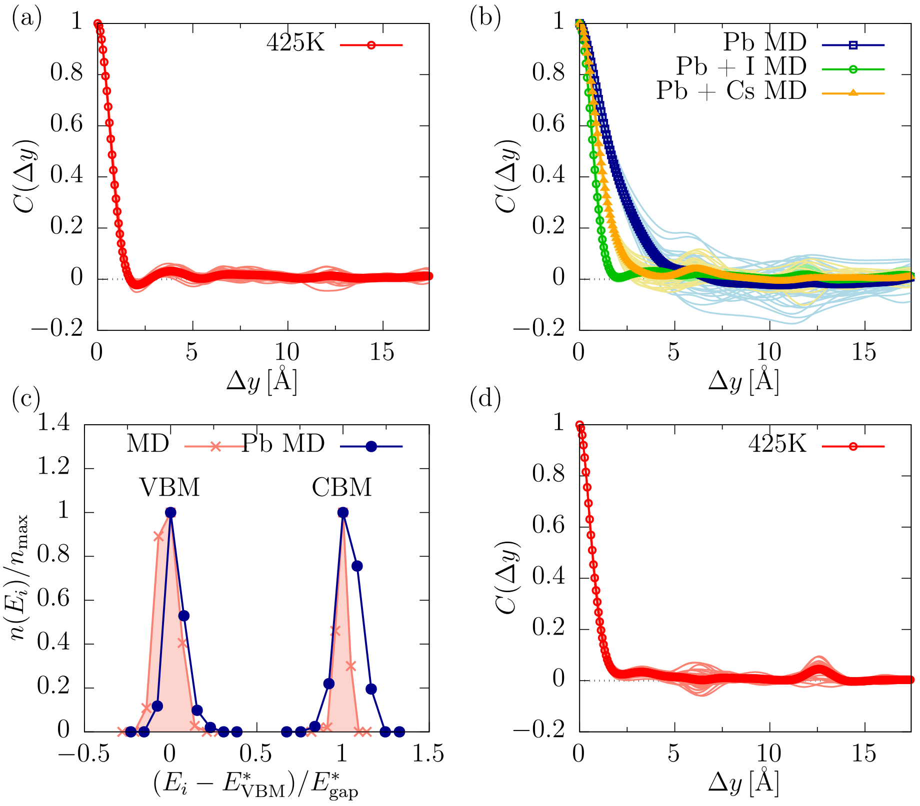

Figure 3.23.: Autocorrelation of the disorder potential for electronic states in $CsPbI_3$ as obtained from **(a)** MD simulations and **(b)** calculated for three different scenarios similar to fig. 3.21a. **(c)** Band-edge energy distributions for $CsPbI_3$, obtained similar to fig. 3.21b. **(d)** Autocorrelation of the disorder potential for electronic states in $MAPbI_3$ as obtained from force-field MD simulations. *Reprinted with permission from [2], published under a CC BY 4.0 license.*

function, the procedure reported for $CsPbBr_3$ has been repeated. In fig. 3.23b the correlation functions for constrained simulations are shown. In case of only Pb being displaced ("Pb MD") the correlation is more long range compared to the case of "full MD" (fig. 3.23a) and the cases of "Pb + I MD" and "Pb + Cs MD". Thus, the findings are similar to those for $CsPbBr_3$. However, besides the similarities of $CsPbBr_3$ and $CsPbI_3$, there is also one difference. Considering only Pb displacements induces a partially negative correlation at a distance of about two lattice parameters. Compared to $CsPbBr_3$ (fig. 3.21a), this is hardly visible in $CsPbI_3$ (fig. 3.23b) at least on average. This difference can be rationalized considering iodine has a larger atomic polarizability, which would imply that the iodine lattice provides more screening than the bromine lattice.

Last but not least, we investigate the hybrid organic-inorganic HaP $MAPbI_3$. $MAPbI_3$ is the paradigmatic HaP for solar-cell applications and has been shown to feature resonant bonding and long-range effects [158]. Occupying the A-site with the organic MA molecule instead of the inorganic Cs atom makes the system anisotropic.

The permanent dipole moment of the MA molecules further allows for additional long-range order, due to oriented dipoles. On the other hand, disarranged molecules might introduce additional disorder and screening of the correlation. The correlation function for the disorder potentials was calculated similar to the correlations shown for $CsPbBr_3$ and $CsPbI_3$, but for instantaneous atomic configurations obtained from force-field MD (see fig. 3.23d). Again, we find the correlation to be short-ranged. This finding is consistent with the notion that at elevated temperature the orientation of the MA molecules is disordered, as we, e.g., discussed already for $MAPbBr_3$ in section 3.2. An analysis of constrained MD cases is complicated by the orientational degrees of freedom of the MA molecules. Due to this additional complexity for the constraints no further gedankenexperiments have been performed for $MAPbI_3$.

As a bottom line, we have found short-range correlated disorder potentials in all HaP examples we studied and conclude that this is important for their functional properties due to the implications for band-edge distributions and Urbach energy. In particular, the correlations are dynamically shortened due to A-site and especially due to halide motion. The latter will be further studied in the following section.

3.7. Impact of strongly anharmonic transversal halide motion

The strong impact of the halide motion on the disorder potential and thus band-edge distributions motivates further studying it. A useful starting point is a peculiarity of the cubic perovskite structure, i.e., that there exists a "directionality" in halide bonding. In particular, in the ideal cubic perovskite geometry, there exists a linear Pb-X-Pb bonding, while the halide ions exhibit no bonding in any other direction (cf. fig. 3.24a). This allows for the definition of a *longitudinal* (blue arrows in fig. 3.24a) and *transversal* direction (yellow arrows in fig. 3.24a) with respect to the Pb-Br-Pb bond in $CsPbBr_3$. To compare the transversal displacements to the longitudinal displacements, the *transversality* has been defined as

$$\eta = \frac{1}{N_{\mathrm{Br}}} \sum_{i}^{N_{\mathrm{Br}}} \frac{d_i^{\mathrm{transv}}}{d_i^{\mathrm{longi}}} , \tag{3.5}$$

where $d_i^{\mathrm{transv/longi}}$ are the (absolute) transversal/longitudinal displacements of Br atom i and N_{Br} denotes the total number of Br atoms considered in the analysis. Thus, the transversality can be interpreted as the averaged ratio between transversal and longitudinal components of Br displacements, with a large transversality ($\eta \gg 1$) indicating that, on average, transversal displacements are larger than longitudinal displacements. A histogram of the transversality, as obtained for a system containing 96 Br ions and from a MD trajectory of 150 ps at 425 K can be seen in fig. 3.24b. This histogram is peaked at around $\eta \approx 15 - 20$ ($\log_{10}(\eta) \approx 1.2 - 1.3$) and quickly decays for η approaching 1. Consequently, the histogram reveals large

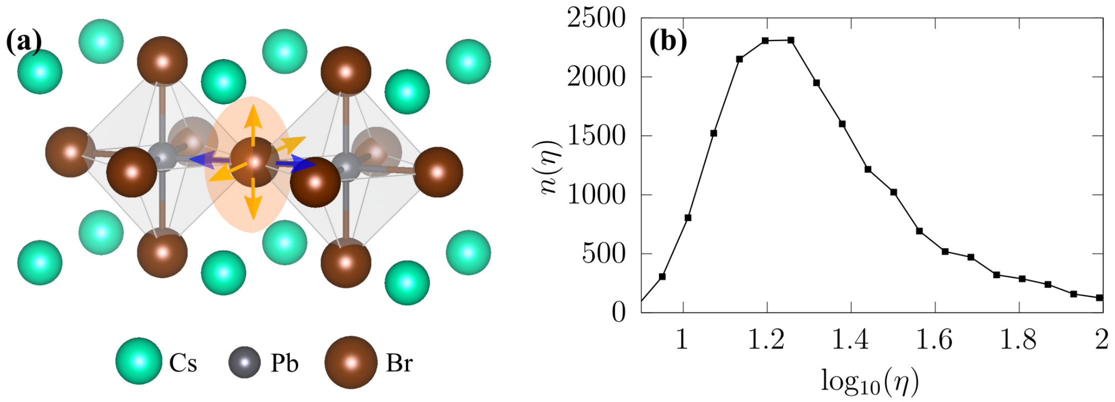

Figure 3.24.: **(a)** Visualization of longitudinal Br displacements (parallel to Pb-Br-Pb bonds, blue arrows) and transversal Br displacements (in plane perpendicular to the Pb-Br-PB bonds, sketched in orange). **(b)** Semi-log plot of the histogram of the transversality, η, eq. (3.5), as obtained from an MD simulation at 425 K containing 96 Br atoms. *Reprinted with permission from [5], published under a CC BY 4.0 license.*

transversal displacements. Alternatively, the histograms of transversal and longitudinal displacements, fig. 3.25, can be inspected directly. The broader spread for the components of transversal displacements in comparison to the longitudinal displacements in fig. 3.25a, as well as the broader spread and the shift of the peak to higher values for the norms of the displacements in fig. 3.25b result in the same conclusion of larger transversal displacements. On top, as shown in fig. 3.26, potential energy landscapes $U(\delta r_1, \delta r_2, \delta r_3)$ for specific transversal and longitudinal directions can be deduced from this. The potential energy landscapes are obtained from inversion of the histograms of the displacements, $n(\delta r_1, \delta r_2, \delta r_3)$. Since the histograms are obtained from MD simulations, Boltzmann statistics can be assumed:

$$n(\delta r_1, \delta r_2, \delta r_3) \propto \exp\big\{-U(\delta r_1, \delta r_2, \delta r_3)/k_B T\big\} \; . \tag{3.6}$$

Accordingly, the potential energy landscapes can be calculated as:

$$U(\delta r_1, \delta r_2, \delta r_3) = -\ln\big\{n(\delta r_1, \delta r_2, \delta r_3)\big\} \cdot k_B T + const. \tag{3.7}$$

However, for this method one has to consider that the result would be the potential energy landscape as a function of all three spatial coordinates $\delta r_1, \delta r_2, \delta r_3$. For simplicity, fig. 3.26 shows the potential energy only along exemplary paths in which two directions are kept at 0, i.e.,

$$U(\delta r_1) = U(\delta r_1, \delta r_2 = 0, \delta r_3 = 0) = -\ln\big\{n(\delta r_1, \delta r_2 = 0, \delta r_3 = 0)\big\} \cdot k_B T + const. \tag{3.8}$$

This is in contrast to fig. 3.25, where the one-dimensional histograms were obtained by integrating out the other components, i.e.,

$$n(\delta r_1) = \iint d\delta r_2 \, d\delta r_3 n(\delta r_1, \delta r_2, \delta r_3) \; . \tag{3.9}$$

The potential energy landscapes obtained according to eq. (3.8) provide much shallower potentials for transversal displacements, i.e., large longitudinal displacements

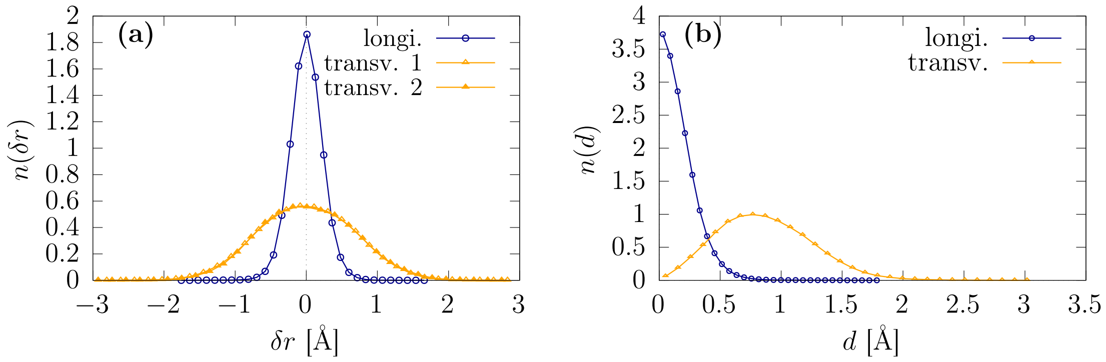

Figure 3.25.: Distribution of Br displacements in $CsPbBr_3$, projected onto longitudinal and transversal components. In **(a)** histograms for one longitudinal and two transversal components $\delta r_i^{\mathrm{longi/transv}}$ are shown. All components are perpendicular to each other such that the three components shown form a basis to fully characterize Br displacements. In **(b)** histograms for the norms $d^{\mathrm{longi/transv}} = \left|\delta \mathbf{r}^{\mathrm{longi/transv}}\right|$ of longitudinal and transversal displacements are shown. All histograms are normalized such that they resemble a density, i.e., their integral equals 1. *Reprinted with permission from [5], published under a CC BY 4.0 license.*

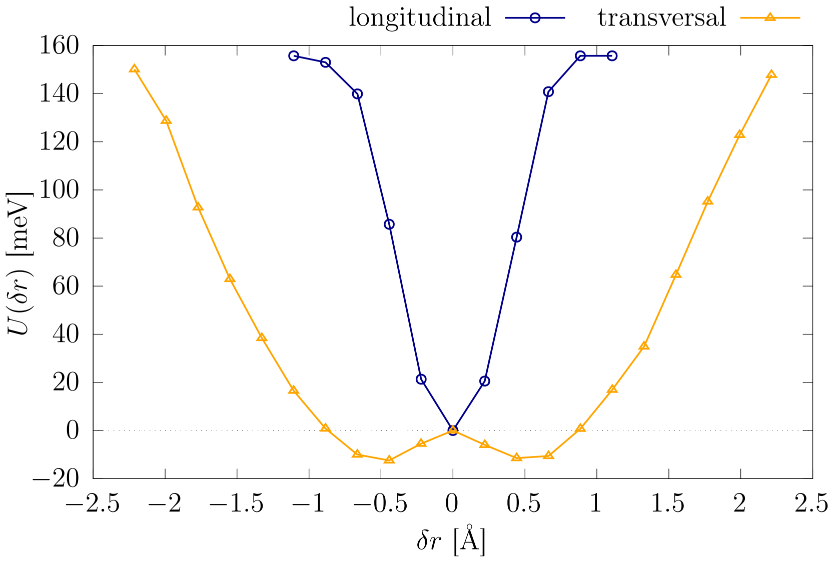

Figure 3.26.: Potential energy landscape, $U(\delta r)$, of the Br displacements obtained from an inversion of the Boltzmann distribution for one longitudinal and one transversal direction. *Reprinted with permission from [5], published under a CC BY 4.0 license.*

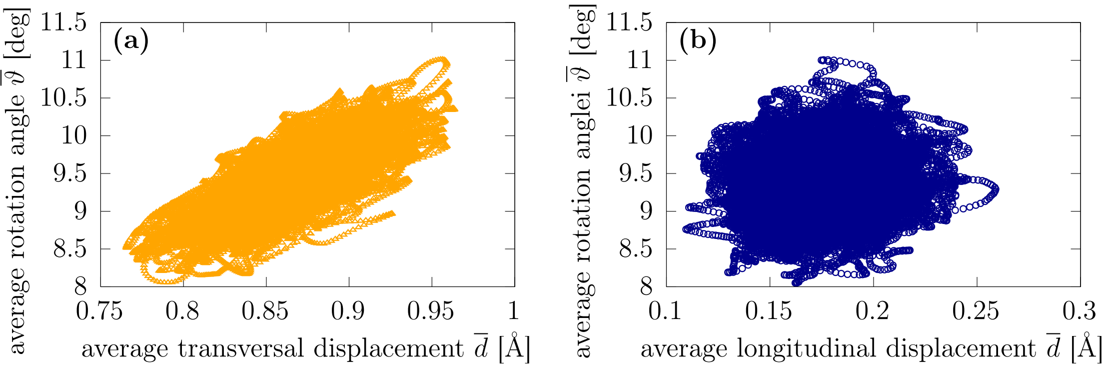

Figure 3.27.: Correlation between average octahedral rotation angle $\overline{\vartheta}$ (cf. fig. 3.28) and the average transversal (**(a)**) and longitudinal (**(b)**) Br displacements in $CsPbBr_3$. *Reprinted with permission from [5], published under a CC BY 4.0 license.*

are energetically much more expensive than transversal displacements. Moreover, a strongly anharmonic potential can be found for the transversal displacement which resembles the double-well potential found in literature for octahedral tilting and that was discussed earlier in section 3.3.

Finally, in fig. 3.27 the average ocathedral rotation angle (see fig. 3.28 for a definition of the angle) is shown as a function of the average transversal and longitudinal displacements, averaged over all Br atoms. While a correlation between transversal displacement and rotation angle can be seen in fig. 3.27a, no such correlation can be seen for longitudinal displacements in fig. 3.27b. Consequently, the transversal displacements can be correlated to octahedral tilting (see figs. 3.27 and 3.28) which is an established element of HaP dynamics [191–194]. In sum, the above findings establish a certain directionality in halide displacements. Here, however, implications of the directionality in halide motion on the resonant bonding and short disorder potential correlations, attributed to halide motion in section 3.6 above, shall be investigated.

In fig. 3.29, the correlation of the disorder potential according to eq. (2.120) is shown for several cases: only longitudinal Br displacements, only transversal Br displacements, and for the case of all possible atomic motion, according to thermal excitations at 425 K (full MD). From the correlations in fig. 3.29, it can be seen that the correlation length of the disorder potential induced by Br displacements transversal to the Pb-Br-Pb bonds is concurrent with the short-range correlation found for the dynamically shortened correlations from MD simulations, whereas the correlation in the disorder potential induced from longitudinal displacements of the Br atoms is more long-range. This suggests that the favorable properties of HaPs, namely short correlation length of the disorder potential and narrow band-edge energy distributions, are due to the structural flexibility of the halide atoms, i.e., their large transversality.

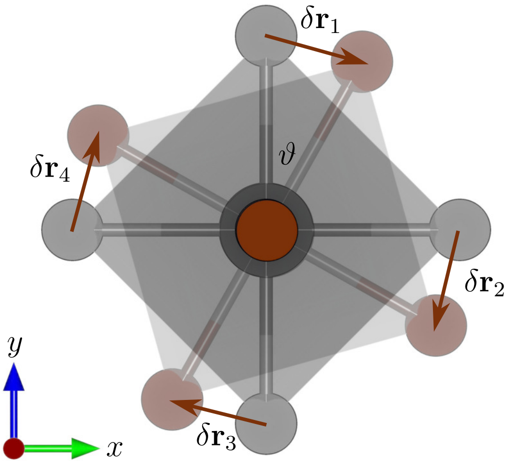

Figure 3.28.: Sketch to visualize the calculation of the octahedral rotation angle ϑ in the x-y plane. The rotation of an octahedron with respect to its reference is indicated by the two differently colored octahedra. The rotation angle can be calculated from the displacements of the four Br atoms as $\vartheta = \arcsin\left(\frac{1}{4d_{\text{Pb-Br}}}[\delta x_1 - \delta y_2 - \delta x_3 + \delta y_4]\right)$, where $d_{\text{Pb-Br}}$ is the Pb-Br distance. *Reprinted with permission from [5], published under a CC BY 4.0 license.*

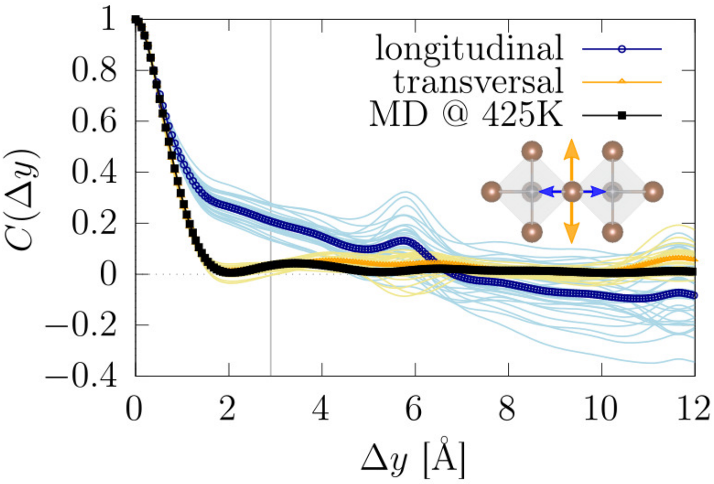

Figure 3.29.: Autocorrelation of the disorder potential for electronic states, calculated according to eq. (2.120). The thin curves show the autocorrelation functions for instantaneous snapshots of the three cases described below. The thick lines represent the averages of the instantaneous configurations. Shown are the correlation functions for three different cases: only longitudinal displacements of Br atoms are considered (blue), only transversal displacements of Br atoms are considered (orange), and all atomic motion at 425 K, according to a MD simulation, is considered (black). *Reprinted with permission from [5], published under a CC BY 4.0 license.*

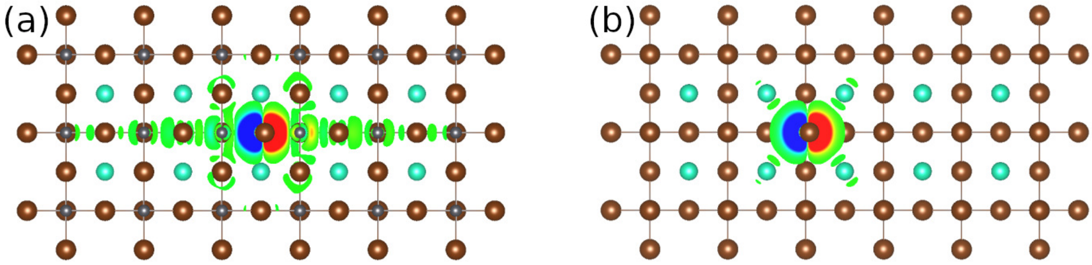

Figure 3.30.: Difference in the charge-density induced by displacing a single Br atom in **(a)** longitudinal and **(b)** transversal direction, visualized as an iso-surface plot, with an iso-surface of more than 8.1×10^{-3} $e\text{Å}^{-3}$. *Reprinted with permission from [5], published under a CC BY 4.0 license.*

Further, in order to understand the differences between longitudinal and transversal correlations, the response of the charge-density to atomic displacements is investigated fig. 3.30a and fig. 3.30b. The results can be explained as follows: the valence band of $CsPbBr_3$ is formed by a σ interaction between Br p-orbitals and Pb s-orbitals [195, 196], which form the resonant network explained in section 3.5. A longitudinal Br displacement thus perturbs the orbital overlap, lifting the degeneracy of the resonant $sp\sigma$-bonds, and results in a long-range change of the charge-density, as can be seen in fig. 3.30a. However, a transversal displacement is, by definition, perpendicular to the $sp\sigma$-bonds and therefore has a much smaller influence on the network of resonant bonds. For this reason changes in the charge-density, induced by a transversal Br displacement, are much more localized, i.e., short-range in nature. This can be seen fig. 3.30b.

These differences between longitudinal and transversal displacements are expected to also impact optical absorption. Consequently, fig. 3.31 shows the JDOS for longitudinal and transversal Br displacements. The result resembles the findings in fig. 3.22 remarkably well. In other words, while the JDOS calculated for instantaneous configurations with longitudinal Br displacements only in fig. 3.31 still behaves as the static case in fig. 3.22, it is the emergence of transversal Br displacements which leads to the rapid rise found for the MD case in fig. 3.22.

We thus conclude that the favorable band-edge distributions and short-range correlations of the disorder potential in HaPs are a consequence of the perovskite structure and the dynamic flexibility coming along with this geometry, i.e., the transversality of Br displacements. This hypothesis will next be further tested by a comparison of the case of HaPs to a material with a similar degree of anharmonicity and bonding mechanism, but a substantially different crystal structure.

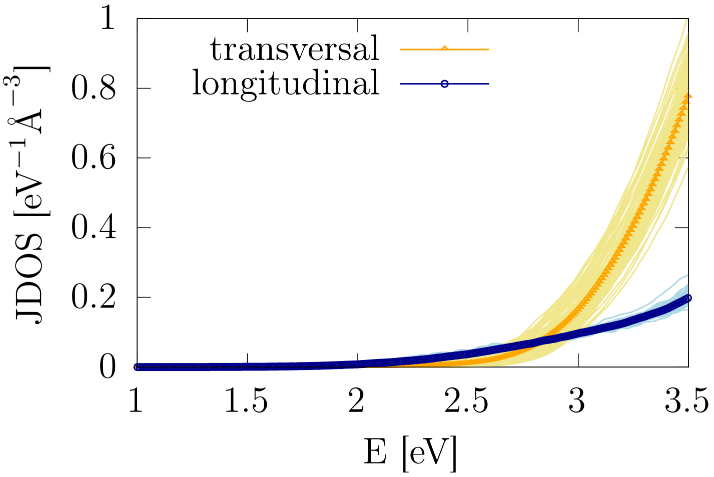

Figure 3.31.: JDOS of $CsPbBr_3$ for two different cases. The thin curves show the JDOS for instantaneous snapshots of the two different scenarios described below. The thick lines represent the averages of the instantaneous configurations. Shown is the JDOS for the cases: only longitudinal displacements of Br atoms are considered (blue) and only transversal displacements of Br atoms are considered (orange). *Reprinted with permission from [5], published under a CC BY 4.0 license.*

3.8. Comparison to PbTe

PbTe is a paradigmatic thermoelectric material with a rocksalt crystal structure (fig. 3.32), a low band gap, and a high thermoelectric figure of merit, i.e., a high efficiency in converting heat into electrical energy [197–202]. PbTe is a compelling counter-example to $CsPbBr_3$ as both materials share some important characteristics while they differ in others. Among their similarities are their vibrational and bonding properties. Both materials exhibit low phonon energies, i.e., lower than approximately 4 THz and 5 THz for PbTe and $CsPbBr_3$, respectively, see fig. 3.13, fig. 3.16, fig. 3.33, and the summary in table 3.2 [2, 203–205]. Figure 3.33 shows the VDOS of PbTe as obtained from harmonic calculations using finite displacements (black line) as well as the VDOS obtained from MD simulations by means of the VACF (green curve). The VDOS demonstrates the low vibrational frequencies reported above for both, a harmonic and an anharmonic treatment of lattice dynamics. Second, the differences between a harmonic and an anharmonic treatment can be seen by comparing the black line with the green curve. Anharmonicity is important in both PbTe [182, 206–208] and HaPs [21, 22, 24, 26, 144–146, 156, 158, 209], which is the second similarity both materials share for their vibrational properties. This can, e.g., also be seen in their low phonon lifetimes of less than 10 ps in both, PbTe and HaPs (see table 3.2 and references there). The important role of anharmonicity has been attributed to the bonding mechanism in both materials, which also is very similar as discussed below and summarized in table 3.2. In particular, resonant bonding can be found and related to anharmonicity in PbTe [182] and HaPs [2, 158,

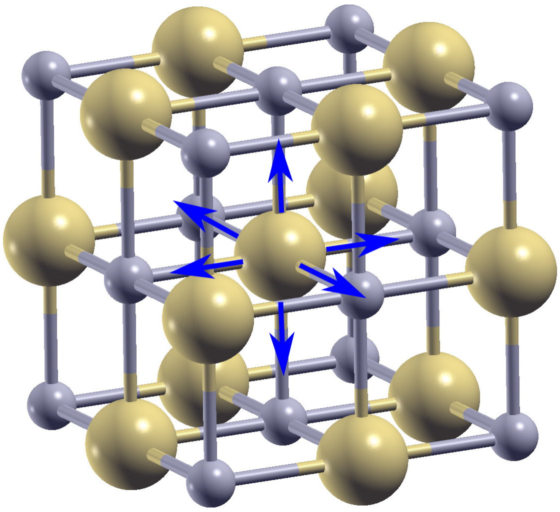

Figure 3.32.: Crystal structure of PbTe (gray: Pb, yellow: Te). In contrast to the halide ions in HaPs, Te exhibits three *longitudinal* directions (indicated by blue arrows). The atomic structure was visualized using the xCrysden program [215].

181] (see also section 3.5). In both materials, the valence band is anti-bonding and formed by a σ interaction of Pb s-orbitals with Te and halide p-orbitals, respectively [197, 210, 211]. The conduction band, on the other hand, is predominantly formed by Pb p-orbitals in both materials, with σ interactions dominating in PbTe and π character arising in HaPs due to their different crystal structures [197, 210, 211]. Finally, the hybridization of Pb s-orbitals and Te/halide p-orbitals results in a stereochemically active lone pair of electrons in both compounds [212–214]. Hence, these characteristics render PbTe an interesting material for comparison when it comes to properties that are suggested to depend on (anharmonic) structural dynamics and resonant bonding.

On the other hand, there are also important differences between PbTe and HaPs rendering the comparison of both materials even more interesting. First of all, the most obvious contrast is the difference in the crystal structure between both materials, see figs. 3.24 and 3.32. Although both materials share their bonding mechanism, PbTe crystallizes in a rocksalt structure whereas HaPs show the perovskite structure. As a consequence the structures show the same coordination for the Pb atoms in both compounds, however the coordination of Te is higher than that of the halides (Br in $CsPbBr_3$). Therefore, PbTe has three longitudinal directions (indicated by blue arrows in fig. 3.32), i.e., directions parallel to Pb-Te-Pb bonds, but no direction perpendicular to the Pb-Te-Pb bonds, that is, no transversal direction. This is in contrast to the case of HaPs which have only one longitudinal, but two transversal directions. Following our discussion in the previous sections, we assume this difference to be crucial for the structural flexibility and its impact on disorder-potential correlations and band-edge distributions.

Closely related to band-edge distributions is the Urbach energy, providing the steepness of the absorption coefficient close to the onset of optical absorption, as discussed

Table 3.2.: Comparison of several properties between the two materials PbTe and $CsPbBr_3$. *Reprinted with permission from [5], published under a CC BY 4.0 license.*

	PbTe	$CsPbBr_3$
crystal structure	rocksalt	perovskite
phonon frequencies	$\lesssim 4$ THz[+] [204, 205]	$\lesssim 5$ THz [2, 203]
anharmonic	✓	✓
phonon lifetimes	< 10 ps [216]	< 10 ps [2, 27]
resonant bonding	✓	✓
VBM character	σ^*	σ^*
CBM character	σ^*	$\sigma^*\pi^*\pi^*$
band gap	~ 0.32 eV [217–220]	2.25 - 2.38 eV[§] [151, 221–224]
Urbach energy	~ 56 meV[†] [220]	$\sim$15 meV[‡] [127–131, 225]

[+] see also fig. 3.33

[§] depending on structural phase, temperature and method

[†] nanocrystalline, not single crystalline

[‡] most for $MAPbI_3$, only [225] for $CsPbBr_3$

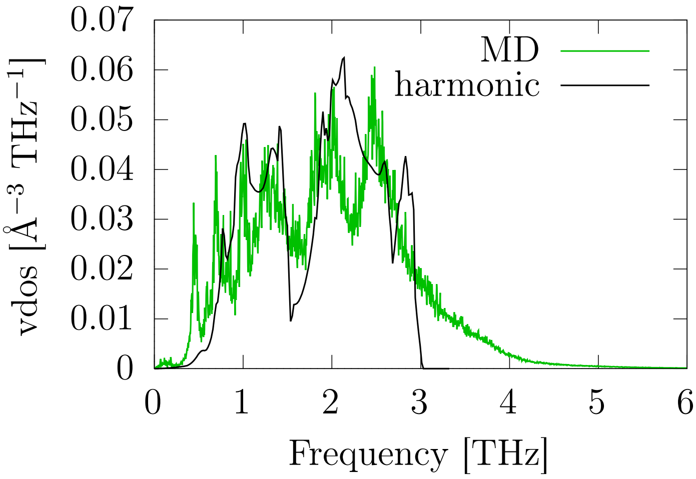

Figure 3.33.: Harmonic (black) and anharmonic (green) VDOS of rocksalt PbTe. The anharmonic VDOS has been obtained from the VACF calculated from MD at 425 K. *Reprinted with permission from [5], published under a CC BY 4.0 license.*

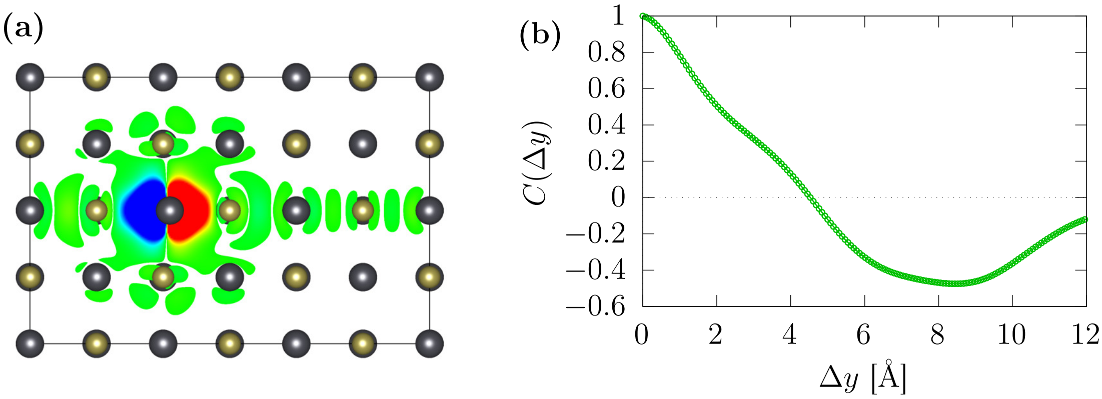

Figure 3.34.: **(a)** Difference in the charge-density induced by displacing a single Pb atom, visualized as an iso-surface plot (iso-level = 8.1×10^{-3} eÅ^{-3}). *Reprinted with permission from [5], published under a CC BY 4.0 license.* **(b)** Autocorrelation of the disorder potential for electronic states, calculated according to eq. (2.120).

in sections 2.5 and 3.6. For sharp optical absorption edges and thus efficient solar absorption in thin-film devices, small Urbach energies are demanded, which requires narrow band-edge distributions. Indeed, small Urbach energies have been measured for HaPs, with Urbach energies of about 15 meV about room temperature reported for the paradigmatic $MAPbI_3$ [127–131] ($\lesssim$19 meV in $CsPbBr_3$ [225]). In contrast, PbTe is not known as an efficient solar absorber and features higher Urbach energies of 56 meV in nanocrystalline PbTe [220].

Further differences include the electronic structure. PbTe exhibits a comparatively small direct band-gap (around 0.32 eV) at the L-point of the Brillouin zone [217–220]. Several prototypical HaPs, on the other hand, as discussed in section 3.1 exhibit a direct band gap at the R-point of the Brillouin zone when in the cubic phase. Their band gap is much larger than that of PbTe, and it is tunable by ionic composition. For instance, the band gap of $CsPbBr_3$ is measured to be 2.25 - 2.38 eV, with the spread in the reported values resulting from different structural phases, temperatures, and methods [151, 222–224].

The focus here, however, is on comparing the material to the findings discussed in sections 3.5 and 3.6 for HaPs to further test the importance of transversal motion hypothesized in section 3.7. In fig. 3.34a, the response of the charge density to the displacement of a single Pb atoms is shown, similar to fig. 3.19 in section 3.5. This response is found to be long range, in accordance with our expectations based on the knowledge that PbTe and HaPs exhibit similar bonding mechanisms for their ideal structures. Consequently, the correlation of the disorder potential, shown in fig. 3.34b, also is long range, easily exceeding the 6.56 Å of the lattice constant of the conventional unit cell. Thus our findings for the charge density response are similar to our findings in fig. 3.19, section 3.5. Particularly, we establish that we indeed find a (static) long-range response of the material, similar to the findings for HaPs.

For HaPs, dynamic effects have shown to dynamically shorten the correlation length of the disorder potential and narrow band-edge distributions (section 3.6). Therefore, the behavior of PbTe has been examined with calculations including structural dynamics by means of MD simulations. In fig. 3.35a the correlation of the disorder potential calculated for instantaneous snapshots from MD at 425 K is shown. Remarkably, the correlation remains long ranged, in particular when compared to the case of $CsPbBr_3$, since it goes far beyond unit cell size and the Pb-Te nearest-neighbor distance. A second remarkable feature of the disorder potential correlation in PbTe, are the oscillations that can be seen in fig. 3.35a. These oscillations can be attributed to the periodic crystal potential which is modulated by the thermal noise. For further details, see the toy model in appendix B.

Finally, the relative widths of the VBM and CBM distributions of PbTe and $CsPbBr_3$ are compared in fig. 3.35b. There, we find that the relative band-edge distributions of PbTe are much wider than those of $CsPbBr_3$ which is in agreement with the expectations from (i) literature results on the Urbach tail, namely a larger Urbach energy in PbTe compared to HaPs (cf. table 3.2) coincides with larger distributions in fig. 3.35b. And (ii), as discussed already before in section 3.6, a broader band-edge distribution is concomitant with a longer correlation length in the disorder potential.

In summary, a comparison of $CsPbBr_3$ to PbTe supports the notion of attributing important characteristics of the HaPs, such as short-range correlated disorder potentials, narrow band-edge distributions, and consequently small Urbach energies and sharp optical absorption edges, to the structural flexibility of the perovskite structure. More precisely, the structural flexibility of HaPs manifests in large transversal motion of the halide atoms which is preferred over longitudinal displacements and cannot be found in PbTe.

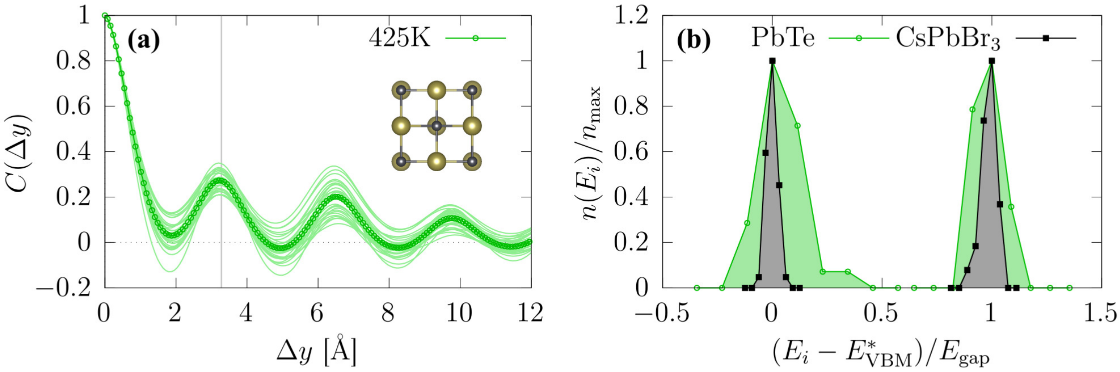

Figure 3.35.: **(a)** Autocorrelation of the disorder potential for electronic states in PbTe as obtained from MD simulations. **(b)** Band-edge energy distributions for PbTe (green curve) and CsPbBr$_3$ (black curve) as obtained from MD simulations at 425 K. The histograms are normalized by the highest occurrences $n_{\max} = n(E^*_{\mathrm{VBM/CBM}})$ for VBM and CBM, respectively. The nominal band gap $E^*_{\mathrm{gap}} = E^*_{\mathrm{CBM}} - E^*_{\mathrm{VBM}}$ is given by the difference between the VBM/CBM energies with the highest occurrence, $E^*_{\mathrm{VBM/CBM}}$. *Reprinted with permission from [5], published under a CC BY 4.0 license.*

4. Results and discussion: superionic α-AgI

4.1. Introduction to solid-state ion conductors and silver iodide

The application of energy materials with intriguing structural dynamics is not restricted to photovoltaics only. Energy storage systems, in particular batteries, are also driven by the usage of promising new materials. One such candidate for improvement in battery research are solid-state electrolytes, which could potentially replace liquid electrolytes [32]. Solid-state electrolytes are usually nonflammable [226] and thus they improve safety of batteries, the longevity of batteries [227, 228] and they enable higher energy densities [226]. In electrolytes - in liquid as well as solid-state - electrical current is conducted by diffusing ions. Thus we call solid materials, e.g., crystalline materials, glasses, polymers, or nano-composites [229], used as electrolytes *solid-state ion conductors (SSICs)*. The applications of SSICs further span fuel cells, supercapacitors, sensors, and filters [229–232]. Crucial for all these applications is a high electric conductivity, which is often hindered by low ion diffusion [233]. As a consequence, SSIC research is driven by understanding and predicting highly conductive SSIC materials, and by the search for well-founded descriptors of “good” ion conduction.

In accordance with the scope of this work, we will discuss the role of lattice dynamics for ionic conductivity. Lattice dynamics studies on ion conductors have been done for decades, see, e.g., refs. [84, 234–238] for MD studies on the SSIC α-AgI. Consequently, lattice dynamics have been suggested as descriptors for SSICs [227, 239–242] and even for being used in high throughput studies [227]. However, simple approaches, for instance correlating the softness of the lattice (low phonon frequencies) with the activation energy for ionic transport [239–242], have been shown to break down at some point [243, 244]. But ion diffusion is a structural dynamic process, and it can be shown that exciting as little as only about 10 % of the vibrational modes in Ge-substituted Li_3PO_4 ($Li_{3.042}Ge_{0.042}P_{0.958}O_4$) can drastically increase ion diffusion [233]. This motivates studies towards a more fundamental understanding of lattice dynamics in SSICs. This understanding has to include anharmonicity and, strongly connected to this, relaxational motion as discussed in section 2.3.5, two aspects which have often been neglected in traditional models. As sketched in fig. 4.1, diffusing ions (green arrow) have to overcome the saddle point area in the potential

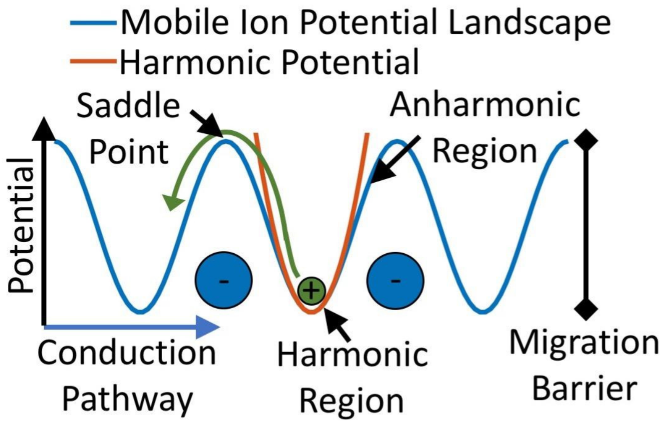

Figure 4.1.: Sketch of the potential energy landscape for ion diffusion, comparing the harmonic region and the anharmonic region close to the saddle point. *Reprinted with permission from [3]. Copyright (2020) by the American Physical Society.*

energy landscape (blue curve) during ionic hopping. This region is clearly outside the range where a harmonic model (orange curve) is valid, thus anharmonicity is inherent to ion diffusion [3, 245–248]. In traditional models, however, the harmonic approximation has been used to estimate hopping frequencies and anharmonicity has at most been described phenomenologically [32, 245–249]. Our approach is to include anharmonicity and relaxational motion by means of combining Raman spectroscopy, conducted by our experimental collaborators and MD simulations, for the paradigmatic SSIC α-AgI.

The high-temperature phase of silver iodide, α-AgI, is one of the seemingly simplest and most extensively studied ion conductors. Structural phase transitions, and consequently the ion diffusivity, of silver iodide are temperature and pressure dependent. There are two phases stable only at high pressure, whereas the three phases mentioned below are (meta-)stable at ambient pressure [250]. At low temperatures – including room temperature – β-AgI, exhibiting a wurtzite structure, is the most stable phase. In this phase, AgI is not a SSIC, however it is famous for its application in cloud seeding. This weather modification, e.g., allows to prevent damage by hail using β-AgI to initiate freezing of water within the cloud, see, e.g., reference [251]. In the same temperature range, the meta-stable γ-phase coexists with β-AgI [250]. This phase crystallizes in a zinc blende structure, however it is not ion conductive, either. The most interesting phase, in our context, is the high temperature phase α-AgI. This phase is stable above approximately 420 K [3, 250, 252] and exhibits a high ionic conductivity due to diffusing silver ions [234, 252]. In this structural phase, the iodide ions crystallize into a BCC lattice, with the silver ions distributed over tetrahedral sites (see fig. 4.2) [237, 250, 253–257]. As there are more tetrahedral sites than Ag atoms, the Ag atoms are distributed across and moving in between the sites, finally breaking translational symmetry. An alternative way to interpret the structure of α-AgI, is to consider it as a space filling arrangement of XI_4 tetrahedra, with X either an empty tetrahedral site or an Ag cation

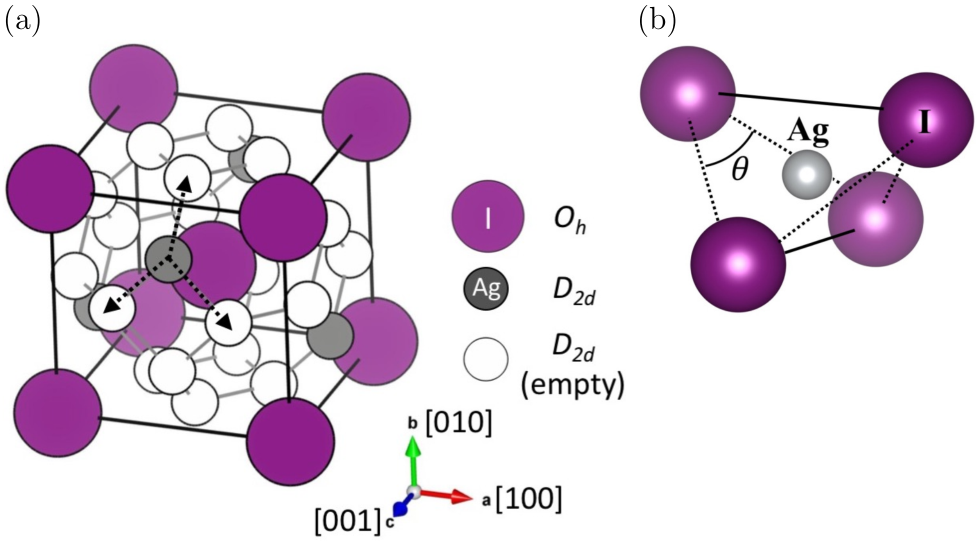

Figure 4.2.: Structural representations of α-AgI. **(a)** Crystal structure of α-AgI. Iodine anions (purple) are positioned at BCC positions. Ag cations (gray) are distributed over tetrahedral sites (empty sites: white). Ag diffusion between tetrahedral sites is indicated by the black arrows. The crystal structure of α-AgI can also be represented by space filling AgI_4 tetrahedra. **(b)** AgI_4 tetrahedron. *Reprinted with permission from [3]. Copyright (2020) by the American Physical Society.*

(fig. 4.2b). In this more localized picture, Ag is diffusing between tetrahedra which can either be empty or occupied. In our recent work on the lattice dynamics on α-AgI, our experimental collaborators convincingly show that this local tetrahedral picture explains the Raman spectrum much more accurately than models based on the (average) crystal structure [3].

Below, we discuss the lattice dynamics of α-AgI by means of Raman spectroscopy experiments and theoretical MD simulations. In particular, we identify important roles of anharmonicity for the iodine host lattice as well as the mobile Ag ions. Moreover, using a set of theoretical *gedankenexperiments* we establish a link between the host lattice dynamics and ion diffusion, with host lattice dynamics facilitating ion diffusion. We therefore suggest (anharmonic) host lattice dynamics, which can for instance be observed as a central peak in Raman spectra, as a descriptor for high ionic conductivity in SSIC materials.

4.2. VDOS and Raman spectrum of superionic α-AgI

Note that parts of the results presented in sections 4.2 to 4.4 are published in reference [3].

As introduced above, the second important field of energy materials, we discuss in this work, are SSICs, as used for instance as solid electrolytes in all solid-state batteries. Their name - *ion conductor* - already highlights one of their hallmark properties, i.e., their electric conductivity that is dominated by the (diffusive) motion of ions. This ion diffusion is an inherently anharmonic motion, already because there is no long term average position $\mathbf{R}_0$ the ion could fluctuate around in a harmonic potential. An illustration of a simplified picture of the potential energy landscape has been discussed above in the context of fig. 4.1. In a traditional description of ion diffusion, the ion is harmonically vibrating until it reaches the saddle point area, which it finally overcomes [32, 245–249]. The attempt frequency for overcoming the migration barrier is estimated from the harmonic frequency. However, naturally this description is neglecting all effects of anharmonicity going beyond the ion diffusion. Such effects may arise in the saddle point region and, moreover, might even be present for the *host lattice* of SSICs , i.e., the lattice formed by the ion species that are not diffusing. This host lattice is traditionally assumed to fulfill the harmonic approximation [245]. However Raman spectroscopy of super-ionic α-AgI reveals traces of anharmonicity besides the signature of ion diffusion. Experimental measurements of Raman spectra, an example spectrum can be seen in fig. 4.3, exhibit a *central peak* [3, 250, 258, 259], a clear signature of anharmonicity. A central peak denotes a Raman peak at zero frequency, and as in a harmonic picture $\omega = \sqrt{f/m}$, this would imply an atomic motion without restoring force f, a *relaxational motion*. Obviously, ion diffusion resembles such an atomic motion and has been identified to cause a central peak in the Raman spectrum. However, ion diffusion is not required to observe a central peak in Raman spectra - for instance a central peak has also been observed for anharmonic HaPs [24, 260, 261], oxide perovskites [262–267], and other materials [268–272]. In the case of α-AgI, previous work identified one very narrow central peak caused by the diffusing silver atoms, which however is too narrow to be resolved in fig. 4.3 [259, 273]. On top, there is a second relaxational motion, resulting in a broader central peak whose origin has not yet been identified [3, 259] and which is visible in the experimental Raman spectrum in fig. 4.3.

A more detailed experimental study using polarization-orientation (PO) Raman measurements further reveals that the central peak of fig. 4.3 exhibits a symmetry [3] (see discussion of fig. 4.4 below). As discussed in appendix C, in addition to “normal” Raman measurements, PO Raman measurements further observe the angular dependency of the outgoing light to learn about the symmetry of the underlying Raman active phonon modes. For further information on the experimental part, we would like to refer to the paper by Brenner et al. [3] accompanying our combined experimental-theoretical study.

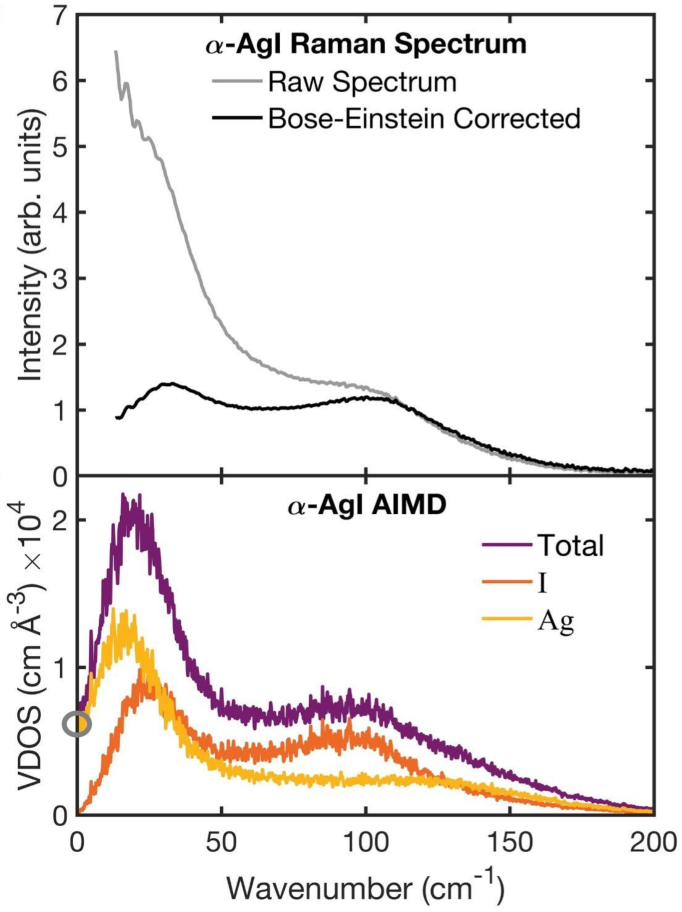

Figure 4.3.: Vibrational spectra of α-AgI at finite temperature. **Top:** Experimentally measured Raman spectrum at 443 K. The raw data are shown in gray, the Bose-Einstein corrected spectrum is shown in black. **Bottom:** VDOS of α-AgI obtained from first-principles MD at 500 K. The full VDOS is shown in purple, contributions from I and Ag ions in orange and yellow, respectively. The gray circle highlights the zero-frequency component of the VDOS, providing a diffusion constant $D = 3.1 \times 10^{-5}$ cm^2/s for Ag diffusion. *Reprinted with permission from [3]. Copyright (2020) by the American Physical Society.*

We would like to start our discussion of structural dynamics in α-AgI and its implications for functional properties by revisiting the crystal structure, fig. 4.2. It comprises a BCC iodine host lattice and a silver sublattice. However, the distribution of silver atoms is ambiguous, as the two silver atoms per unit cell populate two out of twelve tetrahedral sites in the unit cell [237, 250, 253–257], with empty sites sketched in white in fig. 4.2. Between these sites, silver atoms can hop, i.e., diffuse. As a consequence silver atoms are distributed at finite temperature and there is no unique reference structure. Moreover, translational invariance is broken by the silver atoms, introducing a form of disorder. Subsequently, the symmetry of the material is shortened to below the unit cell range, which will be important for understanding PO Raman spectra as we will discuss below. On top, not having a reference structure makes it unfeasible for us to start describing the structural dynamics of this material by harmonic phonon calculations as we have done for the HaPs (sections 3.2 and 3.3). Instead, we will directly start from first-principles MD simulations.

The VDOS as obtained from MD, using the VACF as explained in section 2.4.2, can be seen in fig. 4.3. The VDOS in fig. 4.3 resembles the experimentally measured Raman spectrum shown in the same figure remarkably well. This is peculiar since the Raman spectrum only samples vibrational modes at the Γ-point of the Brillouin zone of a crystalline material (cf. section 2.3.4) which is a direct consequence of the comparatively small momentum of photons. The momentum of a photon with wave vector $\mathbf{k}$ is given by

$$\mathbf{p}_k = \hbar \mathbf{k} \ , \tag{4.1}$$

and its magnitude is determined by the photon energy

$$E_k = \hbar \omega_k = \hbar c k \ , \tag{4.2}$$

with $k = |\mathbf{k}|$ the absolute value of $\mathbf{k}$ and c the speed of light. Similar expressions also hold for a phonon with wave vector $\mathbf{q}$,

$$\mathbf{p}_q = \hbar \mathbf{q} \tag{4.3}$$

and

$$E_q = \hbar \omega_q = \hbar c_s q \ , \tag{4.4}$$

with $c_s = \omega_q / q$ the phase velocity of the phonon mode (the speed of sound in case of acoustic modes). Due to energy conservation, the change in the energy between incident light and scattered light has to be similar to the energy of the involved phonon that scatters the light, i.e.,

$$\Delta E_k = \hbar \Delta \omega_k = \hbar c \Delta k = E_q \ . \tag{4.5}$$

But momentum conservation also implies

$$\hbar \Delta \mathbf{k} = \hbar \mathbf{q} \ . \tag{4.6}$$

From eqs. (4.5) and (4.6) we get

$$\hbar c_s q = \hbar c \Delta k \ . \tag{4.7}$$

But since $c \gg c_s$, eqs. (4.6) and (4.7) can only hold at the same time when

$$\Delta k \approx q \approx 0 \ , \tag{4.8}$$

i.e., only phonons close to the Γ-point ($\mathbf{q} = 0$) can be measured with photons. For photons in the visible range ($E \approx 2$ eV) the change in reciprocal vector can be estimated to $\Delta k = \Delta E_k / \hbar c \approx 10^{-3}$ Å^{-1}, which indeed is much smaller than the typical dimension of the first Brillouin zone (~ 1 Å^{-1}) [36, 39].

An alternative picture in real space can be obtained considering the much longer wave length of light than the size of a typical unit cell. Therefore only vibrational motion with long wave lengths, i.e., atoms vibrating in phase in several unit cells, are expected to be probed in Raman spectroscopy. But the long wave-length limit is the $q \to 0$ limit. Thus, also this picture provides that only phonons close to Γ can be probed in such experiments.

According to the above pictures and reasoning, only a small fraction of the VDOS should be represented in the Raman spectrum. However in fig. 4.3, the theoretically obtained VDOS resembles the experimentally measured Raman spectrum remarkably well. This can be explained by a breaking of the translational symmetry: The Γ-point is defined as the center of the Brillouin zone, the "unit cell" in reciprocal space. However, as the unit cell dimensions, for instance the volume $V_{\rm UC}$ of the unit cell, increase in real space, the dimensions in reciprocal space, as represented here by the volume of the first Brillouin zone in reciprocal space decrease

$$V_{\rm BZ} = \frac{(2\pi)^3}{V_{\rm UC}} \ . \tag{4.9}$$

In the extreme case of total absence of translational symmetry, the lattice dimensions of the "unit cell" in real space go to infinity (there is no repeated motif), and thus the reciprocal lattice dimensions go to 0, i.e., they collapse to a single point, the Γ-point. Thus, with increasing disorder, i.e., increasing breaking of translational symmetry, an increasing fraction of vibrational excitations are represented at the Γ-point. Consequently, the VDOS, sampling all vibrations within the complete first Brillouin zone, and the Raman spectrum, only sampling vibrations at the Γ-point, become more and more similar. Therefore, our comparison in fig. 4.3 establishes the notion of broken translational symmetry, thus the experiment is sampling phonons at the Γ-point of an effectively larger "unit cell" spanning a larger fraction of the sample.

Having established the broken translational symmetry in α-AgI, we can now analyze the vibrational properties in more detail. In both, theory and experiment, two broad features at approximately 40 cm^{-1} and 100 cm^{-1} respectively are found. A detailed analysis of the PO Raman spectra reveals three underlying modes at 37.7 cm^{-1}, 102.2 cm^{-1}, and 106.4 cm^{-1} (cf. fig. 4.4b and table 4.1) [3]. A fourth feature is the experimentally detected central peak. According to literature, there should be two contributions to the central peak, with the narrower being caused by silver diffusion [259, 273]. In our theoretical VDOS silver diffusion can be seen by the

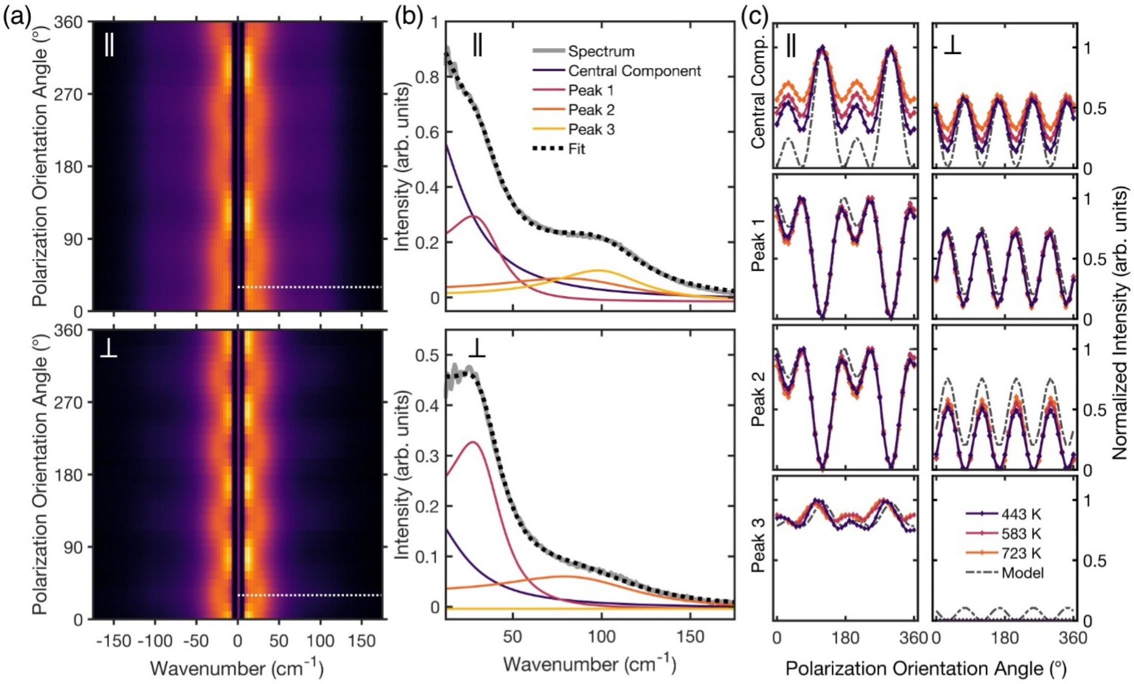

Figure 4.4.: PO Raman spectra of α-AgI. **(a)** Angle dependent Raman intensities for parallel (∥, top) and perpendicular (⊥, bottom) polarization. **(b)** Example Raman spectra for both polarizations at fixed angle (dashed lines in panel (a)), decomposed into its contributions as obtained from a fit according to the “local tetrahedral model”. **(c)** Angle dependence of the four components of the Raman spectrum at three different temperatures, compared to the expectation from the “local tetrahedral model”. *Reprinted with permission from [3]. Copyright (2020) by the American Physical Society.*

non-zero VDOS at zero frequency, see fig. 4.3. The decomposition of the theoretical VDOS into atomic contributions in fig. 4.3 confirms that this is solely due to silver. Besides the difference at zero frequency, the decomposition into atomic contributions reveals that both, Ag and I, show similar frequency ranges. From the zero frequency VDOS the diffusion constant D can be obtained with eq. (2.108) to obtain $D = 3.1 \times 10^{-5}\text{cm}^2/\text{s}$, which is in excellent agreement with literature values [234, 252] and with the diffusion constant obtained from a fit of the MSD (cf. eq. (2.103); fig. 4.6). Nonetheless, due to experimental limitations, the contribution of silver diffusion to the Raman spectrum should not be resolved in the experimental Raman spectrum shown in fig. 4.3. Therefore, the central peak in the Raman spectra of our experimental collaborators (figs. 4.3 and 4.4) has to be caused by a different relaxational motion.

Moreover, the PO dependence of the Raman intensity of the measured central peak reveals an underlying symmetry of this peak (fig. 4.4). Similar, the PO analysis of the three finite frequency components shown in fig. 4.4 reveals underlying symmetries. Figure 4.4 shows the PO Raman intensities measured experimentally. In

Table 4.1.: Raman modes and their symmetries as predicted from both, the average space group of α-AgI and the "local tetrahedral model" (LTM), as well as the frequencies and widths obtained from fitting the experimentally measured spectrum at 442 K (cf. fig. 4.4). *Reprinted with permission from [3]. Copyright (2020) by the American Physical Society.*

Component	Space group	LTM	Frequency (cm^{-1})	Width (cm^{-1})
Central component	E_g	$A_1 + B_1$	0	23.0
Peak 1	T_{2g}	$B_2 + E$	37.7	37.0
Peak 2	-	$B_2 + E$	102.2	95.7
Peak 3	-	A_1	106.4	61.4

panel (a), the intensity is shown as a function of both the PO angle θ (see fig. C1 in section 2.3.4) and frequency for parallel and perpendicular polarized light. A representative spectrum at constant PO angle is shown in fig. 4.4b (the angle is indicated by the dashed line in panel (a)). From this spectrum at constant angle, the four components discussed above can be identified. The angular dependence of each of the four components can be observed in the modulation of the spectrum in fig. 4.4a and, in particular, in fig. 4.4c. Figure 4.4c shows the Raman spectrum as a function of the PO angle for each of the four components individually (this can be understood as a vertical line in fig. 4.4a, i.e., a line with constant frequency). At the bottom line, the main features of the PO measurements can be summarized to reveal four Raman active components, each showing a PO angle dependence.

All of these PO findings are difficult to rationalize by using a traditional picture. The space group of the time-averaged crystal structure ($Im\bar{3}m$) only predicts two Raman active phonon modes of symmetries E_g and T_{2g}, respectively, see table 4.1. On the other hand, the spectrum cannot be explained by disorder induced Raman scattering, either. Disorder induced Raman scattering, as observed in other materials with broken translational symmetry, e.g., amorphous crystals or liquids, is expected not to show any PO angle dependence at all [3]. This is also shown in fig. A2, where the PO Raman measurements of liquid $CHCl_3$ at room temperature are shown. As discussed here, the Raman spectrum of this fluid has no PO angle dependence, although showing a central peak. In conclusion, established pictures predict either two Raman active modes with PO dependence or no PO dependence at all, in contrast with the four features with PO dependence experimentally measured.

4.3. Iodine host-lattice anharmonicity in superionic α-AgI

In order to identify the origins of this "liquid-crystal conundrum" and the relaxational motion that results in the central peak, we thus study the I-I-I bond angle θ (defined in fig. 4.2), see fig. 4.5 (all 12 angles are shown in figs. A3 and A4).

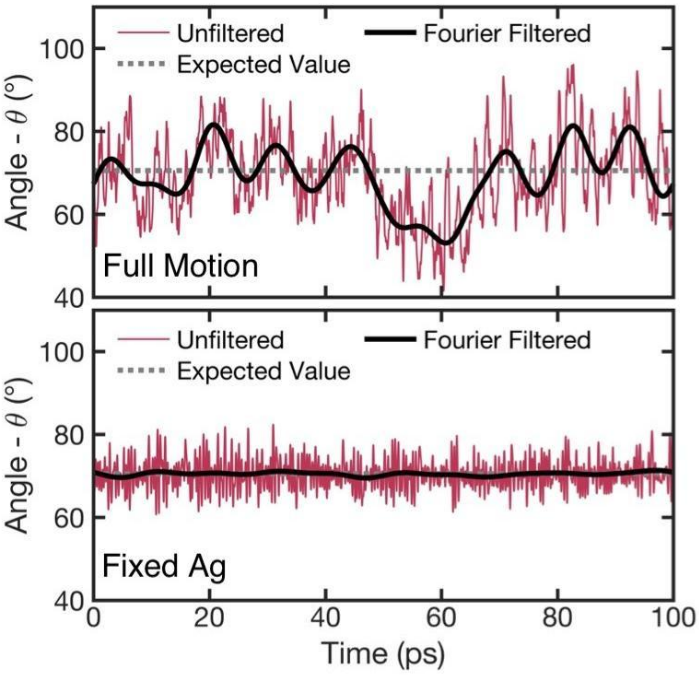

Figure 4.5.: Trajectories of the angle θ as obtained from MD simulations at 500 K. The unfiltered trajectories are shown in red, the black lines show the trajectories filtered with a Fourier filter. The expectation values are indicated by the gray horizontal lines. **Top:** unfiltered and Fourier filtered trajectory of θ as obtained from a fully unconstrained MD simulation. **Bottom:** unfiltered and Fourier filtered trajectory of θ as obtained from a MD simulation with Ag ions fixed to BCC positions. *Reprinted with permission from [3]. Copyright (2020) by the American Physical Society.*

In fig. 4.5 we show the trajectories of θ as obtained from MD simulations. The full trajectory (red line) shows significant temporal deviations from $\theta = 70.5°$ and $\theta = 54.75°$ for the large and the small angles of the tetrahedra, respectively, which are expected for the tetraheda in the ideal BCC structure. These deviation further seem to appear even at longer timescales. To distinguish slow motion and thus low frequency fluctuations from expected high frequency fluctuations, we filtered the trajectories for low frequencies. The solid black lines in fig. 4.5 show only contributions to the angular trajectories with frequencies below 5 cm^{-1} (see section 2.6.2 for details on the FFT-filter method). Importantly, also the FFT-filtered angular trajectories show long lasting, large deviations from the expected angles, suggesting that the low frequency relaxational motion observed in Raman spectroscopy can be related to iodine host lattice motion.

Remarkably, this suggests that the "crystal-liquid conundrum" can be resolved by introducing a *local tetrahedral oscillator model.* As discussed before, the relaxational motion we observe, independent whether it is due to ion diffusion or any other process, breaks translational symmetry. As a consequence, lattice vibrations localize to motifs below unit cell size and, thus, the symmetry observed in the PO data is established locally, rather than through long-range order. One natural motif is given by the AgI_4 tetrahedron sketched in fig. 4.2b. The point group of one such local tetrahedron (D_{2d}) predicts Raman modes of symmetries $2A_1 + B_1 + 2B_2 + 2E$. And thus, as table 4.1 reveals, the point group of the local AgI_4 tetrahedra can indeed correctly predict the PO spectrum. Interestingly, the local tetrahedral oscillator model is also capable of explaining the symmetry of the central peak as part of the eigenmodes of a D_{2d} tetrahedron. As discussed in section 2.3.5, and in particular demonstrated in fig. 2.6, a central peak Raman feature can result from an overdamping of a normal mode. It thus appears that the Raman spectrum of α-AgI can be rationalized by a local tetrahedral model and the central peak arises from an overdamped normal mode of the AgI_4 tetrahedron. Notably, this suggest that also the iodine host-lattice undergoes a relaxational motion.

4.4. Interplay of host-lattice dynamics and ion diffusion

Provided with this finding we studied the interplay of host lattice and silver dynamics by a set of *gedankenexperiments*, performing constrained MD simulations. First of all, we fixed the silver atoms when analyzing the angular trajectories. The obtained trajectories can also be seen in see fig. 4.5. While there still are high frequency fluctuations around the expectation value obtained from the BCC structure, the long lasting low frequency deviations are no longer present. This can particularly well be seen in the FFT-filtered trajectories which are almost identical to the expected angle. We therefore conclude that the host lattice relaxational motion is closely related to silver motion being active or mute at this temperature.

What is more, however, we examined to what degree silver diffusion is influenced by iodine motion. Hence, we studied the MSD of the silver atoms for a set of *gedankenexperiments*. As shown by eq. (2.103), the slope of the MSD determines the diffusion constant, D. In case of full MD, i.e., all degrees of freedom are active according to the thermodynamic ensemble, we obtain a diffusion constant of $D = 2.6 \times 10^{-5}\text{cm}^2/\text{s}$ (black line in fig. 4.6). This value however, is significantly reduced when the iodine sublattice is frozen. In case of iodine atoms fixed at their ideal BCC positions, $D = 1.0 \times 10^{-5}\text{cm}^2/\text{s}$ is obtained (yellow line in fig. 4.6). This is even further reduced when iodine atoms are frozen at instantaneous, randomly selected configurations as obtained from the full MD simulation (red lines in fig. 4.6). In this case, diffusion constants of only $D = 0.3 \times 10^{-5}\text{cm}^2/\text{s}$ to $D = 0.7 \times 10^{-5}\text{cm}^2/\text{s}$ are obtained. It can be understood that the diffusion is slower in case of instantaneous configurations compared to BCC positions, when considering the potential energy landscape for diffusion. In case of iodines frozen to BCC positions, the potential barriers are of equal height (as sketched in figs. 4.1 and 4.7a). In case of instantaneous snapshots, however, the potential barriers are on different heights and silver atoms eventually

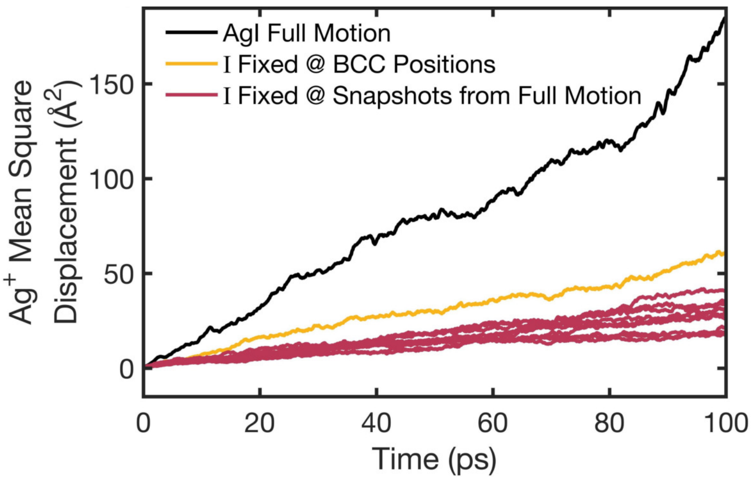

Figure 4.6.: Mean square displacement of the Ag^+ ions in α-AgI for different cases of constrained MD. The black line shows the MSD for full motion of Ag and I ions. The MSD with fixed I ions is shown in yellow for I ions fixed at the lattice positions of a BCC lattice, and in red with I ions fixed at positions obtained as snapshots from a full MD trajectory. *Reprinted with permission from [3]. Copyright (2020) by the American Physical Society.*

get caught in deeper potential wells, sketched in fig. 4.7b, in total slowing down silver diffusion.

Thus, fig. 4.7 presents our conclusions for full dynamics: the host lattice dynamics apparently are coupled to the diffusion dynamics, lowering the potential energy barriers for the Ag ions such that diffusion is enhanced. Only then, theory and experiment agree on the value of D. With this, we established a local tetrahedral model to describe lattice vibrations in α-AgI, and we discussed the presence of relaxational motion in the iodine host lattice and how it is facilitating silver diffusion [3]. This emphasizes the important role of anharmonicity to understand the structural dynamics in α-AgI and the implications for its hallmark functional property, the diffusion of silver ions.

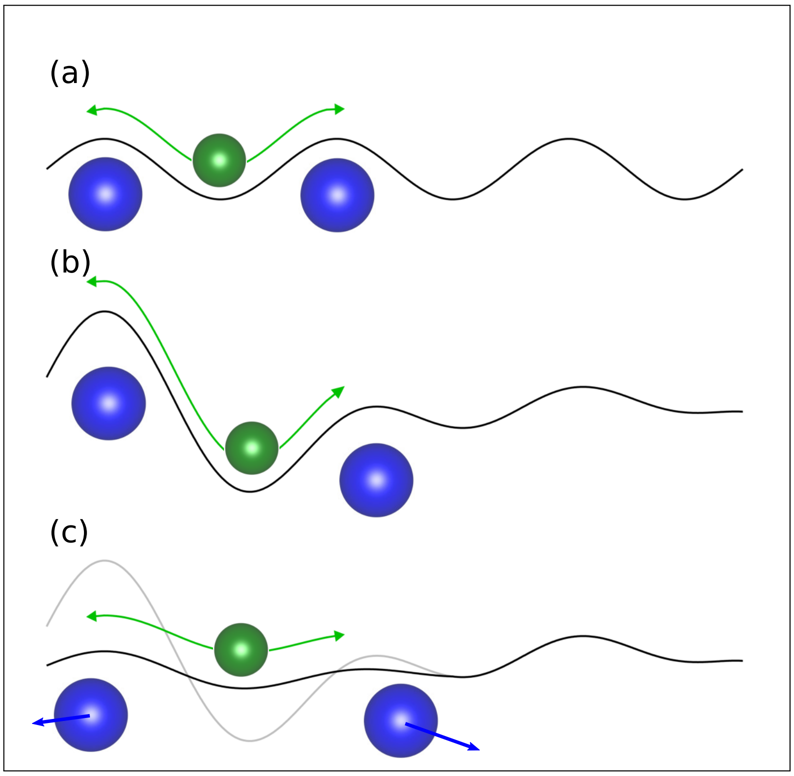

Figure 4.7.: Sketch showing the interplay between host-lattice ions (blue) potential energy landscapes (black) for diffusing ions (green) if host-lattice ions are **(a)** located at their equilibrium positions **(b)** located at instantaneous positions **(c)** allowed to move (blue arrows). In the last scenario, the instantaneous potential energy landscape from panel (b) (gray curve) gets modified (black curve), facilitating ion diffusion by a coupling of the dynamics of host-lattice and diffusing ions.

5. Conclusions and Outlook

Understanding finite temperature properties of energy materials on a microscopic level includes developing a profound understanding of structural dynamics in these materials. In crystals, structural dynamics are usually described and studied within the harmonic approximation, an approximation resulting in the well-known phonon quasi-particles with their **q**-point dependent dispersion relations. This approximation is well-established for many conventional materials, although anharmonic effects, such as finite phonon lifetimes and lattice expansion, are frequently discussed in textbooks. In particular, recent literature has discussed anharmonic effects in energy materials which are important for renewable energy.

Here in this work, structural dynamics in general, and anharmonicity in particular, as well as their implications for functional properties have been studied for paradigmatic energy materials, namely HaPs and the SSIC α-AgI. Specifically, to investigate the role of anharmonicity in all orders of the Taylor expansion as well as a lack of a well defined reference structure, first-principles MD simulations have been employed. These simulations allow to investigate the connection between anharmonic motion and functional properties, such as electronic properties.

Limitations of the harmonic approximation have been shown for HaPs, for which calculations of the IR spectrum within the harmonic approximation predict IR-active modes in $MAPbBr_3$ that are neither found in the inorganic $CsPbBr_3$ nor in experimentally measured spectra. This additional IR activity could further be linked to libration motion of the organic MA cation. Using MD simulations and correlation functions to calculate the IR spectrum, thus including a larger number of MA molecules and allowing them to reorient, this additional IR activity vanishes, resulting in a close resemblance of experimental and theoretical IR spectra. In particular, besides the large difference in the atomic masses of Cs and MA, the IR spectra of $CsPbBr_3$ and $MAPbBr_3$ are found to be very similar if the constraint on the molecular orientation, imposed by the periodic boundary conditions of usual computations, are loosened.

In $CsPbBr_3$ vibrational anharmonicity has been found although no anharmonic motion of a molecular A-site cation has to be considered. Harmonic phonon calculations of the cubic phase recovered imaginary phonon branches which, in literature, have been related to octahedral tilting and the temperature-dependent phase transitions. From this and an inspection of the differences in total energy between the ideal cubic structure and instantaneous structures obtained from a MD simulation it can be concluded that the cubic perovskite structure is located at a local maximum of the potential energy surface. Calculating finite temperature vibrational quasi-particles from MD simulations, using a normal mode projection, revealed the material to stabilize, i.e., no imaginary phonon modes are found anymore in a phonon dispersion calculated from MD at 425 K. Further, quasi-particle lifetimes have been found to be extremely short indicating an enormous degree of anharmonicity and a breakdown of the quasi-particle picture.

The anharmonic structural dynamics are connected to further material properties, such as bonding, band-edge energy distributions, and the JDOS. Anharmonicity in HaPs has been linked to their bonding, in particular to a mechanism called resonant bonding which is causing long-range effects, e.g., in the charge density. Indeed such long-range effects could be recovered for the average structure – tested by a small disturbance – for two properties, a direct inspection of the change in the charge density and the autocorrelation of the disorder potential. There is a dynamic shortening, particularly seen in the autocorrelation function of the disorder potential, as soon as relevant structures obtained from MD simulations at finite temperature are inspected. A short-range correlation in the disorder potential can be related to a small Urbach energy, favorable for solar absorbers in photovoltaic devices. Here, favorable band-edge distributions have been shown to coincide with short correlation lengths in the disorder potential. Last but not least, also for the JDOS, proportional to the number of possible band-to-band transitions under the approximation of constant transition matrix elements, a beneficial steepening close to the onset has been found in the case of structures from MD simulations in contrast with the average structure. Particularly, for the above mentioned quantities, as well as for the band gap, it could be shown that the average calculated from MD snapshots does not equal the values calculated from the average cubic structure. Performing various *gedankenexperiments* together with a comparison to PbTe, allowed to further pin down the effects responsible for the shortening of the correlation functions and the intensification of band-to-band transitions. It has been shown that especially anharmonic halide motion is involved. More precisely, it is the structural flexibility of the perovskite structure, allowing for motion transversal to the Pb-halide-Pb bonds, that is peculiar. This motion is also concurrent with octahedral rotation and multi-well potentials, in contrast to the motion longitudinal to the bond-axis.

Not only HaPs suffer from an incomplete description of structural dynamics when applying the harmonic approximation, also SSICs are effected by it. Using a combination of PO Raman experiments and MD simulations, lattice dynamics have been studied in the paradigmatic α-AgI with a particular focus on host-lattice anharmonicity. The Ag ions in α-AgI diffuse by jumping in between tetrahedral sites, thus distributing themselves among these sites. As a consequence, the average structure can hardly be taken as a reference, e.g., for harmonic phonon calculations. Further, it has been shown that the experimental Raman spectrum, probing vibrations at the Γ-point, corresponds remarkably well to the theoretically calculated VDOS, including vibrations at all points of the first Brillouin zone. This has been discussed to be an effect of the breakdown of translational invariance due to a failure of the averaged unit cell to represent instantaneous configurations. As has been shown, the average structure of α-AgI further fails to predict the PO dependence of the

Raman spectrum, as a too small number of Raman active modes would have been predicted. Interestingly, assuming Raman scattering from a completely disordered system, such as a liquid, fails to predict the correct PO response, too.

To study this "liquid-crystal conundrum“, the trajectories of I-I-I angles in AgI_4 tetrahedra, as obtained from MD simulations, have been analyzed. Large, long-lasting low frequency deviations from the expectation values could be observed for the angles. These low frequency changes of the angles indicate anharmonic relaxational motion in the iodine host-lattice. This provides a possible explanation for a central peak that has been found in the Raman spectrum. Moreover, a local motif – below unit cell dimensions – in form of the AgI_4 tetrahedron allows to resolve the "liquid-crystal conundrum“ and correctly predict the PO Raman spectrum.

A connection between iodine and silver motion could be established by performing a set of *gedankenexperiments*. First of all, it could be shown that the host-lattice relaxational motion only occurs if silver motion is allowed. Freezing the silver motion also hinders the host-lattice relaxational motion. And second, allowing for host-lattice motion aids silver diffusion as has been quantified by investigating the diffusion constant obtained from the MSD.

Taken together, we conclude that several HaPs and SSICs share some interesting features, in particular related to their structural dynamics. Among these common features are manifestations of anharmonicity, such as a central peak in the Raman spectra, which can be connected to the relaxational motion between instantaneous structures. More intriguing however, is the observation of localization due to anharmonic structural dynamics in both materials. This has been identified here for the correlation of the disorder potential in HaPs, which is dynamically localized, as well as for the Raman spectrum in α-AgI, which can only be described correctly using a "local tetrahedral model“.

Below this work will be put in a broader context and an outlook will be provided. It has been shown long ago that disorder localizes both charge carriers [274] and lattice vibrations [275, 276]. Judging from the (average) structure the materials studied in this work are not considered to be disordered or amorphous. However, the above results suggest to have an effect that results in localization for both materials, HaPs and α-AgI, which might be in line with the findings that their average structures do not represent a unique minimum in the potential energy surface. Therefore, *dynamic disorder* might be assumed. The effect of dynamic disorder on charge transport has been studied in organic crystals [277–281] and recently also suggested for HaPs [135]. However, many questions about the interesting topic of *dynamic localization* still remain to be investigated. For instance, understanding how dynamic disorder impacts structural dynamics and whether vibrations are dynamically localized could facilitate the search for efficient thermoelectric materials. Such materials require a *"electron crystal, phonon glass"*, i.e., the material should not be amorphous to display favorable electronic properties, however vibrations should be localized to find a low thermal conductivity [34].

Finally, oercoming the limitations of the harmonic approximation by performing computational research on those anharmonic materials can be expedited not only by the increase in computer power but also with the development of new methods. Among these mentionable developments is the usage of machine learning for performing and accelerating MD simulations, as has already been done for HaPs [27, 174, 282] and SSICs [283]. The trajectories obtained from (machine learned) force-field MD simulations can then be combined, for instance, with tight-binding calculations to study finite temperature electronic properties at reasonable computational costs, even in anharmonic materials [163, 284].

Bibliography

1. Beck, H., Gehrmann, C. & Egger, D. A. Structure and binding in halide perovskites: Analysis of static and dynamic effects from dispersion-corrected density functional theory. *APL Mater.* **7,** 021108. doi:`10.1063/1.5086541` (2019).
2. Gehrmann, C. & Egger, D. A. Dynamic shortening of disorder potentials in anharmonic halide perovskites. *Nat. Commun.* **10,** 3141. doi:`10.1038/s41467-019-11087-y` (2019).
3. Brenner, T. M. *et al.* Anharmonic host-lattice dynamics enable fast ion conduction in superionic AgI. *Phys. Rev. Mater.* **4,** 115402. doi:`10.1103/PhysRevMaterials.4.115402` (2020).
4. Seidl, S. A. *et al.* Assessing the accuracy of screened range-separated hybrids for bulk properties of semiconductors. *Phys. Rev. Mater.* **5,** 034602. doi:`10.1103/PhysRevMaterials.5.034602` (2021).
5. Gehrmann, C. *et al.* Transversal Halide Motion Intensifies Band-To-Band Transitions in Halide Perovskites. *Adv. Sci.,* 2200706. doi:`10.1002/advs.202200706` (2022).
6. Zhu, X. *et al.* Probing the Disorder Inside the Cubic Unit Cell of Halide Perovskites from First-Principles. *ACS Appl. Mater. Interfaces,* acsami.1c23099. doi:`10.1021/acsami.1c23099` (2022).
7. *Best Research-Cell Efficiency Chart* `https://www.nrel.gov/pv/cell-efficiency.html` (2021).
8. Kojima, A. *et al.* Organometal Halide Perovskites as Visible-Light Sensitizers for Photovoltaic Cells. *J. Am. Chem. Soc.* **131,** 6050–6051. doi:`10.1021/ja809598r` (2009).
9. Lee, M. M. *et al.* Efficient Hybrid Solar Cells Based on Meso-Superstructured Organometal Halide Perovskites. *Science* **338,** 643–647. doi:`10.1126/science.1228604` (2012).
10. Snaith, H. J. Perovskites: The Emergence of a New Era for Low-Cost, High-Efficiency Solar Cells. *J. Phys. Chem. Lett.* **4,** 3623–3630. doi:`10.1021/jz4020162` (2013).
11. Burschka, J. *et al.* Sequential deposition as a route to high-performance perovskite-sensitized solar cells. *Nature* **499,** 316–319. doi:`10.1038/nature12340` (2013).

12. Liu, M., Johnston, M. B. & Snaith, H. J. Efficient planar heterojunction perovskite solar cells by vapour deposition. *Nature* **501,** 395–398. doi:`10.1038/nature12509` (2013).

13. Park, N.-G. Organometal Perovskite Light Absorbers Toward a 20% Efficiency Low-Cost Solid-State Mesoscopic Solar Cell. *J. Phys. Chem. Lett.* **4,** 2423–2429. doi:`10.1021/jz400892a` (2013).

14. Kazim, S. *et al.* Perovskite as Light Harvester: A Game Changer in Photovoltaics. *Angew. Chem. Int. Ed.* **53,** 2812–2824. doi:`10.1002/anie.201308719` (2014).

15. Stranks, S. D. & Snaith, H. J. Metal-halide perovskites for photovoltaic and light-emitting devices. *Nat. Nanotechnol.* **10,** 391–402. doi:`10.1038/nnano.2015.90` (2015).

16. Brenner, T. M. *et al.* Hybrid organic—inorganic perovskites: low-cost semiconductors with intriguing charge-transport properties. *Nat. Rev. Mater.* **1,** 15007. doi:`10.1038/natrevmats.2015.7` (2016).

17. Correa-Baena, J.-P. *et al.* Promises and challenges of perovskite solar cells. *Science* **358,** 739–744. doi:`10.1126/science.aam6323` (2017).

18. Tsai, H. *et al.* Light-induced lattice expansion leads to high-efficiency perovskite solar cells. *Science* **360,** 67–70. doi:`10.1126/science.aap8671` (2018).

19. Sutherland, B. R. & Sargent, E. H. Perovskite photonic sources. *Nat. Photonics* **10,** 295–302. doi:`10.1038/nphoton.2016.62` (2016).

20. Kim, H. *et al.* Halide Perovskites for Applications beyond Photovoltaics. *Small Methods* **2,** 1700310. doi:`10.1002/smtd.201700310` (2018).

21. Sharma, R. *et al.* Elucidating the atomistic origin of anharmonicity in tetragonal $CH_3NH_3PbI_3$ with Raman scattering. *Phys. Rev. Mater.* **4,** 092401. doi:`10.1103/PhysRevMaterials.4.092401` (2020).

22. Gold-Parker, A. *et al.* Acoustic phonon lifetimes limit thermal transport in methylammonium lead iodide. *Proc. Natl. Acad. Sci. U.S.A.* **115,** 11905–11910. doi:`10.1073/pnas.1812227115` (2018).

23. Miyata, K., Atallah, T. L. & Zhu, X.-Y. Lead halide perovskites: Crystal-liquid duality, phonon glass electron crystals, and large polaron formation. *Sci. Adv.* **3,** e1701469. doi:`10.1126/sciadv.1701469` (2017).

24. Yaffe, O. *et al.* Local Polar Fluctuations in Lead Halide Perovskite Crystals. *Phys. Rev. Lett.* **118,** 136001. doi:`10.1103/PhysRevLett.118.136001` (2017).

25. Zhou, L. *et al.* Density of States Broadening in $CH_3NH_3PbI_3$ Hybrid Perovskites Understood from ab Initio Molecular Dynamics Simulations. *ACS Energy Lett.* **3,** 787–793. doi:`10.1021/acsenergylett.8b00166` (2018).

26. Whalley, L. D. *et al.* Phonon anharmonicity, lifetimes, and thermal transport in $CH_3NH_3PbI_3$ from many-body perturbation theory. *Phys. Rev. B* **94,** 220301(R). doi:`10.1103/PhysRevB.94.220301` (2016).

27. Lahnsteiner, J. & Bokdam, M. Anharmonic lattice dynamics in large thermodynamic ensembles with machine-learning force fields: $CsPbBr_3$, a phonon liquid with Cs rattlers. *Phys. Rev. B* **105,** 024302. doi:`10.1103/PhysRevB.105.024302` (2022).
28. Hwang, J. *et al.* Performance characteristics of pentacene-based organic photovoltaic cells. *Org. Electron.* **13,** 1809–1818. doi:`10.1016/j.orgel.2012.05.042` (2012).
29. Jindal, V. K. & Kalus, J. A calculation of the anharmonic phonon frequencies in solid deuterated naphthalene-d_8. *J. Phys. C: Solid State Phys.* **16,** 3061–3080. doi:`10.1088/0022-3719/16/16/011` (1983).
30. Sheka, E. F. *et al.* Anharmonicity of phonons in crystalline naphthalene. *J. Phys. C: Solid State Phys.* **17,** 5893–5914. doi:`10.1088/0022-3719/17/33/004` (1984).
31. Asher, M. *et al.* Anharmonic Lattice Vibrations in Small-Molecule Organic Semiconductors. *Adv. Mater.* **32,** 1908028. doi:`10.1002/adma.201908028` (2020).
32. Huggins, R. *Advanced Batteries* (Springer US, 2009).
33. Beekman, M., Morelli, D. T. & Nolas, G. S. Better thermoelectrics through glass-like crystals. *Nat. Mater.* **14,** 1182–1185. doi:`10.1038/nmat4461` (2015).
34. Slack, G. A. in *CRC Handbook of Thermoelectrics* 407 (CRC Press, 1995).
35. Ashcroft, N. W. & Mermin, N. D. *Solid state physics* (Holt, Rinehart and Winston, New York, 1976).
36. Gross, R. & Marx, A. *Festkörperphysik* (Oldenbourg, München, 2012).
37. Fiolhais, C., Nogueira, F. & Marques, M. *A Primer in Density Functional Theory* (Springer Berlin Heidelberg, 2003).
38. Born, M. & Huang, K. *Dynamical Theory of Crystal Lattices* (Oxford University Press, 1954).
39. Dove, M. T. *Introduction to Lattice Dynamics* doi:`10.1017/CBO9780511619885` (Cambridge University Press, Cambridge, 1993).
40. Frenkel, D. & Smit, B. *Understanding Molecular Simulation : From Algorithms to Applications* (Elsevier Science & Technology, San Diego, 2001).
41. Marx, D. & Hutter, J. *Ab Initio Molecular Dynamics: Basic Theory and Advanced Methods* doi:`10.1017/CBO9780511609633` (Cambridge University Press, Cambridge, 2009).
42. *The VASP Manual - Vaspwiki* `https://www.vasp.at/wiki/index.php/The_VASP_Manual` (2022).
43. *Phonopy* `https://phonopy.github.io/phonopy/` (2021).
44. *LAMMPS Documentation* `https://docs.lammps.org/Manual.html` (2021).
45. Born, M. & Oppenheimer, R. Zur Quantentheorie der Molekeln. *Ann. Phys.* **389,** 457–484. doi:`10.1002/andp.19273892002` (1927).

46. Hohenberg, P. & Kohn, W. Inhomogeneous Electron Gas. *Phys. Rev.* **136,** B864–B871. doi:`10.1103/PhysRev.136.B864` (1964).
47. Kohn, W. & Sham, L. J. Self-Consistent Equations Including Exchange and Correlation Effects. *Phys. Rev.* **140,** A1133–A1138. doi:`10.1103/PhysRev.140.A1133` (1965).
48. Ceperley, D. M. & Alder, B. J. Ground State of the Electron Gas by a Stochastic Method. *Phys. Rev. Lett.* **45,** 566–569. doi:`10.1103/PhysRevLett.45.566` (1980).
49. Perdew, J. P., Burke, K. & Ernzerhof, M. Generalized gradient approximation made simple. *Phys. Rev. Lett.* **77,** 3865 (1996).
50. Kurth, S., Perdew, J. P. & Blaha, P. Molecular and solid-state tests of density functional approximations: LSD, GGAs, and meta-GGAs. *Int. J. Quant. Chem.* **75,** 889–909. doi:`10.1002/(SICI)1097-461X(1999)75:4/5<889::AID-QUA54>3.0.CO;2-8` (1999).
51. Staroverov, V. N. *et al.* Tests of a ladder of density functionals for bulk solids and surfaces. *Phys. Rev. B* **69,** 075102. doi:`10.1103/PhysRevB.69.075102` (2004).
52. Quester, W. `https://commons.wikimedia.org/wiki/File:Sketch_Pseudopotentials.png` (2022).
53. Feng, J. Mechanical properties of hybrid organic-inorganic $CH_3NH_3BX_3$ (B = Sn, Pb; X = Br, I) perovskites for solar cell absorbers. *APL Mater.* **2,** 081801. doi:`10.1063/1.4885256` (2014).
54. Kabakova, I. V. *et al.* The effect of ionic composition on acoustic phonon speeds in hybrid perovskites from Brillouin spectroscopy and density functional theory. *J. Mater. Chem. C* **6,** 3861–3868. doi:`10.1039/C8TC00875B` (2018).
55. Wang, Y. *et al.* Density functional theory analysis of structural and electronic properties of orthorhombic perovskite $CH_3NH_3PbI_3$. *Phys. Chem. Chem. Phys.* **16,** 1424–1429. doi:`10.1039/C3CP54479F` (2014).
56. Egger, D. A. & Kronik, L. Role of Dispersive Interactions in Determining Structural Properties of Organic–Inorganic Halide Perovskites: Insights from First-Principles Calculations. *J. Phys. Chem. Lett.* **5,** 2728–2733. doi:`10.1021/jz5012934` (2014).
57. Motta, C. *et al.* Revealing the role of organic cations in hybrid halide perovskite $CH_3NH_3PbI_3$. *Nat. Commun.* **6.** doi:`10.1038/ncomms8026` (2015).
58. Li, J. & Rinke, P. Atomic structure of metal-halide perovskites from first principles: The chicken-and-egg paradox of the organic-inorganic interaction. *Phys. Rev. B* **94,** 045201. doi:`10.1103/PhysRevB.94.045201` (2016).
59. Faghihnasiri, M., Izadifard, M. & Ghazi, M. E. DFT Study of Mechanical Properties and Stability of Cubic Methylammonium Lead Halide Perovskites ($CH_3NH_3PbX_3$, X = I, Br, Cl). *J. Phys. Chem. C* **121,** 27059–27070. doi:`10.1021/acs.jpcc.7b07129` (2017).

60. Motta, C., El-Mellouhi, F. & Sanvito, S. Exploring the cation dynamics in lead-bromide hybrid perovskites. *Phys. Rev. B* **93,** 235412. doi:`10.1103/PhysRevB.93.235412` (2016).

61. Tkatchenko, A. & Scheffler, M. Accurate Molecular Van Der Waals Interactions from Ground-State Electron Density and Free-Atom Reference Data. *Phys. Rev. Lett.* **102,** 073005. doi:`10.1103/PhysRevLett.102.073005` (2009).

62. Marom, N. *et al.* Dispersion Interactions with Density-Functional Theory: Benchmarking Semiempirical and Interatomic Pairwise Corrected Density Functionals. *J. Chem. Theory Comput.* **7,** 3944–3951. doi:`10.1021/ct2005616` (2011).

63. Al-Saidi, W. A., Voora, V. K. & Jordan, K. D. An Assessment of the vdW-TS Method for Extended Systems. *J. Chem. Theory Comput.* **8,** 1503–1513. doi:`10.1021/ct200618b` (2012).

64. Dolling, G. *Inelastic Scattering of Neutrons in Solids and Liquids* (International Atomic Energy Agency, Vienna, 1963).

65. Nilsson, G. & Nelin, G. Study of the Homology between Silicon and Germanium by Thermal-Neutron Spectrometry. *Phys. Rev. B* **6,** 3777–3786. doi:`10.1103/PhysRevB.6.3777` (1972).

66. Togo, A. & Tanaka, I. First principles phonon calculations in materials science. *Scr. Mater.* **108,** 1–5 (2015).

67. Mott, N. F. & Davis, E. A. *Electronic processes in non-crystalline materials* 2nd ed (Clarendon Press, Oxford, 2012).

68. Chaput, L. *et al.* Phonon-phonon interactions in transition metals. *Phys. Rev. B* **84.** doi:`10.1103/PhysRevB.84.094302` (2011).

69. Togo, A., Chaput, L. & Tanaka, I. Distributions of phonon lifetimes in Brillouin zones. *Phys. Rev. B* **91,** 094306. doi:`10.1103/PhysRevB.91.094306` (2015).

70. Tadano, T. & Tsuneyuki, S. Self-consistent phonon calculations of lattice dynamical properties in cubic $SrTiO_3$ with first-principles anharmonic force constants. *Phys. Rev. B* **92.** doi:`10.1103/PhysRevB.92.054301` (2015).

71. Hellman, O. *et al.* Temperature dependent effective potential method for accurate free energy calculations of solids. *Phys. Rev. B* **87,** 104111. doi:`10.1103/PhysRevB.87.104111` (2013).

72. Errea, I., Rousseau, B. & Bergara, A. Anharmonic Stabilization of the High-Pressure Simple Cubic Phase of Calcium. *Phys. Rev. Lett.* **106.** doi:`10.1103/PhysRevLett.106.165501` (2011).

73. Errea, I., Calandra, M. & Mauri, F. Anharmonic free energies and phonon dispersions from the stochastic self-consistent harmonic approximation: Application to platinum and palladium hydrides. *Phys. Rev. B* **89.** doi:`10.1103/PhysRevB.89.064302` (2014).

74. Giannozzi, P. & Baroni, S. Vibrational and dielectric properties of C_{60} from density-functional perturbation theory. *J. Chem. Phys.* **100,** 8537–8539. doi:`10.1063/1.466753` (1994).

75. Porezag, D. & Pederson, M. R. Infrared intensities and Raman-scattering activities within density-functional theory. *Phys. Rev. B* **54,** 7830–7836. doi:`10.1103/PhysRevB.54.7830` (1996).
76. Karhánek, D., Bučko, T. & Hafner, J. A density-functional study of the adsorption of methane-thiol on the (111) surfaces of the Ni-group metals: II. Vibrational spectroscopy. *J. Phys.: Condens. Matter* **22,** 265006. doi:`10.1088/0953-8984/22/26/265006` (2010).
77. Karhánek. *Self-Assembled Monolayers Studied by Density-Functional Theory* PhD thesis (Wien, 2010).
78. Skelton, J. M. *et al.* Lattice dynamics of the tin sulphides SnS_2, SnS and Sn_2S_3: vibrational spectra and thermal transport. *Phys. Chem. Chem. Phys.* **19,** 12452–12465. doi:`10.1039/C7CP01680H` (2017).
79. Gonze, X. & Lee, C. Dynamical matrices, Born effective charges, dielectric permittivity tensors, and interatomic force constants from density-functional perturbation theory. *Phys. Rev. B* **55,** 10355–10368. doi:`10.1103/PhysRevB.55.10355` (1997).
80. Gaigeot, M.-P. & Sprik, M. Ab Initio Molecular Dynamics Computation of the Infrared Spectrum of Aqueous Uracil. *J. Phys. Chem. B* **107,** 10344–10358. doi:`10.1021/jp034788u` (2003).
81. Thomas, M. *et al.* Computing vibrational spectra from ab initio molecular dynamics. *Phys. Chem. Chem. Phys.* **15,** 6608. doi:`10.1039/c3cp44302g` (2013).
82. Pallikara, I. *et al.* The Physical Significance of Imaginary Phonon Modes in Crystals. *arXiv:2203.01244 [cond-mat]* (2022).
83. Hayes, W. & Loudon, R. *Scattering of Light by Crystals* (Dover Publications, 2004).
84. Vashishta, P. & Rahman, A. Ionic Motion in α -AgI. *Phys. Rev. Lett.* **40,** 1337–1340. doi:`10.1103/PhysRevLett.40.1337` (1978).
85. Hata, T. *et al.* Development of a Classical Interatomic Potential for $MAPbBr_3$. *J. Phys. Chem. C* **121,** 3724–3733. doi:`10.1021/acs.jpcc.6b11298` (2017).
86. Mattoni, A. *et al.* Methylammonium Rotational Dynamics in Lead Halide Perovskite by Classical Molecular Dynamics: The Role of Temperature. *J. Phys. Chem. C* **119,** 17421–17428. doi:`10.1021/acs.jpcc.5b04283` (2015).
87. Ponder, J. W. & Case, D. A. in *Advances in Protein Chemistry* 27–85 (Elsevier, 2003). doi:`10.1016/S0065-3233(03)66002-X`.
88. Verlet, L. Computer "Experiments" on Classical Fluids. I. Thermodynamical Properties of Lennard-Jones Molecules. *Phys. Rev.* **159,** 98–103. doi:`10.1103/PhysRev.159.98` (1967).
89. Tuckerman, M., Berne, B. J. & Martyna, G. J. Reversible multiple time scale molecular dynamics. *J. Chem. Phys.* **97,** 1990–2001. doi:`10.1063/1.463137` (1992).

90. Hünenberger, P. H. in *Advanced Computer Simulation* (eds Abe, A. *et al.*) 105–149 (Springer Berlin Heidelberg, Berlin, Heidelberg, 2005). doi:`10.1007/b99427`.
91. Nosé, S. A unified formulation of the constant temperature molecular dynamics methods. *J. Chem. Phys.* **81,** 511–519. doi:`10.1063/1.447334` (1984).
92. Hoover, W. G. Canonical dynamics: Equilibrium phase-space distributions. *Phys. Rev. A* **31,** 1695–1697. doi:`10.1103/PhysRevA.31.1695` (1985).
93. Andersen, H. C. Molecular dynamics simulations at constant pressure and/or temperature. *J. Chem. Phys.* **72,** 2384–2393. doi:`10.1063/1.439486` (1980).
94. Berendsen, H. J. C. *et al.* Molecular dynamics with coupling to an external bath. *J. Chem. Phys.* **81,** 3684–3690. doi:`10.1063/1.448118` (1984).
95. Schneider, T. & Stoll, E. Molecular-dynamics study of a three-dimensional one-component model for distortive phase transitions. *Phys. Rev. B* **17,** 1302–1322. doi:`10.1103/PhysRevB.17.1302` (1978).
96. Evans, D. J. Computer "experiment" for nonlinear thermodynamics of Couette flow. *J. Chem. Phys.* **78,** 3297–3302. doi:`10.1063/1.445195` (1983).
97. Parrinello, M. & Rahman, A. Polymorphic transitions in single crystals: A new molecular dynamics method. *J. Appl. Phys.* **52,** 7182–7190. doi:`10.1063/1.328693` (1981).
98. Martyna, G. J., Tobias, D. J. & Klein, M. L. Constant pressure molecular dynamics algorithms. *J. Chem. Phys.* **101,** 4177–4189. doi:`10.1063/1.467468` (1994).
99. Braun, E. *et al.* Best Practices for Foundations in Molecular Simulations. *Living J. Comp. Mol. Sci.* **1.** doi:`10.33011/livecoms.1.1.5957` (2019).
100. Mohazzabi, P. & Shankar, S. Maxwell-Boltzmann Distribution in Solids. *J. Appl. Phys.* **06,** 602–612. doi:`10.4236/jamp.2018.63052` (2018).
101. Nitzan, A. in *Chemical dynamics in condensed phases: relaxation, transfer and reactions in condensed molecular systems* (Oxford University Press, Oxford; New York, 2006).
102. Gordon, R. in *Advances in Magnetic and Optical Resonance* 1–42 (Elsevier, 1968). doi:`10.1016/B978-1-4832-3116-7.50008-4`.
103. Mathias, G. *et al.* Infrared Spectroscopy of Fluxional Molecules from (ab Initio) Molecular Dynamics: Resolving Large-Amplitude Motion, Multiple Conformations, and Permutational Symmetries. *J. Chem. Theory Comput.* **8,** 224–234. doi:`10.1021/ct2006665` (2012).
104. Fischer, S. A. *et al.* Infrared and Raman Spectroscopy from Ab Initio Molecular Dynamics and Static Normal Mode Analysis: The C–H Region of DMSO as a Case Study. *J. Phys. Chem. B* **120,** 1429–1436. doi:`10.1021/acs.jpcb.5b03323` (2016).
105. Carreras, A., Togo, A. & Tanaka, I. DynaPhoPy: A code for extracting phonon quasiparticles from molecular dynamics simulations. *Comput. Phys. Commun.* **221,** 221–234. doi:`10.1016/j.cpc.2017.08.017` (2017).

106. Sun, T., Zhang, D.-B. & Wentzcovitch, R. M. Dynamic stabilization of cubic $CaSiO_3$ perovskite at high temperatures and pressures from *ab initio* molecular dynamics. *Phys. Rev. B* **89,** 094109. doi:`10.1103/PhysRevB.89.094109` (2014).
107. McGaughey, A. J. H. & Larkin, J. M. Predicting Phonon Properties from Equilibrium Molecular Dynamics Simulations. *Annu. Rev. Heat Transf.* **17,** 49–87. doi:`10.1615/AnnualRevHeatTransfer.2013006915` (2014).
108. Sun, T., Shen, X. & Allen, P. B. Phonon quasiparticles and anharmonic perturbation theory tested by molecular dynamics on a model system. *Phys. Rev. B* **82.** doi:`10.1103/PhysRevB.82.224304` (2010).
109. Zhang, D.-B., Sun, T. & Wentzcovitch, R. M. Phonon Quasiparticles and Anharmonic Free Energy in Complex Systems. *Phys. Rev. Lett.* **112,** 058501. doi:`10.1103/PhysRevLett.112.058501` (2014).
110. Sritrakool, W., Sa-yakanit, V. & Glyde, H. R. Band tails in disordered systems. *Phys. Rev. B* **33,** 1199–1202. doi:`10.1103/PhysRevB.33.1199` (1986).
111. John, S. *et al.* Theory of Electron Band Tails and the Urbach Optical-Absorption Edge. *Phys. Rev. Lett.* **57,** 1777–1780. doi:`10.1103/PhysRevLett.57.1777` (1986).
112. Greeff, C. W. & Glyde, H. R. Anomalous Urbach tail in GaAs. *Phys. Rev. B* **51,** 1778–1783. doi:`10.1103/PhysRevB.51.1778` (1995).
113. Urbach, F. The Long-Wavelength Edge of Photographic Sensitivity and of the Electronic Absorption of Solids. *Phys. Rev.* **92,** 1324–1324. doi:`10.1103/PhysRev.92.1324` (1953).
114. Studenyak, I., Kranjčec, M. & Kurik, M. Urbach Rule in Solid State Physics. *Int. J. Opt.* **4,** 76–83. doi:`10.5923/j.optics.20140403.02` (2014).
115. Kresse, G. & Furthmüller, J. Efficient iterative schemes for ab initio total-energy calculations using a plane-wave basis set. *Phys. Rev. B* **54,** 11169. doi:`10.1103/PhysRevB.54.11169` (1996).
116. Kresse, G. & Joubert, D. From ultrasoft pseudopotentials to the projector augmented-wave method. *Phys. Rev. B* **59,** 1758 (1999).
117. Momma, K. & Izumi, F. *VESTA3* for three-dimensional visualization of crystal, volumetric and morphology data. *J. Appl. Crystallogr.* **44,** 1272–1276. doi:`10.1107/S0021889811038970` (2011).
118. Bučko, T., Hafner, J. & Ángyán, J. G. Geometry optimization of periodic systems using internal coordinates. *J. Chem. Phys.* **122,** 124508. doi:`10.1063/1.1864932` (2005).
119. *Phonopy-Spectroscopy* `https://github.com/JMSkelton/Phonopy-Spectroscopy` (2021).
120. Baroni, S. & Resta, R. *Ab initio* calculation of the macroscopic dielectric constant in silicon. *Phys. Rev. B* **33,** 7017–7021. doi:`10.1103/PhysRevB.33.7017` (1986).

121. Gajdoš, M. *et al.* Linear optical properties in the projector-augmented wave methodology. *Phys. Rev. B* **73,** 045112. doi:`10.1103/PhysRevB.73.045112` (2006).
122. Plimpton, S. Fast Parallel Algorithms for Short-Range Molecular Dynamics. *J. Comput. Phys.* **117,** 1–19. doi:`10.1006/jcph.1995.1039` (1995).
123. Mattoni, A. *et al.* Temperature Evolution of Methylammonium Trihalide Vibrations at the Atomic Scale. *J. Phys. Chem. Lett.* **7,** 529–535. doi:`10.1021/acs.jpclett.5b02546` (2016).
124. Wang, V. *et al.* VASPKIT: A user-friendly interface facilitating high-throughput computing and analysis using VASP code. *Comput. Phys. Commun.* **267,** 108033. doi:`10.1016/j.cpc.2021.108033`. eprint: `1908.08269` (2021).
125. Togo, A. & Tanaka, I. First principles phonon calculations in materials science. *Scr. Mater.* **108,** 1–5. doi:`10.1016/j.scriptamat.2015.07.021` (2015).
126. Goldschmidt, V. M. Die Gesetze der Krystallochemie. *Naturwissenschaften* **14,** 477–485. doi:`10.1007/BF01507527` (1926).
127. Sadhanala, A. *et al.* Preparation of Single-Phase Films of $CH_3NH_3Pb(I_{1-x}Br_x)_3$ with Sharp Optical Band Edges. *J. Phys. Chem. Lett.* **5,** 2501–2505. doi:`10.1021/jz501332v` (2014).
128. De Wolf, S. *et al.* Organometallic Halide Perovskites: Sharp Optical Absorption Edge and Its Relation to Photovoltaic Performance. *J. Phys. Chem. Lett.* **5,** 1035–1039. doi:`10.1021/jz500279b` (2014).
129. Senanayak, S. P. *et al.* Understanding charge transport in lead iodide perovskite thin-film field-effect transistors. *Sci. Adv.* **3,** e1601935. doi:`10.1126/sciadv.1601935` (2017).
130. Patel, J. B. *et al.* Photocurrent Spectroscopy of Perovskite Solar Cells Over a Wide Temperature Range from 15 to 350 K. *J. Phys. Chem. Lett.* **9,** 263–268. doi:`10.1021/acs.jpclett.7b02935` (2018).
131. Ledinsky, M. *et al.* Temperature Dependence of the Urbach Energy in Lead Iodide Perovskites. *J. Phys. Chem. Lett.* **10,** 1368–1373. doi:`10.1021/acs.jpclett.9b00138` (2019).
132. Jeong, J. *et al.* Pseudo-halide anion engineering for α-FAPbI3 perovskite solar cells. *Nature* **592,** 381–385. doi:`10.1038/s41586-021-03406-5` (2021).
133. Whalley, L. D. *et al.* Perspective: Theory and simulation of hybrid halide perovskites. *J. Chem. Phys.* **146,** 220901. doi:`10.1063/1.4984964` (2017).
134. Wright, A. D. *et al.* Electron–phonon coupling in hybrid lead halide perovskites. *Nat. Commun.* **7.** doi:`10.1038/ncomms11755` (2016).
135. Schilcher, M. J. *et al.* The Significance of Polarons and Dynamic Disorder in Halide Perovskites. *ACS Energy Lett.* **6,** 2162–2173. doi:`10.1021/acsenergylett.1c00506` (2021).
136. Sun, S. *et al.* Mechanical properties of organic–inorganic halide perovskites, $CH_3NH_3PbX_3$ (X = I, Br and Cl), by nanoindentation. *J. Mater. Chem. A* **3,** 18450–18455. doi:`10.1039/C5TA03331D` (2015).

137. Rakita, Y. *et al.* Mechanical properties of $APbX_3$ (A = Cs or CH_3NH_3; X= I or Br) perovskite single crystals. *MRS Commun.* **5,** 623–629. doi:`10.1557/mrc.2015.69` (2015).

138. Létoublon, A. *et al.* Elastic Constants, Optical Phonons, and Molecular Relaxations in the High Temperature Plastic Phase of the $CH_3NH_3PbBr_3$ Hybrid Perovskite. *J. Phys. Chem. Lett.* **7,** 3776–3784. doi:`10.1021/acs.jpclett.6b01709` (2016).

139. Egger, D. A. *et al.* What Remains Unexplained about the Properties of Halide Perovskites? *Adv. Mater.* **30,** 1800691. doi:`10.1002/adma.201800691` (2018).

140. Ferreira, A. C. *et al.* Elastic Softness of Hybrid Lead Halide Perovskites. *Phys. Rev. Lett.* **121,** 085502. doi:`10.1103/PhysRevLett.121.085502` (2018).

141. Ferreira, A. C. *et al.* Direct evidence of weakly dispersed and strongly anharmonic optical phonons in hybrid perovskites. *Commun. Phys.* **3,** 48. doi:`10.1038/s42005-020-0313-7` (2020).

142. Hehlen, B. *et al.* Pseudospin-phonon pretransitional dynamics in lead halide hybrid perovskites. *Phys. Rev. B* **105,** 024306. doi:`10.1103/PhysRevB.105.024306` (2022).

143. Hirotsu, S. *et al.* Structural Phase Transitions in $CsPbBr\ _3$. *J. Phys. Soc. Jpn.* **37,** 1393–1398. doi:`10.1143/JPSJ.37.1393` (1974).

144. Marronnier, A. *et al.* Structural Instabilities Related to Highly Anharmonic Phonons in Halide Perovskites. *J. Phys. Chem. Lett.* **8,** 2659–2665. doi:`10.1021/acs.jpclett.7b00807` (2017).

145. Beecher, A. N. *et al.* Direct Observation of Dynamic Symmetry Breaking above Room Temperature in Methylammonium Lead Iodide Perovskite. *ACS Energy Lett.* **1,** 880–887. doi:`10.1021/acsenergylett.6b00381` (2016).

146. Marronnier, A. *et al.* Anharmonicity and Disorder in the Black Phases of Cesium Lead Iodide Used for Stable Inorganic Perovskite Solar Cells. *ACS Nano* **12,** 3477–3486. doi:`10.1021/acsnano.8b00267` (2018).

147. Brivio, F. *et al.* Lattice dynamics and vibrational spectra of the orthorhombic, tetragonal, and cubic phases of methylammonium lead iodide. *Phys. Rev. B* **92,** 144308. doi:`10.1103/PhysRevB.92.144308` (2015).

148. Da Silva, E. L. *et al.* Phase stability and transformations in the halide perovskite $CsSnI_3$. *Phys. Rev. B* **91.** doi:`10.1103/PhysRevB.91.144107` (2015).

149. Patrick, C. E., Jacobsen, K. W. & Thygesen, K. S. Anharmonic stabilization and band gap renormalization in the perovskite $CsSnI_3$. *Phys. Rev. B* **92,** 201205. doi:`10.1103/PhysRevB.92.201205` (2015).

150. Yang, R. X. *et al.* Spontaneous Octahedral Tilting in the Cubic Inorganic Caesium Halide Perovskites $CsSnX_3$ and $CsPbX_3$ (X = F, Cl, Br, I). *J. Phys. Chem. Lett.* **8,** 4720–4726. doi:`10.1021/acs.jpclett.7b02423` (2017).

151. Stoumpos, C. C. *et al.* Crystal Growth of the Perovskite Semiconductor $CsPbBr_3$: A New Material for High-Energy Radiation Detection. *Cryst. Growth Des.* **13,** 2722–2727. doi:`10.1021/cg400645t` (2013).

152. Poglitsch, A. & Weber, D. Dynamic disorder in methylammoniumtrihalogenoplumbates (II) observed by millimeter-wave spectroscopy. *J. Chem. Phys.* **87,** 6373–6378. doi:`10.1063/1.453467` (1987).

153. Onoda-Yamamuro, N., Matsuo, T. & Suga, H. Calorimetric and IR spectroscopic studies of phase transitions in methylammonium trihalogenoplumbates (II). *J. Phys. Chem. Solids* **51,** 1383–1395. doi:`10.1016/0022-3697(90)90021-7` (1990).

154. Keshavarz, M. *et al.* Tracking Structural Phase Transitions in Lead-Halide Perovskites by Means of Thermal Expansion. *Adv. Mater.,* 9 (2019).

155. Even, J., Carignano, M. & Katan, C. Molecular disorder and translation/-rotation coupling in the plastic crystal phase of hybrid perovskites. *Nanoscale* **8,** 6222–6236. doi:`10.1039/C5NR06386H` (2016).

156. Carignano, M. A. *et al.* Critical Fluctuations and Anharmonicity in Lead Iodide Perovskites from Molecular Dynamics Supercell Simulations. *J. Phys. Chem. C* **121,** 20729–20738. doi:`10.1021/acs.jpcc.7b08220` (2017).

157. Neukirch, A. J. *et al.* Polaron Stabilization by Cooperative Lattice Distortion and Cation Rotations in Hybrid Perovskite Materials. *Nano Lett.* **16,** 3809–3816. doi:`10.1021/acs.nanolett.6b01218` (2016).

158. Zhu, T. & Ertekin, E. Mixed phononic and non-phononic transport in hybrid lead halide perovskites: glass-crystal duality, dynamical disorder, and anharmonicity. *Energy Environ. Sci.* **12,** 216–229. doi:`10.1039/C8EE02820F` (2019).

159. Rodová, M. Phase transitions in ternary caesium lead bromide. *J. Therm. Anal. Calorim.* **71,** 667–673 (2003).

160. *Materials Data on CsPbBr3 by Materials Project* `https://www.osti.gov/servlets/purl/1330982/` (2021).

161. Munson, K. T. *et al.* Does Dipolar Motion of Organic Cations Affect Polaron Dynamics and Bimolecular Recombination in Halide Perovskites? *J. Phys. Chem. Lett.* **11,** 3166–3172. doi:`10.1021/acs.jpclett.0c00762` (2020).

162. Poncé, S., Schlipf, M. & Giustino, F. Origin of Low Carrier Mobilities in Halide Perovskites. *ACS Energy Lett.* **4,** 456–463. doi:`10.1021/acsenergylett.8b02346` (2019).

163. Mayers, M. Z. *et al.* How Lattice and Charge Fluctuations Control Carrier Dynamics in Halide Perovskites. *Nano Lett.* **18,** 8041–8046. doi:`10.1021/acs.nanolett.8b04276` (2018).

164. Lanigan-Atkins, T. *et al.* Two-dimensional overdamped fluctuations of the soft perovskite lattice in $CsPbBr_3$. *Nat. Mater.* **20,** 977–983. doi:`10.1038/s41563-021-00947-y` (2021).

165. Sendner, M. *et al.* Optical phonons in methylammonium lead halide perovskites and implications for charge transport. *Mater. Horiz.* **3,** 613–620. doi:`10.1039/C6MH00275G` (2016).

166. Pérez-Osorio, M. A. *et al.* Vibrational Properties of the Organic–Inorganic Halide Perovskite $CH_3NH_3PbI_3$ from Theory and Experiment: Factor Group Analysis, First-Principles Calculations, and Low-Temperature Infrared Spectra. *J. Phys. Chem. C* **119,** 25703–25718. doi:`10.1021/acs.jpcc.5b07432` (2015).
167. Sendner, M., Beck, S. & Lovrincic, R. *Unpublished experimental measurements on* $CsPbBr_3$
168. Li, J. *et al.* Inter-Conversion between Different Compounds of Ternary Cs-Pb-Br System. *Materials* **11,** 717. doi:`10.3390/ma11050717` (2018).
169. Yang, D. *et al.* All-inorganic cesium lead halide perovskite nanocrystals: synthesis, surface engineering and applications. *J. Mater. Chem. C* **7,** 757–789. doi:`10.1039/C8TC04381G` (2019).
170. Toso, S., Baranov, D. & Manna, L. Hidden in Plain Sight: The Overlooked Influence of the Cs^+ Substructure on Transformations in Cesium Lead Halide Nanocrystals. *ACS Energy Lett.* **5,** 3409–3414. doi:`10.1021/acsenergylett.0c02029` (2020).
171. Pérez-Osorio, M. A. *et al.* Van der Waals Interactions and Anharmonicity in the Lattice Vibrations, Dielectric Constants, Effective Charges, and Infrared Spectra of the Organic–Inorganic Halide Perovskite $CH_3NH_3PbI_3$. *J. Phys. Chem. C* **121,** 18459–18471. doi:`10.1021/acs.jpcc.7b07121` (2017).
172. Pérez-Osorio, M. A. *et al.* Raman Spectrum of the Organic–Inorganic Halide Perovskite $CH_3NH_3PbI_3$ from First Principles and High-Resolution Low-Temperature Raman Measurements. *J. Phys. Chem. C* **122,** 21703–21717. doi:`10.1021/acs.jpcc.8b04669` (2018).
173. Berreman, D. W. Infrared Absorption at Longitudinal Optic Frequency in Cubic Crystal Films. *Phys. Rev.* **130,** 2193–2198. doi:`10.1103/PhysRev.130.2193` (1963).
174. Jinnouchi, R. *et al.* Phase Transitions of Hybrid Perovskites Simulated by Machine-Learning Force Fields Trained on the Fly with Bayesian Inference. *Phys. Rev. Lett.* **122,** 225701. doi:`10.1103/PhysRevLett.122.225701` (2019).
175. Lahnsteiner, J. *et al.* Room-temperature dynamic correlation between methylammonium molecules in lead-iodine based perovskites: An *ab initio* molecular dynamics perspective. *Phys. Rev. B* **94,** 214114. doi:`10.1103/PhysRevB.94.214114` (2016).
176. Møller, C. K. THE STRUCTURE OF PEROVSKITE-LIKE CÆSIUM PLUMBO TRIHALIDES. *Mat. Fys. Medd. Dan. Vid. Selsk.* **32,** 28 (1959).
177. Sakata, M. *et al.* A neutron diffraction study of anharmonic thermal vibrations in cubic $CsPbX_3$. *Acta Crystallogr. A* **36,** 7–15. doi:`10.1107/S0567739480000022` (1980).
178. Zhao, X.-G. *et al.* Polymorphous nature of cubic halide perovskites. *Phys. Rev. B* **101,** 155137. doi:`10.1103/PhysRevB.101.155137` (2020).
179. Wang, C. *et al.* Giant Phonon Tuning Effect via Pressure-Manipulated Polar Rotation in Perovskite $MAPbI_3$. *J. Phys. Chem. Lett.* **9,** 3029–3034. doi:`10.1021/acs.jpclett.8b01101` (2018).

180. Henry, A. S. & Chen, G. Spectral Phonon Transport Properties of Silicon Based on Molecular Dynamics Simulations and Lattice Dynamics. *J. Comput. Theor. Nanosci.* **5,** 141–152. doi:`10.1166/jctn.2008.2454` (2008).

181. Weber, D. $CH_3NH_3PbX_3$, ein Pb(II)-System mit kubischer Perowskitstruktur / $CH_3NH_3PbX_3$, a Pb(II)-System with Cubic Perovskite Structure. *Z. NATURFORSCH B* **33,** 1443–1445. doi:`10.1515/znb-1978-1214` (1978).

182. Lee, S. *et al.* Resonant bonding leads to low lattice thermal conductivity. *Nat. Commun.* **5,** 3525. doi:`10.1038/ncomms4525` (2014).

183. Yue, S.-Y., Xu, T. & Liao, B. Ultralow thermal conductivity in a two-dimensional material due to surface-enhanced resonant bonding. *Mater. Today Phys.* **7,** 89–95. doi:`10.1016/j.mtphys.2018.11.005` (2018).

184. Chang, C. & Zhao, L.-D. Anharmoncity and low thermal conductivity in thermoelectrics. *Mater. Today Phys.* **4,** 50–57. doi:`10.1016/j.mtphys.2018.02.005` (2018).

185. Pankove, J. I. *Optical Processes in Semiconductors* (Dover Publications, Inc., New York, 1975).

186. Yu, P. Y. & Cardona, M. *Fundamentals of Semiconductors* 4th ed. (Springer, 2010).

187. Sadigh, B. *et al.* First-Principles Calculations of the Urbach Tail in the Optical Absorption Spectra of Silica Glass. *Phys. Rev. Lett.* **106,** 027401. doi:`10.1103/PhysRevLett.106.027401` (2011).

188. Yin, W. J., Shi, T. & Yan, Y. Unique properties of halide perovskites as possible origins of the superior solar cell performance. *Adv. Mater.* **26,** 4653–4658. doi:`10.1002/adma.201306281` (2014).

189. Davies, C. L. *et al.* Bimolecular recombination in methylammonium lead triiodide perovskite is an inverse absorption process. *Nat. Commun.* **9,** 1–9. doi:`10.1038/s41467-017-02670-2` (2018).

190. Wuttig, M. *et al.* Halide Perovskites: Advanced Photovoltaic Materials Empowered by a Unique Bonding Mechanism. *Adv. Funct. Mater.* doi:`10.1002/adfm.202110166` (2021).

191. Smith, E. H., Benedek, N. A. & Fennie, C. J. Interplay of Octahedral Rotations and Lone Pair Ferroelectricity in $CsPbF_3$. *Inorg. Chem.* **54,** 8536–8543. doi:`10.1021/acs.inorgchem.5b01213` (2015).

192. Young, J. & Rondinelli, J. M. Octahedral Rotation Preferences in Perovskite Iodides and Bromides. *J. Phys. Chem. Lett.* **7,** 918–922. doi:`10.1021/acs.jpclett.6b00094` (2016).

193. Ghosh, D. *et al.* Good Vibrations: Locking of Octahedral Tilting in Mixed-Cation Iodide Perovskites for Solar Cells. *ACS Energy Lett.* **2,** 2424–2429. doi:`10.1021/acsenergylett.7b00729` (2017).

194. Klarbring, J. Low-energy paths for octahedral tilting in inorganic halide perovskites. *Phys. Rev. B* **99,** 104105. doi:`10.1103/PhysRevB.99.104105` (2019).

195. Kim, J. *et al.* Importance of Orbital Interactions in Determining Electronic Band Structures of Organo-Lead Iodide. *J. Phys. Chem. C* **119,** 4627–4634. doi:`10.1021/jp5126365` (2015).

196. Goesten, M. G. & Hoffmann, R. Mirrors of Bonding in Metal Halide Perovskites. *J. Am. Chem. Soc.* **140,** 12996–13010. doi:`10.1021/jacs.8b08038` (2018).

197. Brod, M. K., Toriyama, M. Y. & Snyder, G. J. Orbital chemistry that leads to high valley degeneracy in PbTe. *Chem. Mater.* **32,** 9771–9779. doi:`10.1021/acs.chemmater.0c03740` (2020).

198. Pei, Y., Wang, H. & Snyder, G. J. Band Engineering of Thermoelectric Materials. *Adv. Mater.* **24,** 6125–6135. doi:`10.1002/adma.201202919` (2012).

199. Sootsman, J. R., Chung, D. Y. & Kanatzidis, M. G. New and Old Concepts in Thermoelectric Materials. *Angew. Chem. Int. Ed.* **48,** 8616–8639. doi:`10.1002/anie.200900598` (2009).

200. Chen, G. *et al.* Recent developments in thermoelectric materials. *Inter. Mater. Rev.* **48,** 45–66. doi:`10.1179/095066003225010182` (2003).

201. Biswas, K. *et al.* High-performance bulk thermoelectrics with all-scale hierarchical architectures. *Nature* **489,** 414–418. doi:`10.1038/nature11439` (2012).

202. Heremans, J. P. *et al.* Enhancement of Thermoelectric Efficiency in PbTe by Distortion of the Electronic Density of States. *Science* **321,** 554–557. doi:`10.1126/science.1159725` (2008).

203. Guo, P. *et al.* Polar Fluctuations in Metal Halide Perovskites Uncovered by Acoustic Phonon Anomalies. *ACS Energy Lett.* **2,** 2463–2469. doi:`10.1021/acsenergylett.7b00790` (2017).

204. An, J., Subedi, A. & Singh, D. Ab initio phonon dispersions for PbTe. *Solid State Commun.* **148,** 417–419. doi:`10.1016/j.ssc.2008.09.027` (2008).

205. Sangiorgio, B. *et al.* Correlated local dipoles in PbTe. *Phys. Rev. Mater.* **2.** doi:`10.1103/PhysRevMaterials.2.085402` (2018).

206. Ribeiro, G. A. S. *et al.* Strong anharmonicity in the phonon spectra of PbTe and SnTe from first principles. *Phys. Rev. B* **97.** doi:`10.1103/PhysRevB.97.014306` (2018).

207. Delaire, O. *et al.* Giant anharmonic phonon scattering in PbTe. *Nat. Mater.* **10,** 614–619. doi:`10.1038/nmat3035` (2011).

208. Romero, A. H. *et al.* Thermal conductivity in PbTe from first principles. *Phys. Rev. B* **91,** 214310. doi:`10.1103/PhysRevB.91.214310` (2015).

209. Klarbring, J. *et al.* Anharmonicity and Ultralow Thermal Conductivity in Lead-Free Halide Double Perovskites. *Phys. Rev. Lett.* **125,** 45701. doi:`10.1103/PhysRevLett.125.045701` (2020).

210. Goesten, M. G. & Hoffmann, R. Mirrors of Bonding in Metal Halide Perovskites. *J. Am. Chem. Soc.* **140,** 12996–13010. doi:`10.1021/jacs.8b08038` (2018).

211. Waghmare, U. V. *et al.* First-principles indicators of metallicity and cation off-centricity in the IV-VI rocksalt chalcogenides of divalent Ge, Sn, and Pb. *Phys. Rev. B* **67,** 10. doi:`10.1103/PhysRevB.67.125111` (2003).

212. Wei, S. H. & Zunger, A. Electronic and structural anomalies in lead chalcogenides. *Phys. Rev. B* **55,** 13605–13610. doi:`10.1103/PhysRevB.55.13605` (1997).

213. Fabini, D. H., Seshadri, R. & Kanatzidis, M. G. The underappreciated lone pair in halide perovskites underpins their unusual properties. *MRS Bull.* **45,** 467–477. doi:`10.1557/mrs.2020.142` (2020).

214. Gao, L. *et al.* Metal cation s lone-pairs increase octahedral tilting instabilities in halide perovskites. *Mater. Adv.* doi:`10.1039/d1ma00288k` (2021).

215. Kokalj, A. XCrySDen—a new program for displaying crystalline structures and electron densities. *J. Mol. Graph. Model.* **17,** 176–179. doi:`https://doi.org/10.1016/S1093-3263(99)00028-5` (1999).

216. Lu, Y., Sun, T. & Zhang, D.-B. Lattice anharmonicity, phonon dispersion, and thermal conductivity of PbTe studied by the phonon quasiparticle approach. *Phys. Rev. B* **97,** 174304. doi:`10.1103/PhysRevB.97.174304` (2018).

217. Scanlon, W. W. Recent advances in the optical and electronic properties of PbS, PbSe, PbTe and their alloys. *J. Phys. Chem. Solids* **8,** 423–428. doi:`10.1016/0022-3697(59)90379-8` (1959).

218. Gelmont, B., Globus, T. & Matveenko, A. Optical absorption and band structure of PbTe. *Solid State Commun.* **38,** 931–934. doi:`10.1016/0038-1098(81)90779-1` (1981).

219. Dalven, R. A review of the semiconductor properties of PbTe, PbSe, PbS and PbO. *Infrared Physics* **9,** 141–184. doi:`10.1016/0020-0891(69)90022-0` (1969).

220. Wang, J. *et al.* Structural, electrical, and optical properties of thermally evaporated nanocrystalline PbTe films. *J. Appl. Phys.* **104,** 053707. doi:`10.1063/1.2970163` (2008).

221. Lang, L. *et al.* Three-step approach for computing band offsets and its application to inorganic ABX_3 halide perovskites. *Phys. Rev. B* **92,** 075102. doi:`10.1103/PhysRevB.92.075102` (2015).

222. Kulbak, M., Cahen, D. & Hodes, G. How Important Is the Organic Part of Lead Halide Perovskite Photovoltaic Cells? Efficient $CsPbBr_3$ Cells. *J. Phys. Chem. Lett.* **6,** 2452–2456. doi:`10.1021/acs.jpclett.5b00968` (2015).

223. Lei, J. *et al.* Efficient planar $CsPbBr_3$ perovskite solar cells by dual-source vacuum evaporation. *Sol. Energy Mater. Sol. Cells* **187,** 1–8. doi:`10.1016/j.solmat.2018.07.009` (2018).

224. Mannino, G. *et al.* Temperature-Dependent Optical Band Gap in $CsPbBr_3$, $MAPbBr_3$, and $FAPbBr_3$ Single Crystals. *J. Phys. Chem. Lett.* **11,** 2490–2496. doi:`10.1021/acs.jpclett.0c00295` (2020).

225. Rakita, Y. *et al.* Low-Temperature Solution-Grown $CsPbBr_3$ Single Crystals and Their Characterization. *Cryst. Growth Des.* **16,** 5717–5725. doi:`10.1021/acs.cgd.6b00764` (2016).

226. Manthiram, A., Yu, X. & Wang, S. Lithium battery chemistries enabled by solid-state electrolytes. *Nat. Rev. Mater.* **2,** 16103. doi:`10.1038/natrevmats.2016.103` (2017).

227. Lin, Y.-Y. *et al.* Toward design of cation transport in solid-state battery electrolytes: Structure-dynamics relationships. *Curr. Opin. Solid State Mater. Sci.* **24,** 100875. doi:`10.1016/j.cossms.2020.100875` (2020).

228. Li, J. *et al.* Solid Electrolyte: the Key for High-Voltage Lithium Batteries. *Adv. Energy Mater.* **5,** 1401408. doi:`https://doi.org/10.1002/aenm.201401408` (2015).

229. Funke, K. Solid State Ionics: from Michael Faraday to green energy—the European dimension. *Sci. Technol. Adv. Mater.,* 51 (2013).

230. Jacobson, A. J. Materials for Solid Oxide Fuel Cells. *Chem. Mater.* **22,** 660–674. doi:`10.1021/cm902640j` (2010).

231. Moseley, P. T. Solid state gas sensors. *Meas. Sci. Technol.* **8,** 223–237. doi:`10.1088/0957-0233/8/3/003` (1997).

232. Gouaux, E. & MacKinnon, R. Principles of Selective Ion Transport in Channels and Pumps. *Science* **310,** 1461–1465. doi:`10.1126/science.1113666` (2005).

233. Gordiz, K. *et al.* Enhancement of ion diffusion by targeted phonon excitation. *Cell Reports Physical Science* **2,** 100431. doi:`10.1016/j.xcrp.2021.100431` (2021).

234. Schommers, W. Correlations in the Motion of Particles in α -AgI: A Molecular-Dynamics Study. *Phys. Rev. Lett.* **38,** 1536–1539. doi:`10.1103/PhysRevLett.38.1536` (1977).

235. Hokazono, M., Ueda, A. & Hiwatari, Y. Dynamical structure of superionic conductors. *Solid State Ion.* **13,** 151–155. doi:`10.1016/0167-2738(84)90050-X` (1984).

236. Yokoyama, Y. & Kobayashi, M. Nano-scaled dynamics of iodine-tetrahedron in α-AgI. *Solid State Ion.* **159,** 79–87. doi:`10.1016/S0167-2738(03)00033-X` (2003).

237. Wood, B. C. & Marzari, N. Dynamical Structure, Bonding, and Thermodynamics of the Superionic Sublattice in α-AgI. *Phys. Rev. Lett.* **97,** 166401. doi:`10.1103/PhysRevLett.97.166401` (2006).

238. Matsunaga, S. Structure and Atomic Dynamics of Silver Halide Mixtures. *Prog. Theor. Phys. Suppl.* **178,** 113–119. doi:`10.1143/PTPS.178.113` (2009).

239. Wakamura, K. Roles of phonon amplitude and low-energy optical phonons on superionic conduction. *Phys. Rev. B* **56,** 11593–11599. doi:`10.1103/PhysRevB.56.11593` (1997).

240. Bachman, J. C. *et al.* Inorganic Solid-State Electrolytes for Lithium Batteries: Mechanisms and Properties Governing Ion Conduction. *Chem. Rev.* **116,** 140–162. doi:`10.1021/acs.chemrev.5b00563` (2016).

241. Kraft, M. A. *et al.* Influence of Lattice Polarizability on the Ionic Conductivity in the Lithium Superionic Argyrodites Li_6PS_5X (X = Cl, Br, I). *J. Am. Chem. Soc.* **139,** 10909–10918. doi:`10.1021/jacs.7b06327` (2017).

242. Krauskopf, T. *et al.* Influence of Lattice Dynamics on Na^+ Transport in the Solid Electrolyte $Na_3PS_{4-x}Se_x$. *Chem. Mater.* **29,** 8859–8869. doi:`10.1021/acs.chemmater.7b03474` (2017).

243. Krauskopf, T. *et al.* Comparing the Descriptors for Investigating the Influence of Lattice Dynamics on Ionic Transport Using the Superionic Conductor $Na_3PS_{4-x}Se_x$. *J. Am. Chem. Soc.* **140,** 14464–14473. doi:`10.1021/jacs.8b09340` (2018).

244. Sagotra, A. K., Chu, D. & Cazorla, C. Influence of lattice dynamics on lithium-ion conductivity: A first-principles study. *Phys. Rev. Mater.* **3,** 035405. doi:`10.1103/PhysRevMaterials.3.035405` (2019).

245. Rice, S. A. Dynamical Theory of Diffusion in Crystals. *Phys. Rev.* **112,** 804–811. doi:`10.1103/PhysRev.112.804` (1958).

246. Vineyard, G. H. Frequency factors and isotope effects in solid state rate processes. *J. Phys. Chem. Solids* **3,** 121–127. doi:`10.1016/0022-3697(57)90059-8` (1957).

247. *Physics of Superionic Conductors* (ed Salamon, M.) (Springer-Verlag, 1979).

248. Maier, J. *Physical Chemistry of Ionic Materials: Ions and Electrons in Solids* (Wiley, 2004).

249. Almond, D. & West, A. The activation entropy for transport in ionic conductors. *Solid State Ion.* **23,** 27–35. doi:`10.1016/0167-2738(87)90078-6` (1987).

250. Hanson, R. C., Fjeldly, T. A. & Hochheimer, H. D. Raman Scattering from Five Phases of Silver Iodide. *phys. stat. sol. (b)* **70,** 567–576. doi:`10.1002/pssb.2220700216` (1975).

251. Dessens, J. *et al.* Hail prevention by ground-based silver iodide generators: Results of historical and modern field projects. *Atmos. Res.* **170,** 98–111. doi:`10.1016/j.atmosres.2015.11.008` (2016).

252. Kvist, A. & Tärneberg, R. Self-diffusion of Silver Ions in the Cubic High Temperature Modification of Silver Iodide. *Z. NATURFORSCH. A* **25,** 257–259. doi:`10.1515/zna-1970-0219` (1970).

253. Cava, R. J., Reidinger, F. & Wuensch, B. J. Single-crystal neutron-diffraction study of AgI between 23° and 300°C. *Solid State Commun.* **24,** 411–416. doi:`10.1016/0038-1098(77)91306-0` (1977).

254. Wright, A. F. & Fender, B. E. F. The structure of superionic compounds by powder neutron diffraction. I. Cation distribution in α-AgI. *J. Phys. C: Solid State Phys.* **10,** 2261–2267. doi:`10.1088/0022-3719/10/13/003` (1977).

255. Hoshino, S. Crystal Structure and Phase Transition of Some Metallic Halides IV On the Anomalous Structure of α-AgI. *J. Phys. Soc. Jpn.* **12,** 315–326. doi:`10.1143/JPSJ.12.315` (1957).

256. Hoshino, S., Sakuma, T. & Fujii, Y. DISTRIBUTION AND ANHARMONIC THERMAL VIBRATION OF CATIONS IN a-AgI. *Solid State Commun.* **22,** 763–765 (1977).

257. Boyce, J. B. *et al.* Position and Dynamics of Ag Ions in Superionic AgI Using Extended X-Ray Absorption Fine Structure. *Phys. Rev. Lett.* **38,** 1362–1365. doi:`10.1103/PhysRevLett.38.1362` (1977).

258. Cazzanelli, E. *et al.* Analysis of the Raman spectral shape in α-AgI. *Phys. Rev. B* **28,** 7269–7276. doi:`10.1103/PhysRevB.28.7269` (1983).

259. Nemanich, R., Martin, R. M. & Mikkelsen, J. in *Inelastic Light Scattering* 79–82 (Elsevier, 1980). doi:`10.1016/B978-0-08-025425-8.50022-2`.

260. Guo, Y. *et al.* Interplay between organic cations and inorganic framework and incommensurability in hybrid lead-halide perovskite $CH_3NH_3PbBr_3$. *Phys. Rev. Mater.* **1,** 042401. doi:`10.1103/PhysRevMaterials.1.042401` (2017).

261. Damle, V. H. *et al.* Structural Characterization and Room Temperature Low-Frequency Raman Scattering from $MAPbI_3$ Halide Perovskite Films Rigidized by Cesium Incorporation. *ACS Appl. Energy Mater.* **1,** 6707–6713. doi:`10.1021/acsaem.8b01539` (2018).

262. Quittet, A. M. *et al.* Anomalous scattering and asymmetrical line shapes in Raman spectra of orthorhombic $KNbO_3$. *Phys. Rev. B* **14,** 5068–5072. doi:`10.1103/PhysRevB.14.5068` (1976).

263. Kania, A. *et al.* Raman scattering, central peak and phase transitions in $AgNbO_3$. *J. Phys. C: Solid State Phys.* **19,** 9–20. doi:`10.1088/0022-3719/19/1/007` (1986).

264. Sokoloff, J. P., Chase, L. L. & Rytz, D. Direct observation of relaxation modes in $KNbO_3$ and $BaTiO_3$ using inelastic light scattering. *Phys. Rev. B* **38,** 597–605. doi:`10.1103/PhysRevB.38.597` (1988).

265. Sokoloff, J. P., Chase, L. L. & Boatner, L. A. Low-frequency relaxation modes and structural disorder in $KTa_{1-x}Nb_xO_3$. *Phys. Rev. B* **41,** 2398–2408. doi:`10.1103/PhysRevB.41.2398` (1990).

266. DiAntonio, P. *et al.* Polar fluctuations and first-order Raman scattering in highly polarizable $KTaO_3$ crystals with off-center Li and Nb ions. *Phys. Rev. B* **47,** 5629–5637. doi:`10.1103/PhysRevB.47.5629` (1993).

267. Ko, J.-H. *et al.* Elastic softening and central peaks in BaTiO3 single crystals above the cubic-tetragonal phase-transition temperature. *Appl. Phys. Lett.* **93,** 102905. doi:`10.1063/1.2980444` (2008).

268. Winterling, G. Very-low-frequency Raman scattering in vitreous silica. *Phys. Rev. B* **12,** 2432–2440. doi:`10.1103/PhysRevB.12.2432` (1975).

269. Siny, I. G. *et al.* Central peak in light scattering from the relaxor ferroelectric $PbMg_{1/3}Nb_{2/3}O_3$. *Phys. Rev. B* **56,** 7962–7966. doi:`10.1103/PhysRevB.56.7962` (1997).

270. Jiang, F. M., Ko, J.-H. & Kojima, S. Central peaks and Brillouin scattering in uniaxial relaxor single crystals of $Sr_{0.61}Ba_{0.39}Nb_2O_6$. *Phys. Rev. B* **66,** 184301. doi:`10.1103/PhysRevB.66.184301` (2002).

271. Shabbir, G. & Kojima, S. Central Peak in PLZT Relaxors Studied by Micro-Brillouin Scattering. *Ferroelectrics* **303,** 167–171. doi:`10.1080/00150190490453568` (2004).

272. Malinovsky, V. K., Pugachev, A. M. & Surovtsev, N. V. Study of the central peak in Raman spectra of SBN crystals. *Bull. Russ. Acad. Sci. Phys.* **74,** 1231–1234. doi:`10.3103/S1062873810090133` (2010).

273. Dieterich, W., Geisel, T. & Peschel, I. Scattering of light and neutrons in a model for superionic conductors. *Z. Physik B* **29,** 5–12 (1978).

274. Anderson, P. W. Absence of Diffusion in Certain Random Lattices. *Phys. Rev.* **109,** 1492–1505. doi:`10.1103/PhysRev.109.1492` (1958).

275. Allen, P. B. & Feldman, J. L. Thermal conductivity of disordered harmonic solids. *Phys. Rev. B* **48,** 12581–12588. doi:`10.1103/PhysRevB.48.12581` (1993).

276. Allen, P. B. *et al.* Diffusons, locons and propagons: Character of atomic vibrations in amorphous Si. *Philos. Mag. B* **79,** 1715–1731. doi:`10.1080/13642819908223054` (1999).

277. Troisi, A. & Orlandi, G. Charge-Transport Regime of Crystalline Organic Semiconductors: Diffusion Limited by Thermal Off-Diagonal Electronic Disorder. *Phys. Rev. Lett.* **96,** 086601. doi:`10.1103/PhysRevLett.96.086601` (2006).

278. Eggeman, A. S. *et al.* Measurement of molecular motion in organic semiconductors by thermal diffuse electron scattering. *Nat. Mater.* **12,** 1045–1049. doi:`10.1038/nmat3710` (2013).

279. Fratini, S., Mayou, D. & Ciuchi, S. The Transient Localization Scenario for Charge Transport in Crystalline Organic Materials. *Adv. Funct. Mater.* **26,** 2292–2315. doi:`10.1002/adfm.201502386` (2016).

280. Fratini, S. *et al.* A map of high-mobility molecular semiconductors. *Nat. Mater.* **16,** 998–1002. doi:`10.1038/nmat4970` (2017).

281. Fratini, S. *et al.* Charge transport in high-mobility conjugated polymers and molecular semiconductors. *Nat. Mater.* **19,** 491–502. doi:`10.1038/s41563-020-0647-2` (2020).

282. Bokdam, M., Lahnsteiner, J. & Sarma, D. D. Exploring librational pathways with on-the-fly machine-learning force fields: Methylammonium molecules in $MAPbX_3$ (X=I, Br, Cl) perovskites. *J. Phys. Chem. C* **125,** 21077–21086. doi:`10.1021/acs.jpcc.1c06835` (2021).

283. Gupta, M. K. *et al.* Fast Na diffusion and anharmonic phonon dynamics in superionic Na_3PS_4. *Energy Environ. Sci.* **14,** 6554–6563. doi:`10.1039/D1EE01509E` (2021).

284. Lacroix, A. *et al.* Modeling of Electronic Mobilities in Halide Perovskites: Adiabatic Quantum Localization Scenario. *Phys. Rev. Lett.* **124,** 196601. doi:`10.1103/PhysRevLett.124.196601` (2020).

285. Mizoguchi, K. & Nakashima, S.-i. Determination of crystallographic orientations in silicon films by Raman-microprobe polarization measurements. *J. Appl. Phys.* **65,** 2583–2590. doi:`10.1063/1.342787` (1989).

Appendix A. Supplemental figures

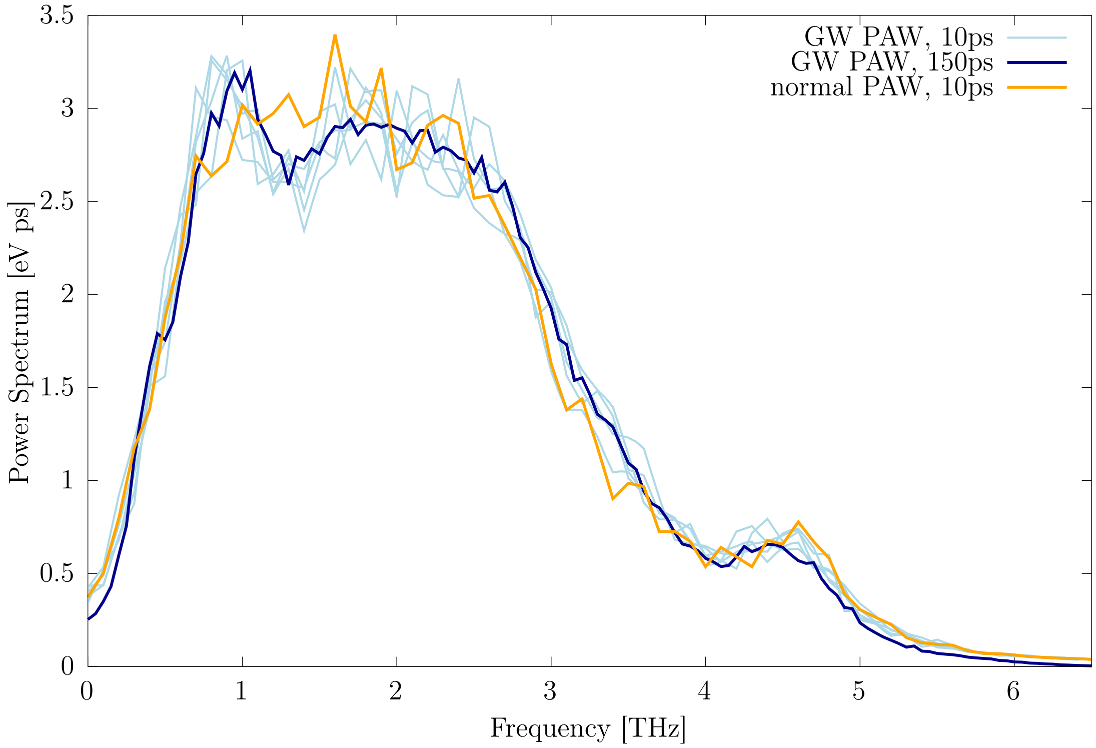

Figure A1.: Power spectrum of the VACF obtained from MD simulations at T=425 K obtained with the “GW” PAW pseudo-potentials (blue) compared with “normal” PAW pseudo-potentials (orange).

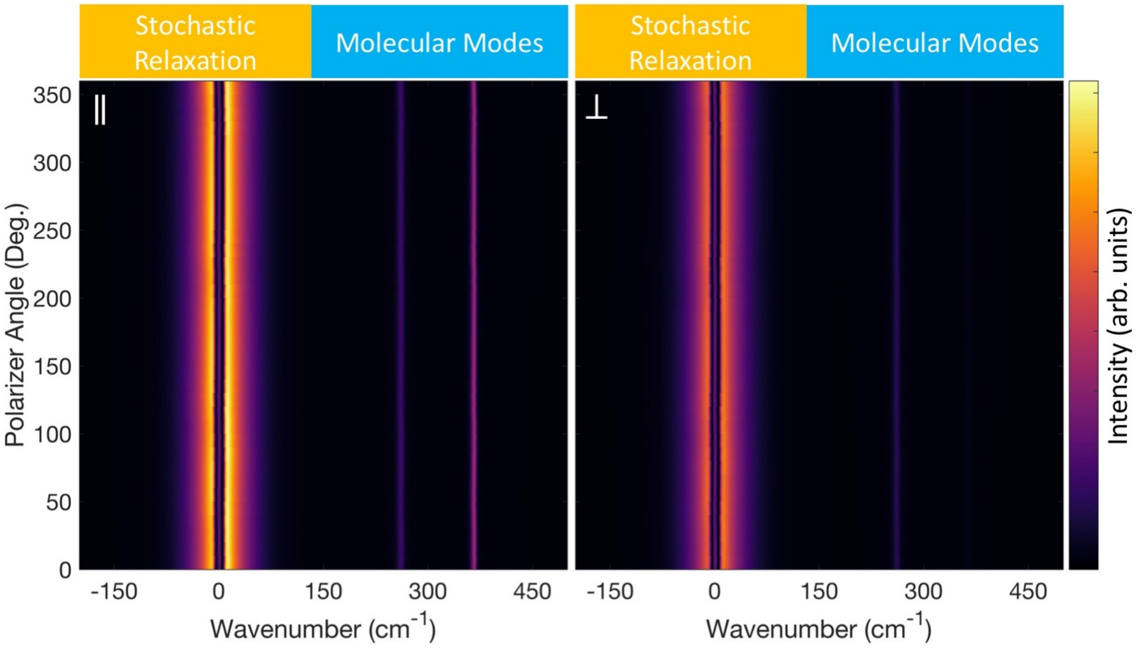

Figure A2.: PO Raman spectrum of liquid chloroform ($CHCl_3$) at room temperature. An orientation-independent central peak can be observed, indicating stochastic relaxation processes . Although there are differences between parallel and perpendicular measurements, no angular dependence can be found. *Reprinted with permission from [3]. Copyright (2020) by the American Physical Society.*

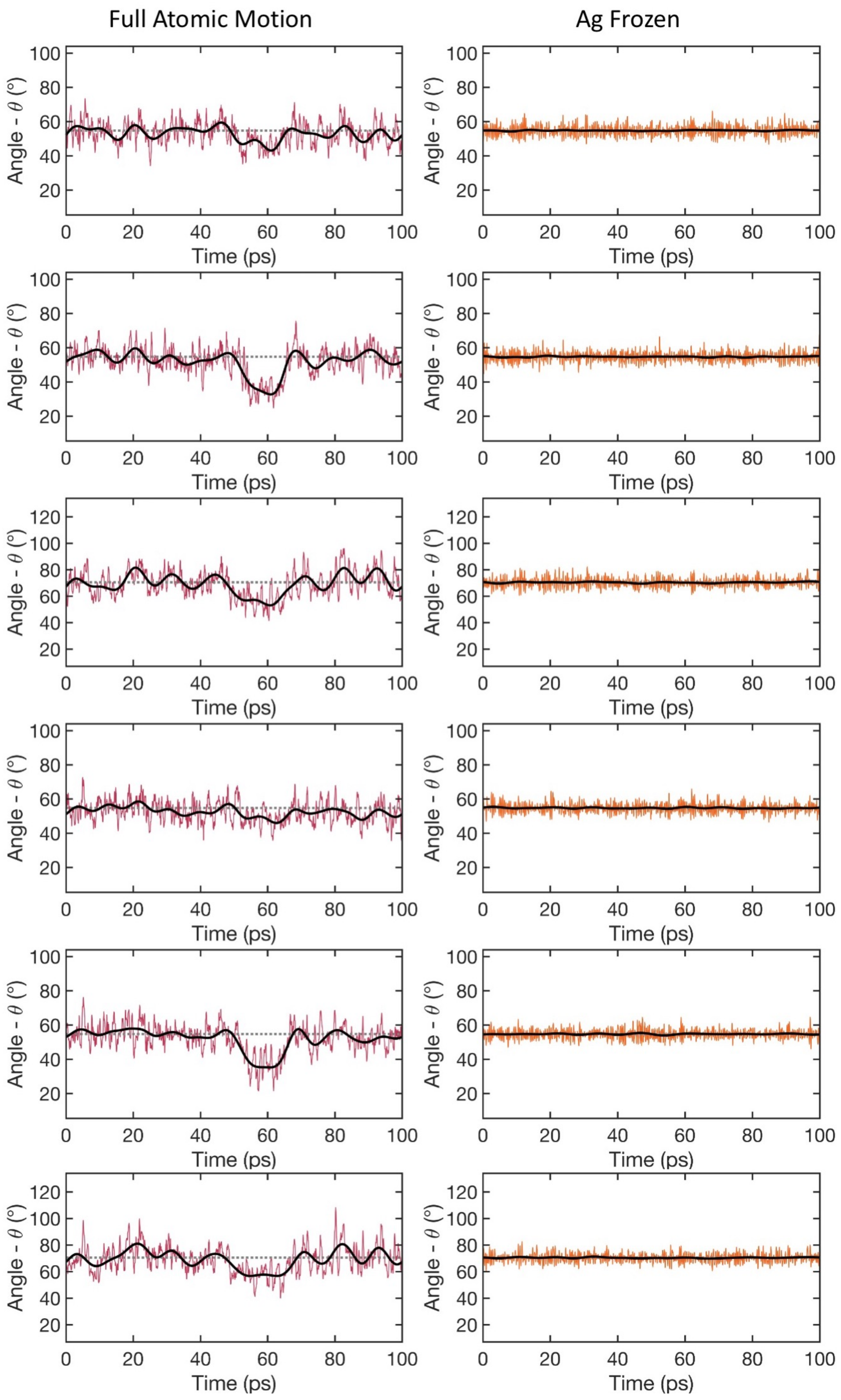

Figure A3.: Trajectories of all 12 I-I-I bond angles θ (continued in fig. A4) as obtained from MD simulations at 500 K. The unfiltered trajectories are shown in red (full MD) and orange (Ag frozen), the black lines show the trajectories filtered with a Fourier filter. The expectation values are indicated by the gray horizontal lines. *Reprinted with permission from [3]. Copyright (2020) by the American Physical Society.*

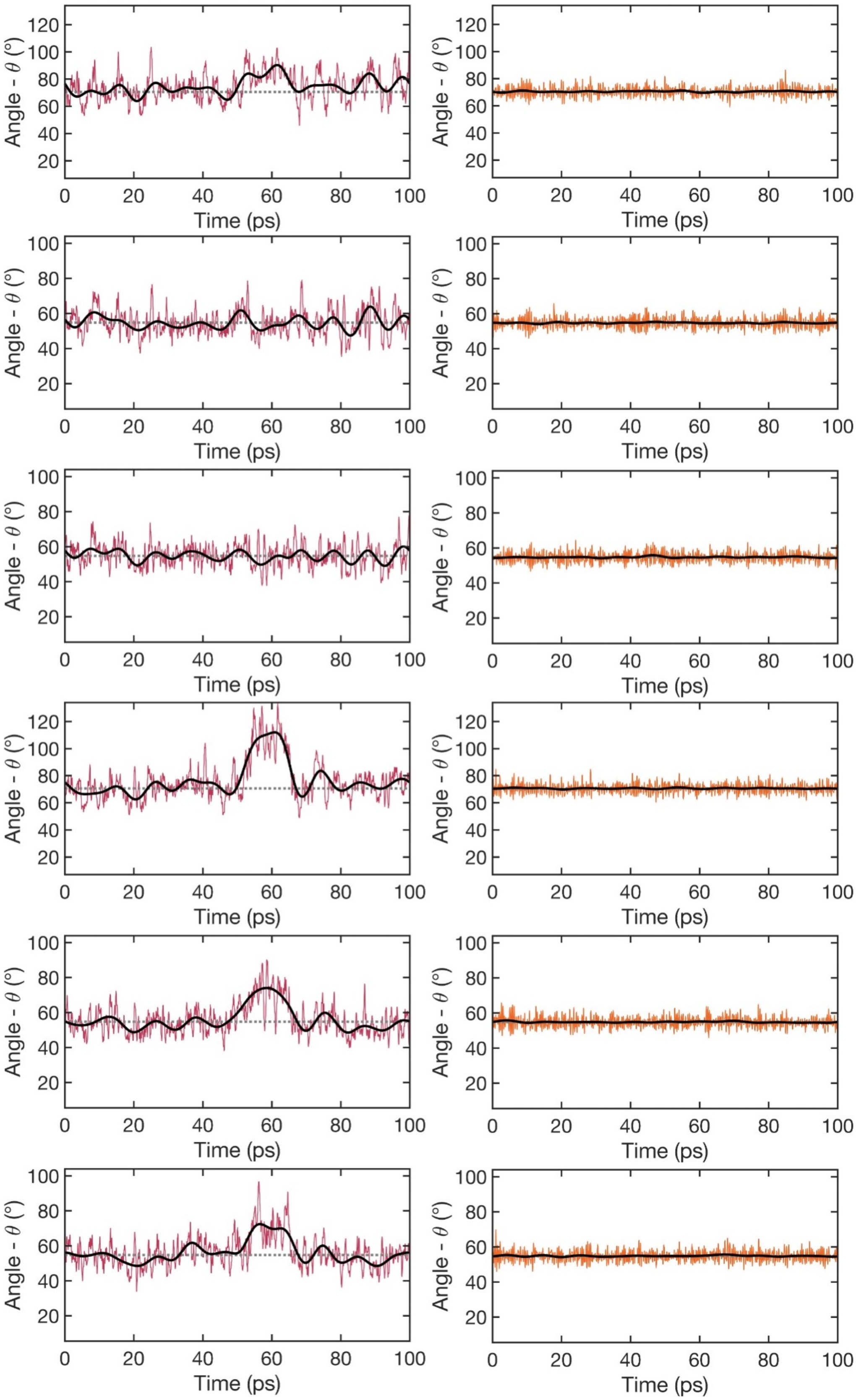

Figure A4.: Trajectories of all 12 I-I-I bond angles θ (continued from fig. A3) as obtained from MD simulations at 500 K. The unfiltered trajectories are shown in red (full MD) and orange (Ag frozen), the black lines show the trajectories filtered with a Fourier filter. The expectation values are indicated by the gray horizontal lines. *Reprinted with permission from [3]. Copyright (2020) by the American Physical Society.*

Appendix B.

Simplistic model to explain oscillatory decaying autocorrelation functions

In this appendix, following reference [5], a simplistic model for the correlations in a one dimensional periodic function, resembling the potential in a crystal, is presented. A "disorder potential" of amplitude A_i preserving the translational invariance of a crystalline material, with spatial periodicity ω_i, might be written as

$$\Delta V_i(y) = A_i \sin(\omega_i \, y) \ . \tag{B1}$$

For this case, normalized autocorrelation function

$$C_i(\Delta y) = \frac{\langle \Delta V_i(y + \Delta y) \cdot \Delta V_i(y) \rangle}{\langle \Delta V_i(y) \cdot \Delta V_i(y) \rangle} \ , \tag{B2}$$

is periodic too (see fig. B1a and fig. B1b for the potential and autocorrelation, respectively). However, for a crystalline material at finite temperature, the periodicity is expected to be disturbed due to nuclear motion. This has been mimicked in fig. B1c by using randomized A_i and ω_i. The correlation of each randomized function, shown as light red lines in fig. B1d, still is periodic and non-decaying, as each function still only has one (random) frequency. But a combination of several randomized functions culminates in a autocorrelation function which is both oscillatory and decaying. This on one hand resembles a periodic potential which is modulated by thermal noise due to nuclear displacements and on the other hand the autocorrelation function resembles the one found in section 3.8, fig. 3.35.

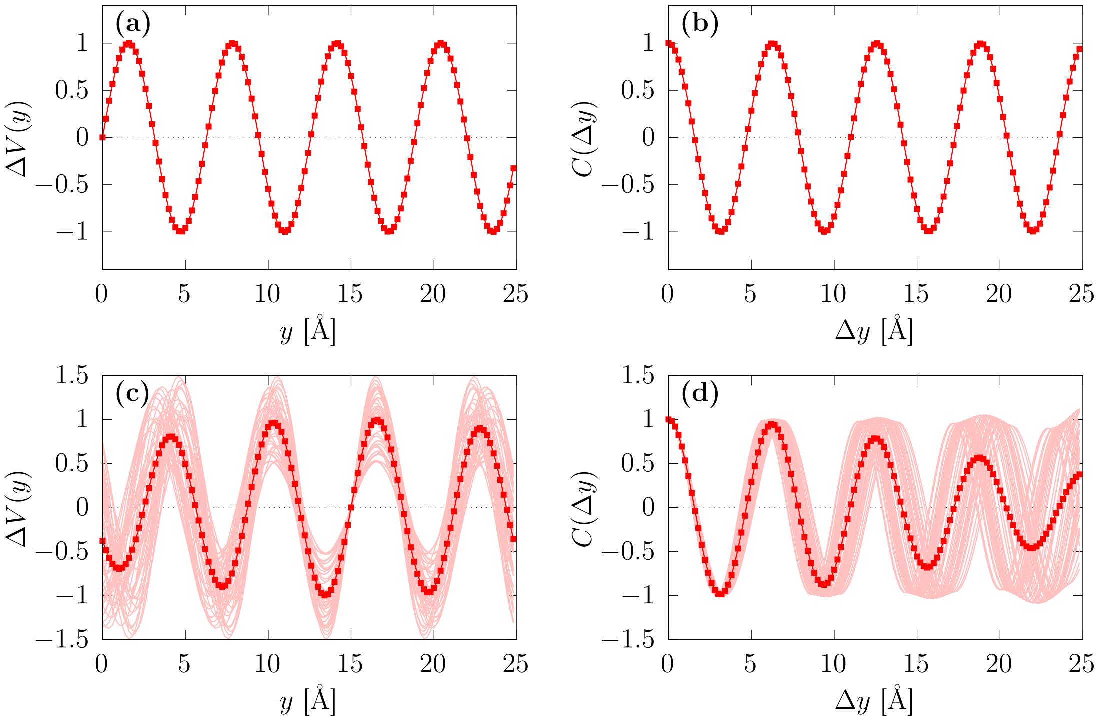

Figure B1.: Toy model to explain oscillatory and decaying autocorrelation functions. **(a)** shows the function of eq. (B1) for $A = 1$ and $\omega = 1$. **(b)** shows the autocorrelation function (eq. (B2)) for the periodic function shown in panel a. **(c)** $N = 50$ randomized functions with $0.5 \leq A_i \leq 1.5$ and $0.9 \leq \omega \leq 1.1$ chosen randomly (light red), the dark red curve shows their average. **(d)** shows autocorrelation functions for the 50 randomized functions of panel c (light red), and the average $\overline{C}(\Delta y) = N^{-1} \sum_{i=1}^{N} C_i(\Delta y)$ (dark red). *Reprinted with permission from [5], published under a CC BY 4.0 license.*

Appendix C. Polarization-orientation Raman spectroscopy

In this appendix, we will further discuss some aspects of PO Raman spectroscopy, following reference [285], as this will help in understanding the experimental results in section 4.3 and the model depicted from this. Since the Raman intensity is connected to the change of the polarizability $\hat{\alpha}$, which is a tensor, also a Raman tensor

$$\hat{\mathsf{R}}_\nu \propto \frac{\partial \hat{\alpha}_\nu}{\partial \mathbf{Q}_\nu} \ , \tag{C1}$$

can be defined. As with the polarizability, the elements of the Raman tensor are determined by the symmetry of the specific Raman active phonon mode. The Raman intensity is then given by

$$I_\nu \propto \left| \mathbf{e}_i \hat{\mathsf{R}}_\nu \mathbf{e}_s \right|^2 \ , \tag{C2}$$

with $\mathbf{e}_{i/s}$ the polarization vectors of the incident and scattered light, respectively. Equation (C2) provides that the intensity of a Raman active mode ν depends on the polarization of the incident and scattered light. Or, *vice versa*, the components of the Raman tensor can be obtained from measurements using incident light with a specific orientation of the polarized light. Such an experimental measurement is called PO Raman spectroscopy and sketched in fig. C1. As visualized in fig. C1, the incident light is polarized, using a polarizer, with a specific angle θ with respect to the predefined x-axis

$$\mathbf{e}_i = (\cos\,\theta, \sin\,\theta, 0)^T \ . \tag{C3}$$

During the experiment, θ is varied from 0 to 2π and the Raman intensity is measured for scattered light with an orientation parallel and perpendicular to the incident polarization, i.e.,

$$\mathbf{e}_{s,\parallel}(\theta) = \mathbf{e}_i(\theta) \quad \text{and} \quad \mathbf{e}_{s,\perp}(\theta) = (-\sin\,\theta, \cos\,\theta, 0)^T \ . \tag{C4}$$

As a consequence, the symmetry of a Raman mode can be determined from the periodicity of

$$I_{\nu,\parallel}(\theta) \propto \left| \mathbf{e}_i(\theta) \hat{\mathsf{R}}_\nu \mathbf{e}_{s,\parallel}(\theta) \right|^2 \tag{C5}$$

$$\text{and} \quad I_{\nu,\perp}(\theta) \propto \left| \mathbf{e}_i(\theta) \hat{\mathsf{R}}_\nu \mathbf{e}_{s,\perp}(\theta) \right|^2 \ . \tag{C6}$$

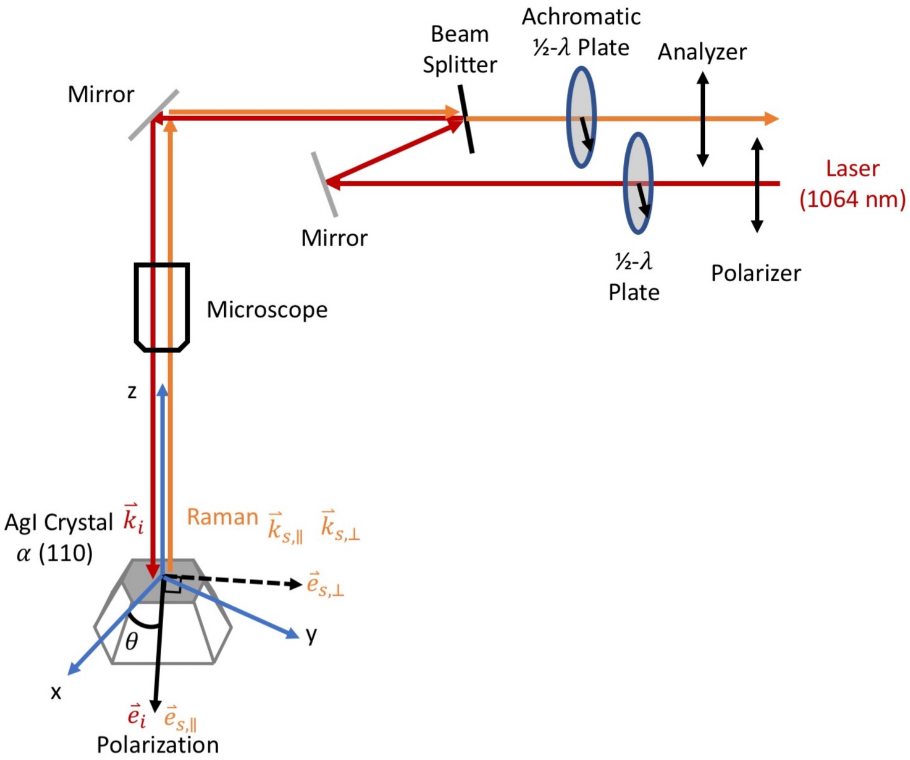

Figure C1.: Sketch of an experimental setup to measure the polarization-orientation (PO) Raman spectrum of a sample, in this example α-AgI. *Reprinted with permission from [3]. Copyright (2020) by the American Physical Society.*

This allows to match the measured frequencies to specific phonon modes, if their irreducible representation is known, and in the case of the SSIC α-AgI this method particularly allows to distinguish disorder induced, e.g., liquid-like Raman response, exhibiting no periodicity, from vibrational features showing specific symmetries.